

University of Warwick institutional repository: <http://go.warwick.ac.uk/wrap>

A Thesis Submitted for the Degree of PhD at the University of Warwick

<http://go.warwick.ac.uk/wrap/56778>

This thesis is made available online and is protected by original copyright.

Please scroll down to view the document itself.

Please refer to the repository record for this item for information to help you to cite it. Our policy information is available from the repository home page.

Library Declaration and Deposit Agreement

1. STUDENT DETAILS

Please complete the following:

Full name:

University ID number:

2. THESIS DEPOSIT

2.1 I understand that under my registration at the University, I am required to deposit my thesis with the University in BOTH hard copy and in digital format. The digital version should normally be saved as a single pdf file.

2.2 The hard copy will be housed in the University Library. The digital version will be deposited in the University's Institutional Repository (WRAP). Unless otherwise indicated (see 2.3 below) this will be made openly accessible on the Internet and will be supplied to the British Library to be made available online via its Electronic Theses Online Service (EThOS) service.

[At present, theses submitted for a Master's degree by Research (MA, MSc, LLM, MS or MMedSci) are not being deposited in WRAP and not being made available via EThOS. This may change in future.]

2.3 In exceptional circumstances, the Chair of the Board of Graduate Studies may grant permission for an embargo to be placed on public access to the hard copy thesis for a limited period. It is also possible to apply separately for an embargo on the digital version. (Further information is available in the *Guide to Examinations for Higher Degrees by Research*.)

2.4 *If you are depositing a thesis for a Master's degree by Research, please complete section (a) below. For all other research degrees, please complete both sections (a) and (b) below:*

(a) Hard Copy

I hereby deposit a hard copy of my thesis in the University Library to be made publicly available to readers (please delete as appropriate) EITHER immediately OR after an embargo period of months/years as agreed by the Chair of the Board of Graduate Studies.

I agree that my thesis may be photocopied.

YES / NO (Please delete as appropriate)

(b) Digital Copy

I hereby deposit a digital copy of my thesis to be held in WRAP and made available via EThOS.

Please choose one of the following options:

EITHER My thesis can be made publicly available online. YES / NO (Please delete as appropriate)

OR My thesis can be made publicly available only after.....[date] (Please give date)

YES / NO (Please delete as appropriate)

OR My full thesis cannot be made publicly available online but I am submitting a separately identified additional, abridged version that can be made available online.

YES / NO (Please delete as appropriate)

OR My thesis cannot be made publicly available online.

YES / NO (Please delete as appropriate)

3. GRANTING OF NON-EXCLUSIVE RIGHTS

Whether I deposit my Work personally or through an assistant or other agent, I agree to the following:

Rights granted to the University of Warwick and the British Library and the user of the thesis through this agreement are non-exclusive. I retain all rights in the thesis in its present version or future versions. I agree that the institutional repository administrators and the British Library or their agents may, without changing content, digitise and migrate the thesis to any medium or format for the purpose of future preservation and accessibility.

4. DECLARATIONS

(a) I DECLARE THAT:

- I am the author and owner of the copyright in the thesis and/or I have the authority of the authors and owners of the copyright in the thesis to make this agreement. Reproduction of any part of this thesis for teaching or in academic or other forms of publication is subject to the normal limitations on the use of copyrighted materials and to the proper and full acknowledgement of its source.
- The digital version of the thesis I am supplying is the same version as the final, hard-bound copy submitted in completion of my degree, once any minor corrections have been completed.
- I have exercised reasonable care to ensure that the thesis is original, and does not to the best of my knowledge break any UK law or other Intellectual Property Right, or contain any confidential material.
- I understand that, through the medium of the Internet, files will be available to automated agents, and may be searched and copied by, for example, text mining and plagiarism detection software.

(b) IF I HAVE AGREED (in Section 2 above) TO MAKE MY THESIS PUBLICLY AVAILABLE DIGITALLY, I ALSO DECLARE THAT:

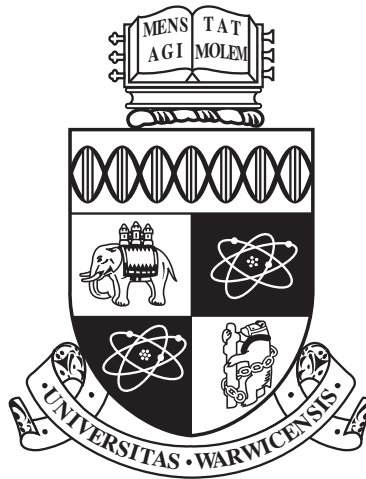
- I grant the University of Warwick and the British Library a licence to make available on the Internet the thesis in digitised format through the Institutional Repository and through the British Library via the EThOS service.
- If my thesis does include any substantial subsidiary material owned by third-party copyright holders, I have sought and obtained permission to include it in any version of my thesis available in digital format and that this permission encompasses the rights that I have granted to the University of Warwick and to the British Library.

5. LEGAL INFRINGEMENTS

I understand that neither the University of Warwick nor the British Library have any obligation to take legal action on behalf of myself, or other rights holders, in the event of infringement of intellectual property rights, breach of contract or of any other right, in the thesis.

Please sign this agreement and return it to the Graduate School Office when you submit your thesis.

Student's signature: Date:



**The effect of toroidal flows on the stability of ITGs
in MAST**

by

Peter A. Hill

Thesis

Submitted to the University of Warwick

for the degree of

Doctor of Philosophy

Physics

.... ..

THE UNIVERSITY OF
WARWICK

Contents

Acknowledgments	iv
Declarations	vi
Abstract	vii
Chapter 1 Introduction	1
1.1 Motivation	1
1.1.1 What is fusion	2
1.2 Magnetic confinement	4
1.2.1 Single particle motion	5
1.2.2 Tokamak equilibria	7
1.2.3 Magnetic mirroring and trapped particles	9
1.3 Transport in tokamaks	10
1.3.1 Classical and neoclassical theory	11
1.3.2 Anomalous transport and turbulence	13
1.4 The MAST device	14
1.4.1 Spherical tokamaks	14
1.4.2 Local vs. global analysis	14
1.5 Outline	16
Chapter 2 Gyrokinetics	18
2.1 Introduction	18
2.2 Gyrokinetic ordering	19
2.3 Lie formalism	21
2.3.1 Lagrangian in particle space	22
2.3.2 Guiding centre transformation	24
2.3.3 Gyro-centre transformation	25
2.3.4 The gyrokinetic equations of motion	28

2.4	Vlasov equation and the δf formulation	28
2.5	Poisson's equation and quasi-neutrality	30
2.6	Summary	32
Chapter 3	Microinstabilities	33
3.1	"Universal drive"	34
3.2	Toroidal ITG mode	35
3.3	Trapped particle effects	38
3.4	Turbulence	38
3.4.1	Zonal Flows	40
3.4.2	Turbulence diagnostics	41
3.5	Sheared flow stabilisation	41
3.6	Summary	44
Chapter 4	The global gyrokinetic PIC code NEMORB	45
4.1	Particle-in-cell method	45
4.2	Straight-field line coordinates	46
4.3	Parallelisation scheme	48
4.4	Numerical discretisation of equations	48
4.4.1	Equilibrium	48
4.4.2	Equations of motion in straight field line coordinates	49
4.4.3	Vlasov equation	50
4.4.4	Poisson equation	52
4.4.5	Diagnostics	54
4.4.6	Conservation properties	55
4.4.7	Noise control	56
4.5	Benchmarking	57
Chapter 5	Linear stability of global ITG modes in $E \times B$ flows	59
5.1	Introduction	59
5.2	Gyrokinetic Model	60
5.3	The CYCLONE base case	63
5.4	Small-aspect ratio, MAST-like equilibrium with analytic rotation profile	67
5.5	Small-aspect ratio, MAST-like equilibrium with experimental rota- tion profile and adiabatic electrons	72
5.6	MAST-like equilibrium with experimental rotation profile and kinetic trapped electrons	74
5.7	Conclusion	76

Chapter 6	Nonlinear simulations of ITG/TEM turbulence and comparison with MAST experiments	77
6.1	Introduction	77
6.2	Tuning parameters	79
6.2.1	Noise	80
6.2.2	Shielding	82
6.2.3	Heating	83
6.2.4	Markers	84
6.3	Transport	84
6.4	Comparison with linear studies	89
6.4.1	Counter-rotation	94
6.5	Comparison with experiment	98
6.5.1	BES system	99
6.5.2	Results	102
6.6	Conclusions	105
Chapter 7	The role of collisions on ITG/TEMs in MAST	106
7.1	Implementation	106
7.2	Linear studies	108
7.3	Nonlinear studies	109
7.3.1	Coarse-graining	110
7.3.2	Number of markers	110
7.4	Results	112
7.4.1	Comparison to experiment	113
7.5	Conclusion	114
Chapter 8	Conclusion	117
8.1	Summary of key results	117
8.2	Future work	119
Appendix A	Notation	121

Acknowledgments

I owe a great deal of thanks to a great many people. First and foremost, I am grateful to Dr. Erwin Verwichte, my supervisor at University at Warwick, and to Dr. Samuli Saarelma, my supervisor at CCFE. Both have been instrumental in helping me produce this thesis, and to survive the trial of completing my PhD. Erwin stepped in to replace Prof. Arthur Peeters, my original supervisor, who left in my first year of study for Germany, and his good humour and reassurance has helped inspire and motivate me through the long, dark teatime of the soul that is a PhD programme. Samuli's knowledge and encouragement have helped guide me and give me a deeper understanding of the physics of tokamaks.

There are many people who, without their knowledge and skills, I would not have been able to complete this work. Dr. Ben McMillan has provided continuous help with bending NEMORB to my will and insights into plasma turbulence. Dr. Alberto Bottino and Thibaut Vernay have also contributed a great deal of knowledge and time to my understanding of NEMORB. The work done by Dr. Anthony Field and Young-chul Kim on the BES system, its synthetic diagnostic, and the analysis of the resulting data, has made this work possible. During my time at Culham, David Dickinson has proven to be a fountain of useful advice on physics and computers, and an invaluable sounding board, letting me bounce ideas off him until they metamorphosed into crystalline form. Over the last few years, I have benefitted from useful discussions with a large number of people, including M. Barnes, F. Casson, J. Cook, D. Edie, S. Freethy, D. Higgins, C. Roach, G. Szepesi, and C. Wrench; there are certainly others whom I have forgotten.

This work was funded partly by the RCUK Energy Programme under grant

EP/I501045 and the European Communities under the contract of Association between EURATOM and CCFE. The views and opinions expressed herein do not necessarily reflect those of the European Commission. This work was also funded by EPSRC and simulations were performed using the HPC-FF resource at the J ulich Supercomputing Centre, the HECTOR national resource, and the HELIOS supercomputer in Japan.

My parents and family deserve a significant proportion of my thanks for their love and support throughout my education, and for helping me deal with unexpected crises. Darren Aldous has helped me avoid bad faith through the years, yearn for eudaemonia, and generally been a friend of mine. I want to thank my friends outside of physics for their friendship and support, and for putting up with my impromptu lectures on physics. I have to give special thanks to Nicky for her companionship, humour, wisdom and love, especially through this last slog.

Declarations

I declare that the work presented in this thesis is my own except where stated otherwise.

This thesis has not been submitted, either wholly or in part, for a degree at any level at any other academic institution.

The majority of chapter 5 has been published in [1].

Abstract

The free energy in the large temperature and density gradients in tokamaks can drive microinstabilities, which in turn drive turbulence. This turbulence is responsible for the transport of energy and particles over and above that predicted by neoclassical theory. Sheared toroidal rotation can suppress the turbulence and stabilise the underlying microinstabilities, thereby reducing the transport. This thesis investigates how variation of the equilibrium temperature and density profiles, over the same scales associated with the microinstabilities, affects how the flow shear stabilises the linear modes and suppresses the turbulence. A global gyrokinetic code is employed in this investigation, which retains the profile variation and simulates the full 3D domain of a tokamak plasma.

How much flow shear is needed to stabilise the linear ion temperature gradient (ITG) mode is found to be dependent on its poloidal wavenumber, with longer wavelength modes needing more flow shear than the fastest growing mode. This dependence is present whether the flow shear is constant across the radius or if it has the variation typical in an experimental rotation profile. There is an asymmetry with respect to the sign of the flow shear in the effectiveness of the stabilisation, with the maximum linear growth rate occurring at finite negative shearing rates for the plasma studied here. This asymmetry arises from the profile variation, and is found to be significant in simulations of MAST L-mode plasmas, especially when the effects of kinetic trapped electrons are included in the simulations.

Flow shear asymmetry is still present in nonlinear simulations, and the suppression of fully-developed turbulence depends on the sign of the shearing rate. With the experimental rotation profile, the heat flux arising from ITG turbulence is reduced by an amount comparable to the reduction in the linear growth rates. When the direction of the rotation profile is reversed, such that the sign of the flow shear is flipped while the magnitude remains the same, the turbulence is almost completely suppressed. A new diagnostic on MAST, beam emission spectroscopy (BES), is used to make a direct comparison between density fluctuations from simulation, and from experiment. Collisionless, electrostatic simulations with rotation are found to disagree significantly with experiment in the level of ITG turbulence activity and the correlation times and lengths of the turbulence. The inclusion of electron-electron and electron-ion collisions into static simulations is enough to bring the level of turbulent density fluctuations down to within a factor two of the experimental levels, with the correlation lengths becoming comparable, while the correlation times remain an order of magnitude too large.

Chapter 1

Introduction

1.1 Motivation

We live in a world facing several crises symptomatic of our dependence on limited, environmentally damaging and incredibly useful fossil fuels - increasing geopolitical tension, global climate change, and irresponsible waste of resources[2]. Development of methods of energy production which do not rely on limited or easily monopolised resources has become a clear and pressing global goal[3]. Currently, the largest focus from both the public and private sectors worldwide is on so-called renewables - wind, solar, tidal, etc[4]. These work well on local scales, but suffer from severe limitations on national and international scales. The other major fossil fuel-alternative is nuclear fission. This method suffers from an almost crippling perception of being excessively dangerous with an unsolvable waste problem, as well as having its own legitimate concerns - proliferation of nuclear materials is an not-inconsiderable problem.

Fusion promises unlimited, clean and safe energy. Research has been underway since the 1950s, but the early optimism was tempered as experiments failed to live up to the dream. Some of that optimism is now returning, as we come to understand more and more of the physics of fusion plasmas and achieve more and more goals of the fusion experiment. We can produce fusion reactions - the next step is achieve self-sustaining reactions. This is hoped to be achieved using the internationally developed ITER, which is scheduled to have its first plasma in 2020. After ITER, a prototype power plant will be built, named DEMO. DEMO is hoped to produce net power out and demonstrate the commercial viability of fusion power.

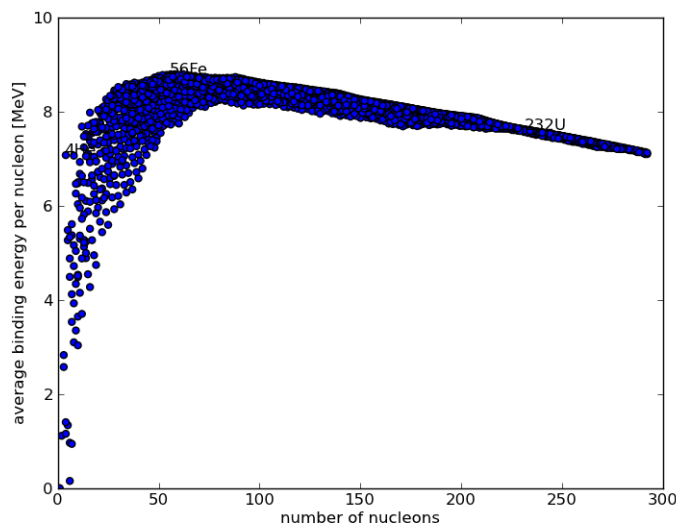


Figure 1.1: Binding energy per nucleon versus number of nucleons for all known nuclides. There is a peak in the binding energy at ^{56}Fe . Elements beyond this cannot be created through the usual stellar fusion reactions, and must be formed in the violent explosions of stars. Data for this figure was taken from [5]

1.1.1 What is fusion

Fusion happens when two nuclei come close enough that the strong force becomes dominant over the repulsive Coulomb force, binding them together. The resulting product has a smaller mass than the original nuclei as some of the mass is in the strong force holding the nucleons together, the binding energy, and the binding energy per nucleon is less in the product than in the reactants. The “missing mass” is released as energy. The binding energy is the energy required to separate a nucleus into its component nucleons. Figure 1.1 shows the binding energy per nucleon of all known nuclides, and it can immediately be seen that there is a peak in this graph. This means that fusion reactions up to ^{56}Fe are exothermic, and as such, all these elements can be produced in stars. Elements heavier than ^{56}Fe can only be created in supernovae and in laboratories on Earth. The most energetic fusion reactions are those that produce helium from isotopes of hydrogen.

The probability of a given fusion reaction occurring is measured by its cross-section. As mentioned above, reactions producing isotopes of helium release the most energy, and of these, deuterium-tritium \rightarrow helium-4¹ (hereafter referred to as D-T) has the largest cross-section (see fig. 1.2). For these reasons, D-T is the

¹A helium-4 ion is also known as an α particle

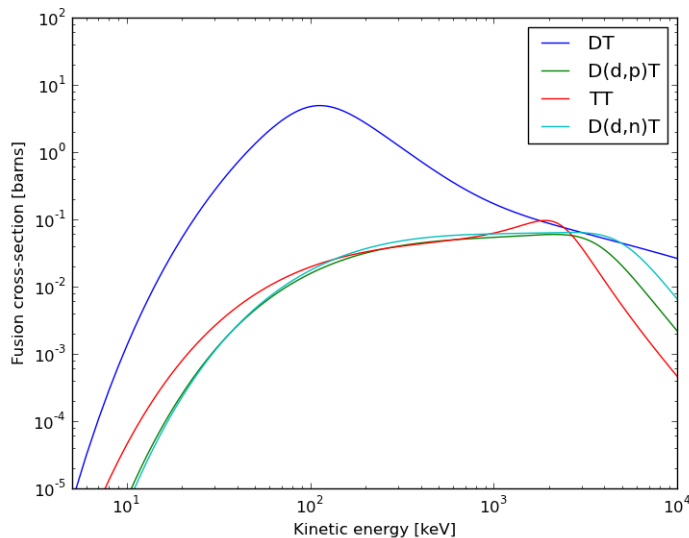


Figure 1.2: Fusion cross-sections for some common reactions as functions of energy: blue, DT; red, TT; green and turquoise, DD. Note the resonance of the DT reaction around 100 keV.

reaction most favoured by most fusion power plant designs.

Triple product

In a fusion power plant, it is essential that we can get more energy out than we put in. The power lost (P_L) through inefficiencies in the power generation, loss mechanisms internal to the plasma, etc., must be less than that put into the plasma through external heating (P_H) and self-heating by alpha particles (P_α). If the alpha-heating is equal to the power loss, then the plasma is said to have achieved ignition. The ignition condition is set by three parameters: the plasma temperature, density and energy confinement time, $\tau_E = \frac{W}{P_L}$, where W is the energy stored in the plasma. For a typical D-T reaction, the ignition condition is[6]:

$$nT\tau_E > 10^{21} \text{ m}^{-3} \text{ keV s}, \quad (1.1)$$

also known as the “triple product”. In tokamaks, the density has an upper limit (that depends on the plasma current), set by the Greenwald stability criterion[7], and the temperature has a small optimum range (see fig. 1.2), leaving only τ_E as a free parameter². The optimum range of temperature has a lower limit set by

²This only applies to tokamaks. In ICF, there are different limits to n and T , though the triple product still holds

the peak in the cross-section and an upper-limit set by the operating regime of the device. Increasing the temperatures means increasing the plasma pressure, which means magnetic field required to contain the plasma must also be increased (this is discussed in more detail in section 1.2.2). The energy confinement time is set by the transport of heat from the core of the plasma to the outside (see section 1.3 for more about transport).

1.2 Magnetic confinement

In order to have a sustainable reaction, it is necessary to hold the plasma together in one place long enough to confine the energy. There are three main methods of confining plasmas for fusion reactions - gravitational, inertial and magnetic. Gravitational confinement is used by stars. The huge mass of plasma contracts under its own gravity, increasing the temperature and pressure to levels where fusion is possible. The star needs enough mass to counteract the radiation pressure exerted by the energy released in its fusion reactions. The engine of stars is the p-p reaction, but because it is mediated by the weak interaction and has a small cross-section, this reaction is slow.

Inertial confinement uses lasers to heat a small pellet, ablating the outer layers. The resulting explosion causes the core to implode, creating high densities and pressures. This is one of the current leading efforts to achieve fusion power, with several state-of-the-art projects underway, namely NIF and HiPER.

Magnetic confinement is the other contender for fusion power. Because plasmas consist of electrically-charged particles, it is possible to confine them within magnetic fields. Charged particles in a magnetic field experience a force perpendicular to both the magnetic field and their velocity. This means that the particles gyrate in closed-orbits in the plane perpendicular to the magnetic field, given uniform, homogeneous fields. This motion is called the Larmor motion, and has a characteristic radius ρ_L (also called the Larmor radius, cyclotron or gyroradius):

$$\rho_L = \frac{mv}{qB}, \quad (1.2)$$

where m, v, q are the mass, velocity and electric charge respectively of the particle, and B is the magnetic field strength. The particle gyrates with a frequency $\Omega_c = qB/m$, (called the cyclotron frequency). Parallel to the magnetic field, particles can move freely. This immediately suggests a confinement mechanism: by bending the field lines round into a closed loop, we can keep the plasma trapped in our device. It

turns out that this by itself is not sufficient. It is necessary to also include a degree of helicity in the field lines in order to prevent system-scale instabilities[8]. For example, the ∇B drift causes the electrons and ions to move vertically in different directions, causing a separation of charge, leading to a massive loss of particles due to the $E \times B$ drift (see section 1.2.1 for an explanation of these drifts). There are two ways to achieve this helical field: either by using magnetic coils especially shaped to directly produce this field, or by driving part of the fields through a current in the plasma. The class of machines using the former approach are called stellarators, while the latter are called tokamaks (the Russian acronym of “toroidal chamber with magnetic coils”). The plasma current is usually driven by changing the electrical current through the central solenoid (so-called ohmic operation), meaning most tokamaks are inherently pulsed³. This is contrast to stellarators, whose design means they can be run almost indefinitely. However, the geometry of the stellarator field coils is exceedingly complicated, making them costly to design and build. The induced plasma current has a secondary benefit, in that it also heats the plasma. So far, the highest values of the triple product in magnetic devices have been in tokamaks.

1.2.1 Single particle motion

Charged particles in a magnetic field gyrate around the field lines with a characteristic radius, ρ_L and can be accelerated along the field either by parallel electric fields (E_{\parallel}) or the magnetic field strength decreasing along the field line ($\nabla_{\parallel} B$). Forces perpendicular to the magnetic field applied to the particles induce a drift which is perpendicular both to the field and to the external force. There is a simple physical picture to understand this motion, as illustrated in fig. 1.3. When the force is parallel to the particle’s instantaneous velocity, ρ_L is temporarily increased. When it is anti-parallel to the velocity, ρ_L is decreased. This combination causes a drift perpendicular to the applied force, \mathbf{F} of the general form:

$$\mathbf{v}_D = \frac{\mathbf{F} \times \mathbf{b}}{qB}, \quad (1.3)$$

where $\mathbf{b} = \mathbf{B}/B$ and B is the magnitude of the magnetic field.

The main drifts in a tokamak are due to the electric field and the curvature and (perpendicular) gradient of the magnetic field. The force due to the electric field depends on the charge of the particle - it is immediately clear that the resulting drift

³There are methods of driving the plasma current through other means, and the existence of the so-called “bootstrap current” means that it is possible to achieve 100% non-inductive current

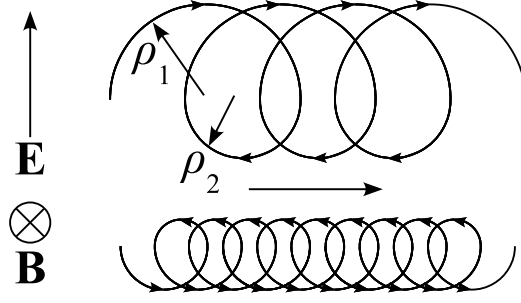


Figure 1.3: Charged particles in the presence of both a magnetic field and an electric field gyrate around a guiding centre which experiences a drift perpendicular to the two fields. This cartoon demonstrates how this drift arises. On one side of its orbiting, the particle has an increased gyroradius, ρ_1 , while on its other side, it is decreased, ρ_2 . The top spiral shows the motion of a positively charged ion, the bottom, an electron. Though the two species gyrate in opposite directions, the electric field accelerates them in opposite directions - the resulting $E \times B$ drift is independent of charge. The other drifts discussed in this section, however, do depend on charge, and so ions and electrons drift in opposite directions.

is independent of charge:

$$\mathbf{v}_{E \times B} = \frac{\mathbf{E} \times \mathbf{b}}{B}. \quad (1.4)$$

It can be seen that the perpendicular $E \times B$ drift is also independent of mass - ions and electrons feel the same drift in the same direction. Electric fields do not immediately lead to a charge separation, as might naïvely be expected.

On the other hand, curvature of the magnetic field and perpendicular gradients in the field do lead to separation of charges. The curvature drift comes about because particles following curved field lines experience a centrifugal force outwards, while the ∇B drift arises because the magnetic moment ($\mu = mv_{\perp}^2/2B$) of the particle is an adiabatically conserved quantity. That is, provided that the changes in the magnetic field are slow compared to the gyrofrequency and larger than the gyro-radius, the flux enclosed by the particle's orbit is almost constant. These two drifts have similar forms and are often combined into one expression:

$$\mathbf{v}_d = \frac{mv_{\parallel}^2 + \frac{1}{2}mv_{\perp}^2}{ZeB} \frac{\mathbf{b} \times \nabla B}{B}, \quad (1.5)$$

A time-varying electric field can also lead to a charge separation, which itself leads to the so-called polarisation drift. This has a slightly-different form to the previous drifts:

$$\mathbf{v}_p = \frac{m}{eB^2} \frac{d\mathbf{E}}{dt} \quad (1.6)$$

We can then decompose the motion of a particle into the gyro-motion about a guiding centre, its parallel motion along the field line and the perpendicular drifts. If we ignore the gyro-motion and instead concentrate on the motion of the guiding centre, \mathbf{X} , we get

$$\mathbf{v}_\mathbf{X} = v_\parallel \mathbf{b} + \mathbf{v}_d + \mathbf{v}_{E \times B} + \mathbf{v}_p. \quad (1.7)$$

The origins and mechanisms of heat and particle transport are discussed in-depth in section 1.3.

1.2.2 Tokamak equilibria

The helical field in tokamaks has two components: the toroidal field (B_φ), produced by the toroidal field coils; and the poloidal field (B_θ), produced by the plasma current and poloidal field coils. The shape of the helical magnetic field is such that the field lines lie in toroidal surfaces and are axisymmetric to within a few percent. We can define a convenient radial coordinate, ψ , as the poloidal magnetic flux within a magnetic surface. It can be shown that ψ is constant on a magnetic surface, i.e. that

$$\mathbf{B} \cdot \nabla \psi = 0, \quad (1.8)$$

so these surfaces are often called flux surfaces. From eq. (1.8), we get the following relations between the poloidal field and ψ :

$$B_R = -\frac{1}{R} \frac{\partial \psi}{\partial Z}, \quad B_Z = \frac{1}{R} \frac{\partial \psi}{\partial R}, \quad (1.9)$$

which along with Gauss' Law which requires:

$$\frac{1}{R} \frac{\partial}{\partial R} (R B_R) + \frac{\partial B_Z}{\partial Z} = 0, \quad (1.10)$$

where Z is the vertical direction in fig. 1.4.

Our most basic coordinate system for a tokamak is then (ψ, θ, φ) (see fig. 1.4). For convenience, we will often refer to “parallel” and “perpendicular” directions - these are understood to be relative to the magnetic field, \mathbf{B} , and lie within a flux surface (that is, the perpendicular direction is $\nabla \psi \times \nabla \varphi$). Note that “perpendicular” may also refer to the perpendicular plane - i.e. a poloidal cross-section of the plasma at constant φ .

In equilibrium, the pressure and Lorentz forces are in balance:

$$\mathbf{J} \times \mathbf{B} = \nabla p, \quad (1.11)$$

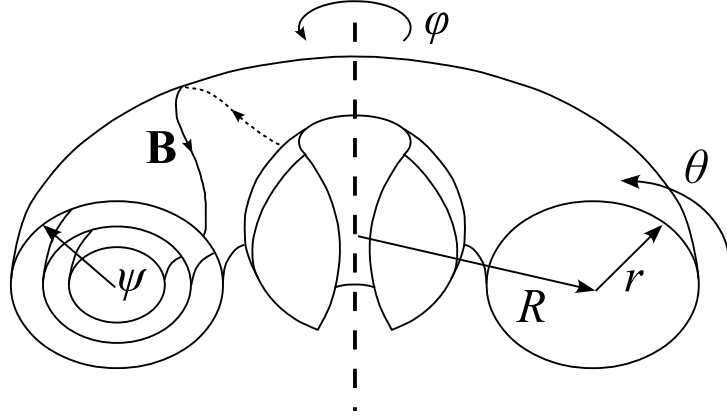


Figure 1.4: Illustration of the shape of two tokamak plasmas - the outer torus shows a large aspect-ratio plasma, with circular cross-section; the inner torus depicts a small aspect-ratio plasma. Also shown is the general coordinate system of a tokamak: the “long way round” the torus is the toroidal direction, φ ; the “short way round” is the poloidal dimension, θ . The vertical dashed line is the axis of symmetry. The minor radius, r , and major radius, R , as well as the flux surface label, ψ are indicated. A representation of the shape of the magnetic field, \mathbf{B} , is shown winding around a flux surface.

where \mathbf{J} is the plasma current density and p is the pressure. From this equation, it is immediately obvious both that $\mathbf{B} \cdot \nabla p = 0$ and that $\mathbf{J} \cdot \nabla p = 0$, and so both \mathbf{J} and \mathbf{B} lie on surfaces of constant pressure. This is made transparent when we introduce a current flux function, f , related to the poloidal current density by

$$j_R = -\frac{1}{R} \frac{\partial f}{\partial Z}, \quad j_Z = \frac{1}{R} \frac{\partial f}{\partial R}. \quad (1.12)$$

Using Ampère’s equation, we can then show that

$$f = \frac{RB_\varphi}{\mu_0}. \quad (1.13)$$

Given eq. (1.12) and eq. (1.11), it follows that

$$\nabla f \times \nabla p = 0, \quad (1.14)$$

and so, knowing that p is a function of ψ , it must be true that $f = f(\psi)$. Therefore, \mathbf{B} and \mathbf{J} are both flux functions, and we need only to use ψ as our flux function. Particles can travel rapidly along the field lines, as the thermal velocity in tokamak plasmas is of the order of 10^5 m s^{-1} , meaning that the equilibrium temperature and density are also flux functions.

The safety factor, q , is used to measure the degree of helicity of the magnetic field. More precisely, it is defined as:

$$q = \frac{1}{2\pi} \int_0^{2\pi} \frac{\mathbf{B} \cdot \nabla \varphi}{\mathbf{B} \cdot \nabla \theta'} d\theta'. \quad (1.15)$$

The safety factor is so-called because its profile determines some of the major stabilising properties of a tokamak equilibrium. Large, system-scale magnetohydrodynamic (MHD) instabilities become serious disruptive events when q drops below 3 at the edge, for example[9].

An important quantity in tokamaks is its plasma- β , the ratio of plasma thermal pressure, $p = nT$ to its magnetic pressure:

$$\beta = \frac{p}{B^2/2\mu_0}. \quad (1.16)$$

This is a dimensionless ratio which measures the efficiency of confinement due to the magnetic field. In tokamaks, β must necessarily be smaller than 1, as $\beta > 1$ means that the magnetic pressure is too small to balance the thermal pressure. Typically, it is only a few percent, though in spherical tokamaks, it may reach as much as 30%.

1.2.3 Magnetic mirroring and trapped particles

As mentioned above, particles moving into regions with increasing magnetic field strength experience a force parallel to the motion of their guiding centre. This is a consequence of the conservation of both the total kinetic energy, $\frac{1}{2}m(v_{\parallel}^2 + v_{\perp}^2)$, and the magnetic moment, μ . The magnetic moment is not strictly a constant of motion - rather, it is an adiabatic invariant, and remains constant provided the magnetic field changes slowly enough. That is, the spatial variation in the magnetic field should be larger than the Larmor orbit, and the temporal variations longer than the gyro-period. Provided these conditions are met, the magnetic moment will be conserved. The increase in B must be matched by an increase in v_{\perp}^2 to keep the flux enclosed by the particle's gyration constant. Then, to balance this, v_{\parallel} must correspondingly decrease. At some point in the particle's trajectory, the parallel velocity may become zero, and this "mirror force" will start to move the particle back the way it came. In order to overcome the mirror force, particles must have some minimum v_{\parallel} - these are called "passing" particles. Those who do not are termed "trapped" particles. In a tokamak, the toroidal magnetic field varies with major radius, roughly as $\sim 1/R$. As a particle follows a field line, it will see a stronger field on the inboard side (or low field side, closest to $R = 0$). It follows

that particles can be trapped on the outboard side (also called the high field side), bouncing between two points along a field line, if their v_{\parallel} is not large enough. The minimum v_{\parallel} can be shown to be given by:

$$v_{\parallel} > \sqrt{\frac{2\epsilon}{1-\epsilon}} v_{\perp}, \quad (1.17)$$

where $\epsilon = r/R_0$ is the inverse aspect-ratio at the particle's position, and R_0 is the major radius of the magnetic axis (where $B_{\theta} \rightarrow 0$). In addition to this trapped motion, particles also experience a deviation from the flux surfaces due to conservation of the canonical momentum, $p_{\varphi} = mRv_{\varphi} + q\psi$. It is obvious that changing v_{\parallel} must lead to a change in ψ . The size of the excursion from the flux surface can be calculated, and the width of a banana orbit, w_b can be shown to be:

$$w_b = \frac{q}{\sqrt{\epsilon}} \rho_L. \quad (1.18)$$

Importantly, two particles of the same species with different signs of v_{\parallel} drift to different sides of a flux surface. Several significant effects arise because of this. Firstly, at a given radius and assuming a density gradient, there will be more particles with one sign of v_{\parallel} than the other. This leads to a the so-called diamagnetic drift, as there are more particles moving in one direction. The sign of this drift is different for ions and electrons. The second effect of the banana orbits is the bootstrap current. The trapped particles carry some parallel current due to their motion along the field lines. Friction between the trapped and passing particles then leads to another, larger current carried by the passing particles, which is known as the bootstrap current. Bootstrap currents are important because it is possible to use them to replace some or all of the induced plasma current to maintain the poloidal field, and as such, could be used in future steady-state devices.

1.3 Transport in tokamaks

Why don't tokamaks work? Early research suggested that a working reactor could be built by 1970[8]. The reason for this overly-optimistic prediction was the underestimation of transport. The transport of heat, energy and particles determine the confinement times of the respective properties and early theories were based around collisions mediating the transport ("neo-classical theory" - see section 1.3.1). The observed transport turned out to be an order or magnitude larger than predicted - and it was this so-called "anomalous" transport which has stymied the achieve-

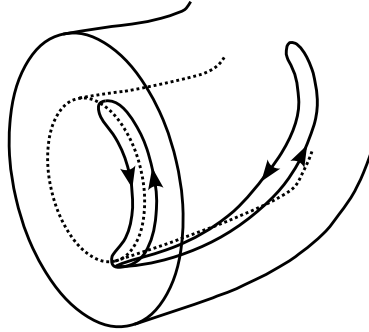


Figure 1.5: Particles can become trapped on the low-field side by magnetic mirror effects. The shape of their orbits, projected onto the poloidal plane, have a characteristic banana shape (the gyro-motion of the particles is not shown here). In this example, following the particle from its lowest point, it experiences a vertical drift downwards which pulls it off the flux surface (dotted line). As it travels anti-clockwise, it crosses the outboard mid-plane, at which point, the vertical drift pulls it back to the flux surface. As it reaches the top of its orbit, its v_{\parallel} reverses and the vertical drift now pulls it below the flux surface.

ment of ignition. We now know that turbulence is responsible for the anomalous transport, and the study and control of turbulence has preoccupied not only the fusion community, but indeed modern physics, and it remains one of the great open problems of science.

1.3.1 Classical and neoclassical theory

The most basic transport mechanism is a purely collisional diffusive process. We can calculate the magnitude of the diffusion coefficient, D , of this process from a simple random walk model. We get that $D \sim (\Delta x)^2 / \Delta t$, where Δx is the step size and Δt is the time scale of the collisions. In a tokamak, the step length is the gyroradius, so:

$$D \sim \rho_L^2 \nu, \quad (1.19)$$

where ν is the collision frequency. If confinement were limited solely by this simple diffusion, then the confinement time would be

$$\tau \sim \frac{a^2}{D} = \left(\frac{a}{\rho_L} \right)^2 \frac{1}{\nu}. \quad (1.20)$$

It is important to note here that collisions between two particles of the same species will produce no net transport of particles. It is collisions between ions and electrons that set the level of transport, and so the relevant step length is actually the Larmor

radius of the electrons, ρ_e , and the collision frequency is that of electron-ion collisions, ν_{ei} ⁴. However, diffusion of heat is different - collisions between like species can exchange energy, and so can transport heat. Therefore, the heat diffusivity of ions, χ_i , is greater than that of electrons, χ_e , by factor of the square root of the mass ratio:

$$\chi_i \sim \sqrt{\frac{m_i}{m_e}} \chi_e. \quad (1.21)$$

Given a typical electron-ion collision rate of $0.1 - 1 kHz$, and $\rho_e \sim 1 \text{ mm}$, $a \sim 1 \text{ m}$, the confinement time from this simple diffusion process would be on the order of an hour. This shows the source of the optimism in early fusion experiments - a device only a metre across could be sufficient to meet the energy demands of an entire city.

The collisional process outlined above changes dramatically when we include the magnetic geometry of a tokamak. Diffusion coefficients can increase by several orders of magnitude. We call the collisional theory that includes effects derived from tokamak geometry “neoclassical” to differentiate it from the picture above, which is called “classical”. The first big effect arises from trapped particles undergoing banana orbits (see fig. 1.5). The step size of the diffusive process then becomes the width of this banana orbit, rather than the gyroradius. However, because only a fraction, $\sim \sqrt{\epsilon}$, of particles are actually trapped and in banana orbits, so the effective diffusivity is actually

$$D_{eff}^{ban} \sim \frac{q^2}{\epsilon^{3/2}} \rho_e^2 \nu_{ei}. \quad (1.22)$$

Again, the electron and ion particle diffusion rates cannot be different, whereas the heat diffusivities differ between species by a factor $\sqrt{\frac{m_i}{m_e}}$. This process is only important at low collisionality, where particles complete at least one orbit before they are scattered. At higher collisionalities, where the collisional frequency becomes comparable to the bounce frequency, different mechanisms dominate the diffusion. Two regimes exist for higher collisionalities - the plateau regime, where the diffusivity no longer depends on collisionality, and the Pfirsch-Schlüter regime, which has a weaker dependence on ν than the banana regime[9]. However, due to the high temperatures in tokamaks, they have rather low collisionalities and so only the banana regime is of interest⁵.

⁴In this thesis, we will denote quantities peculiar to electrons or ions with a subscript e or i , respectively. Ions are assumed to be deuterium ions, unless otherwise stated

⁵MAST, for example, is firmly in the banana regime

1.3.2 Anomalous transport and turbulence

The strong gradients in temperature and density in tokamaks provide large amounts of free energy. As a result, there is a whole zoo of instabilities that can tap this energy and drive increased transport of heat and particles. Large, system-scale instabilities tend to affect the stability of the plasma equilibrium itself, therefore, for stable equilibria, it is the smaller scale so-called “microinstabilities” that are the most important to consider. Chapter 3 shows the main class of microinstabilities, drift waves, are linearly driven. When they reach a certain amplitude, the microinstabilities can start to nonlinearly interact and the plasma becomes turbulent. In experiment, the linear growth phase is never seen - we only see turbulent fluctuations in density, temperature, magnetic field, etc. Fluctuations in density, δn , cause fluctuations in the electrostatic potential, $\delta\phi$, which in turn produces an $E \times B$ velocity (this is discussed in more depth in chapter 3):

$$\delta v_{\perp} = \frac{\delta E_{\perp}}{B}. \quad (1.23)$$

From this fluctuating velocity, and the original density fluctuation, a convective flux arises:

$$\Gamma = \langle \delta v_{\perp} \delta n \rangle, \quad (1.24)$$

where the angular brackets signify an average over a flux surface. How these fluctuations arise and interact will be discussed in more detail in chapter 3. Fluxes for the ions from fluctuations turned out to be an order of magnitude or more larger than neoclassical predictions[9]. More than this, heat fluxes for the electrons were the same level as those for the ions - in direct contradiction to before. We can glean the reason for this from a mixing length argument, which is simply that the microinstabilities stop growing when their linear growth rate, γ , is balanced by the rate at which they are dissipated. This turns out to be the turbulent diffusion rate, which for a perpendicular wavenumber k_{\perp} is given by : $\gamma_D \sim k_{\perp}^2 D$ [10]. Rearranging, we get the quasilinear turbulent diffusion coefficient:

$$D \sim \frac{\gamma}{k_{\perp}^2}. \quad (1.25)$$

Electron-scale microinstabilities, despite having a much shorter wavelength, have vastly larger growth rates than their ion-driven counterparts. This accounts for the dramatic increase in electron heat diffusivity.

1.4 The MAST device

1.4.1 Spherical tokamaks

Spherical tokamaks (STs) are a class of device with a small aspect-ratio, $R_0/a \sim 1$, where a is the minor radius of the largest flux surface (cf. the typical aspect-ratio of a conventional tokamak of ~ 2.5). They are often likened to a “cored-apple” rather than the “doughnut” or “bagel” of larger aspect-ratio machines (see fig. 1.4 for an illustration of the difference). The small aspect-ratio means that STs can have a high fraction of trapped particles. This makes them susceptible to microinstabilities that are driven by trapped particles, but it also means they can have larger bootstrap currents (toroidal currents driven by particles in banana orbits). Their low moment of inertia means that STs can be easily spun up to high rotation rates by injected neutral beams. This makes them an ideal place to study the effects of strong flows.

Because of their size, STs have a smaller potential as power sources, as fusion power scales with volume[11]. However, their size does mean that the neutron fluxes will be much higher. There are plans to use STs as “component test facilities”, where materials can be subject to large neutron fluxes, simulating conditions in larger machines.

The main advantage of spherical tokamaks is that, due to their size and shape, it is possible to achieve higher a plasma- β than conventional aspect ratio tokamaks[11]. This means that they can use a smaller toroidal field to confine a given kinetic pressure. As one of the biggest costs of running a tokamak is the production of the magnetic field, this means that STs would be cheaper to build and run for the same fusion power.

1.4.2 Local vs. global analysis

Over the years, there have been many different models and frameworks used to advance our understanding of plasmas. One of the first attempts was the MHD, single conducting fluid model. As will be covered in chapter 3, the correct, separate treatment of electron and ion dynamics is necessary to understand microinstabilities[12]. It is possible to use two fluid models to recover many of the qualitative features of microinstabilities. However, the features of turbulence and microinstabilities themselves suggest a different approach: gyrokinetics. Chapter 2 will describe the gyrokinetic formalism and derive the relevant equations. We restrict ourselves to the collisionless and electrostatic limit. For details of collisional terms see [13] and for electromagnetic terms, see [14].

The study of turbulence often involves many different scales - which the

gyrokinetic approach utilises. A common assumption is that the normalised gyro-radius, $\rho_* = \rho_i/a$, becomes vanishingly small. In this limit, usually called the “local” limit, it can be assumed that flux surfaces are independent of each other. Numerical codes which use this limit (hereafter referred to as local codes) make the assumption that equilibrium quantities and their derivatives are constant across the simulation domain, e.g. T_0 and $dT_0/d\psi$ both take a single, constant value at all points in the simulation. This approach is valid in the limit $\rho_* \rightarrow 0$ as the simulation is only looking at an infinitesimally thin slice of the whole system. In large aspect-ratio devices, such as JET or ITER, this limit is a good assumption. We can check this by looking at quantities which vary with ρ_* , such as the growth rate of a particular instability. Figure 1.6 shows that $\rho_* = 1/500$ means that the local approximation

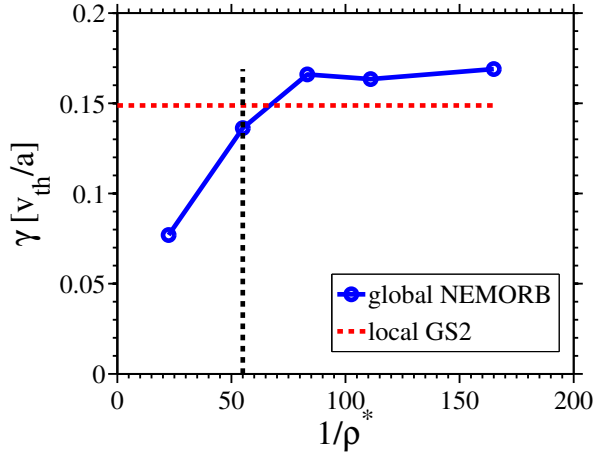


Figure 1.6: Variation of the growth rate of the ITG mode with ρ_* , the normalised gyro-radius. The value of ρ_* on the MAST device are indicated. Figure taken from [15]

is a good assumption for JET plasmas. Local codes may have simulation domains of the order $100\rho_i$ in the “radial” direction⁶. However, MAST can have $\rho_* \sim 1/50$, and so these local codes may have radial domains larger than the MAST machine. This large ρ_* means that it is necessary to use a numerical code which captures the full radial variation of equilibrium quantities. Codes which keep variation of the equilibrium profiles are called “global codes”. We will show in chapter 5 that retaining profile variation can have significant effects on the predictive abilities of numerical codes.

Another important feature of MAST is that it has a small aspect-ratio and

⁶This is perhaps not an entirely fair comparison, as local codes do not attempt to investigate any radial dependence within a single simulation. It is true, however, that they do attempt to simulate phenomena with some radial structure.

highly shaped flux surfaces. This means that in addition to profile effects, geometry effects are also important - it is not possible to make the “large aspect-ratio” ($R/a \gg 1$) assumption, where

$$q = \frac{rB_\varphi}{R_0B_\theta}. \quad (1.26)$$

This assumption turns out to be convenient for reducing the complexity of many equations in tokamaks, such as the formulae for the magnetic equilibria. Because MAST has a small aspect-ratio, the full expression for q must be used (see eq. (1.15)), and the magnetic equilibrium quantities are often two dimensional functions of (ψ, θ) . Geometry effects are not limited to global codes, and many local codes do include them. Simple models for the magnetic equilibrium, such as s - α or circular cross-sections, are ruled out though.

The numerical code, NEMORB, used in this thesis to study MAST plasmas has all of these effects. It is a global code, solving the full 3D domain, with realistic geometry taken from experimental data. The physical model used is gyrokinetics, where the rapid gyro-motion of particles is averaged over, reducing the problem by one dimension. Gyrokinetics is discussed in more detail in chapter 2. During the undertaking of the work in this thesis, the code was in a state of development, and had only electrostatic fluctuations. In general, due to their relatively high β , electromagnetic effects are important in STs. However, simulations using the local gyrokinetic code GS2 show that while for H-mode discharges, electromagnetic effects are indeed crucial, they are not as important for L-mode shots[16], such as the one studied in this thesis. Electromagnetic effects have recently been included in NEMORB[14], and further work will incorporate these.

1.5 Outline

This introduction has given a sketch of some of the important physics in tokamaks. The rest of this thesis presents a more in-depth study of a few of the more important pieces necessary to understand the work presented herein. The reader’s attention is directed to [8, 9, 17, 18] for more detail on tokamak equilibria and possible magnetic geometries, and to [19, 20, 21] for a more complete understanding of transport in tokamaks. The MAST physics reports, [22, 23], outline many of the past and current physics problems and studies of the MAST device.

The main body of work of this thesis is presented in chapters 5 to 7. Chapter 5 introduces background toroidal rotation to linear simulations of MAST plasmas and investigates how these flows affect the spectrum of wavenumbers present in

the machine. The next two chapters focus on nonlinear simulations. At first, in chapter 6, we include only the background rotation, and explore its effect on heat and momentum transport. Then, in chapter 8, a synthetic diagnostic is used to compare the simulations to real experimental data. Additional physics, in the form of collisions, are also included.

Chapter 2 derives the model used in NEMORB, while chapter 4 discusses the coordinate system, equations used and assumptions made in the code. The physics of microinstabilities, how they are driven unstable and how they are suppressed are described in chapter 3, as well as the types studied in this thesis.

Chapter 2

Gyrokinetics

2.1 Introduction

The magnetic field in tokamaks separates the plasma into two distinct regions, separated by the “separatrix”. The Last Closed Flux surface (LCFS) defines the boundary, although in reality, this is not a sharp transition. Outside of the separatrix field lines are “open”, ending on the divertor of the tokamak¹. The plasma in this region is characterised by low densities and temperatures which also can have variation along the field lines, as well as large fluctuations[24]. By contrast, inside the separatrix (the “core”), field lines are closed and the plasma here has much higher densities and temperatures (which remain flux functions), and comparatively small fluctuations[24]. They are non-relativistic ($v_{th} \ll c$), classical (degeneracy condition), fully ionised and fulfil the quasi-neutrality condition[9]. While the edge of a tokamak plasma (the region close to the LCFS) contains a great deal of interesting physics, and sets the boundary conditions for the core, this thesis deals exclusively with the core.

The large number of particles in a tokamak plasma all generate their own electromagnetic fields, which interact with every single other particle in the plasma. This clearly necessitates a statistical description for the evolution of the plasma. The particles are distributed in a six dimensional phase space, according to the distribution function $f_s(\mathbf{x}, \mathbf{v}, t)$ for species s , with spatial coordinates \mathbf{x} , and velocities \mathbf{v} . The mass continuity equation tells us that the mass flow out of a closed volume is equal to the rate of change of mass density in that volume. By analogy, we can construct a similar continuity equation for the distribution function - Liouville’s theorem states that the flow out of a closed volume of phase space is equal to the

¹An area of the first wall designed to withstand large heat fluxes.

rate of change of the probability density:

$$\frac{\partial f_s}{\partial t} + \frac{d\mathbf{x}}{dt} \cdot \nabla f_s + \frac{d\mathbf{v}}{dt} \cdot \frac{\partial f_s}{\partial \mathbf{v}} = 0, \quad (2.1)$$

where we have assumed that there are no sources or sinks of particles, and that there are no collisions. The coupling between species is therefore mediated solely by the electromagnetic fields. This is known as the Vlasov equation[9] and by itself is not enough to fully describe the complex behaviour of plasmas. Maxwell's equations provide the rest of the physics needed to describe all the phenomena present in the core of tokamak plasmas.

Unfortunately, the Vlasov-Maxwell system of partial differential equations is not tractable analytically for most plasmas of interest, and is not even numerically tractable for real world plasmas. In order to have a chance at solving these equations, we must make assumptions and simplify the system.

Over the years, there have been many different models and frameworks used to advance our understanding of plasmas. One of the first models was the MHD, single conducting fluid². This model has been employed to great success over the years, and is still used for many plasma calculations, especially those involving the equilibrium structure and major instabilities. However, there are some plasma phenomena that this model is unable to deal with. As will be covered in chapter 3, the correct, separate treatment of electron and ion dynamics is necessary to understand microinstabilities. It is possible to use two fluid models to recover many of the qualitative features of microinstabilities. However, the features of turbulence and microinstabilities themselves suggest a different approach: gyrokinetics. This chapter will describe the gyrokinetic formalism and derive the relevant equations. We restrict ourselves here to the collisionless and electrostatic limit as this is the regime in which all the work in this thesis has been performed. For details of collisional terms see [13] and for electromagnetic terms, see [14].

2.2 Gyrokinetic ordering

Gyrokinetics is motivated by the large range of temporal and spatial scales found in fusion reactors. Time scales vary from the cyclotron frequency ($\Omega_{ci} \sim 10^8$ Hz, $\Omega_{ce} \sim 10^{11}$ Hz) up to shot times (100 s), eventually up to steady-state reactors (months +). Spatial scales vary from the Larmor radius ($\rho_i \sim 1$ mm $\rho_e \sim 0.01$ mm) up to the system size ($L \sim 1$ m). This large variation in scales is a challenge for

²See [12] for a good history of tokamak transport models.

theory and simulations. Fortunately, most of the scales are well separated, and we can use this to our advantage. The gyrofrequency is much faster than almost all of the physics of interest - for example, the typical turbulence frequency is of the order 100 kHz[25]³. Knowing this (and the orderings given below), we can average over the fast gyromotion of the particles. This is the heart of gyrokinetics. Removing the rapid gyrations of particles is equivalent to reducing the dimensionality of the system and we move from a phase space with six dimensions (three of space, three of velocity), to one with five - losing a dimension of velocity.

More formally, we can define a small parameter, ϵ_ω , that reflects that the frequency of the fluctuating quantities, ω we are interested in is much slower than the cyclotron frequency:

$$\frac{\omega}{\Omega_c} \sim \epsilon_\omega \ll 1. \quad (2.2)$$

It is also possible to separate spatial scales, as long as the gradient of the magnetic field is much longer than the Larmor radius. We can define another small parameter:

$$\frac{\rho_i}{L_B} \sim \epsilon_B \ll 1, \quad (2.3)$$

where L_B is the logarithmic gradient length scale of the magnetic field

$$\frac{1}{L_B} = |\nabla \ln B| = \left| \frac{\nabla B}{B} \right|. \quad (2.4)$$

We also require that the length scales of the background equilibrium quantities, such as the temperature, T , and density, n , are of the same order

$$\frac{\rho_i}{L_n} \sim \frac{\rho_i}{L_T} \sim \epsilon_B. \quad (2.5)$$

The amplitude of fluctuations in the bulk density, δn , and electrostatic potential, $\delta\phi$ in tokamaks is typically much smaller than the magnitude of the equilibrium quantities. This represents a third small parameter:

$$\frac{\delta n}{n} \sim \frac{e\delta\phi}{T} \sim \epsilon_\delta \ll 1. \quad (2.6)$$

Note that throughout this thesis, the temperature is given in units of energy, i.e. $T = k_B T_K$, where T_K is the temperature in Kelvin and k_B is the Boltzmann constant. Given these three small parameters, we can expand all the relevant equations in them, keeping only the terms up to a certain order. This reduces the computa-

³Waves faster than the cyclotron frequency do exist in plasmas (EM radiation, for example), but their effects on turbulence are small in tokamaks.

tional effort required to simulate a plasma, while ensuring that errors are still small compared to the physics.

In general, the different small parameters are assumed to be the same order:

$$\epsilon_\omega \sim \epsilon_B \sim \epsilon_\delta, \quad (2.7)$$

however, one of the advantages of the gyrokinetic ordering is that this can be altered if need be. Additional orderings may also be introduced, without destroying the structure already in place.

2.3 Lie formalism

The Lie formalism ensures that the conservation laws are preserved throughout the transformation from real space to gyro-space. This guarantees a solid mathematical foundation for the whole system, and maintains energy and momentum conservation even to the lowest order in the expansion. The Lie-Transform method involves two changes of coordinates: the first, from the real space coordinates of the particle (\mathbf{x}, \mathbf{v}) to the guiding centre coordinates $(\mathbf{X}, v_\parallel, \mu, \alpha)$; then from the guiding centre frame to the gyro-centre frame $(\bar{\mathbf{X}}, v_\parallel, \bar{\mu}, \bar{\alpha})$. Figure 2.1 illustrates the particle and guiding centre frames. The difference between the guiding centre and gyro-centre frames is the inclusion of the perturbed fields in the latter. Because the length scales of the perturbed fields can be the same size as the gyroradius, they modify the gyromotion, destroying the conservation of μ . The Lie-Transform method is based around the Hamiltonian formulation, using a series of “near-identity” transformations and the freedom of gauge invariance to remove the rapid gyromotion and define a new quantity $(\bar{\mu} = \mu_0 + \mu_1 + \dots)$ which is conserved. These transformations are formally an asymptotic expansion in powers of the small parameter ϵ_δ , defined in eq. (2.6), and can be formulated out to any arbitrary order, with the zeroth order (the guiding centre transformation) being expressed in terms of ϵ_B . It is usually sufficient to derive them only to second order⁴.

The derivation of the equations proceeds as follows:

- i) formulate the Lagrangian in particle space, \mathbf{x} (section 2.3.1),
- ii) transform the Lagrangian to guiding centre space, \mathbf{X} (section 2.3.2),

⁴This is currently subject to some controversy[26]. For some formulations of gyrokinetics, it may be necessary to derive the equations out to third or fourth order in order to ensure consistency in the momentum transport. However, the simulating fourth order terms accurately is a significant challenge.

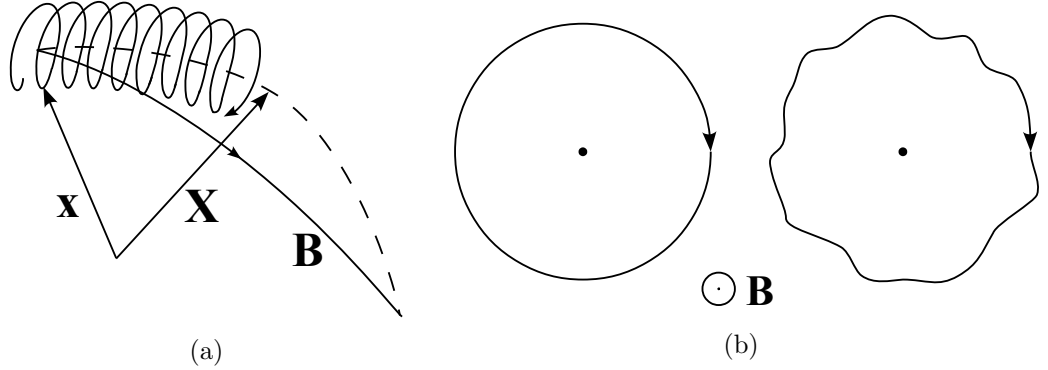


Figure 2.1: Schematic of the gyrokinetic framework. a) A charged particle gyrates around a field line, \mathbf{B} , and drifts cause the guiding centre motion (dashed line) to move off the field line. The particle's position vector is indicated by \mathbf{x} , while the position vector of the guiding centre is \mathbf{X} . b) The difference between the guiding- and gyro-centre coordinates is the inclusion of the perturbed fields in the gyro-centre frame.

iii) use a Lie transform to move to gyro-centre space, $\bar{\mathbf{X}}$ (section 2.3.3),

iv) derive the gyro-form of the Poisson equation (section 2.5).

2.3.1 Lagrangian in particle space

We first formulate the Lagrangian in the particle space, \mathbf{x} . We use Einstein notation, where pairs of repeated indices imply a summation over those indices. Latin indices are over spatial coordinates, and Greek indices over spatiotemporal coordinates, i.e.

$$\begin{aligned} i, j &\in \{1, 2, 3\} \\ \mu, \nu &\in \{1, 2, 3, 4\} \end{aligned} \tag{2.8}$$

The Lagrange equations of motion (for a single particle) are:

$$\frac{d}{dt} \frac{\partial \mathcal{L}}{\partial \dot{q}_i} - \frac{\partial \mathcal{L}}{\partial q_i} = 0, \tag{2.9}$$

where (\mathbf{q}, \mathbf{p}) are canonical variables and the Lagrangian is

$$\mathcal{L} = \mathbf{p} \cdot \dot{\mathbf{q}} - H_c(\mathbf{q}, \mathbf{p}, t). \tag{2.10}$$

We can then generalise this to an arbitrary phase space, $\mathbf{z} = \mathbf{z}(\mathbf{q}, \mathbf{p}, t)$:

$$\mathcal{L} = \gamma_i \dot{z}_i - H \tag{2.11}$$

The Poincaré-Cartan fundamental one-form is

$$\gamma \equiv \mathcal{L}dt = \gamma_i dz^i - Hdt \equiv \gamma_\mu dz^\mu \quad (2.12)$$

Then for a given coordinate transformation: $Z^\mu = Z^\mu(\mathbf{z}, t)$

$$\gamma = \gamma_\mu dz^\mu = \Gamma_\mu dZ^\mu, \quad (2.13)$$

where

$$\Gamma_\mu = \gamma_\nu \frac{\partial z^\nu}{\partial Z^\mu} \quad (2.14)$$

We can then form the Euler-Lagrange equations:

$$\hat{\omega}_{ij} \frac{dz^j}{dt} = \frac{\partial H}{\partial z_i} + \frac{\partial \gamma_i}{\partial t}, \quad (2.15)$$

where

$$\hat{\omega}_{ij} = \frac{\partial \gamma_j}{\partial z_i} - \frac{\partial \gamma_i}{\partial z^j} \quad (2.16)$$

are the components of the 8×8 antisymmetric Lagrangian tensor, also called the symplectic structure⁵.

The Euler-Lagrange equations are invariant under gauge transformation:

$$\gamma = \gamma + dS \quad \forall S(\mathbf{z}) \quad (2.17)$$

The canonical Hamiltonian for a single charged particle in a magnetic field with a perturbed electrostatic field, ϕ , is

$$H(\mathbf{q}, \mathbf{p}, t) = \frac{1}{2m} [\mathbf{p} - e\mathbf{A}(\mathbf{q})]^2 + e\phi(\mathbf{q}, t), \quad (2.18)$$

where \mathbf{A} is the vector magnetic potential.

We now specify our coordinates as:

$$\begin{aligned} \mathbf{x} &= \mathbf{q} \\ \mathbf{v} &= \frac{1}{m}(\mathbf{p} - e\mathbf{A}). \end{aligned} \quad (2.19)$$

⁵This essentially means that volumes in $6D$ phase space are conserved under a given transformation

Our one-form is now:

$$\begin{aligned}\gamma &= \gamma_i dz^i - H dt \\ &= [e\mathbf{A}(\mathbf{x}) + m\mathbf{v}] \cdot d\mathbf{x} - \frac{1}{2}mv^2 dt - e\phi(\mathbf{x}, t)dt\end{aligned}\quad (2.20)$$

$$= \gamma_0 + \delta\gamma, \quad (2.21)$$

where

$$\gamma_0 = [e\mathbf{A}(\mathbf{x}) + m\mathbf{v}] \cdot d\mathbf{x} - \frac{1}{2}mv^2 dt, \quad \delta\gamma = -e\phi(\mathbf{x}, t)dt \quad (2.22)$$

are the zeroth order and perturbed one-forms respectively.

2.3.2 Guiding centre transformation

Transformation into the guiding centre-frame is done using the following relationships to real space:

$$\mathbf{x} = \mathbf{X} + \boldsymbol{\rho}(\mathbf{X}, \alpha), \quad (2.23)$$

$$v_{\parallel} = \mathbf{v} \cdot \mathbf{b}(\mathbf{x}), \quad (2.24)$$

$$\mu = \frac{mv_{\perp}^2}{2B(\mathbf{x})}, \quad (2.25)$$

$$\alpha = \tan^{-1} \left(\frac{\mathbf{v} \cdot \hat{\mathbf{e}}_1}{\mathbf{v} \cdot \hat{\mathbf{e}}_2} \right), \quad (2.26)$$

where

$$\boldsymbol{\rho}(\mathbf{X}, \alpha) = \rho(\mathbf{x})\mathbf{g}, \quad (2.27)$$

$$\mathbf{g} = [\hat{\mathbf{e}}_1 \cos \alpha - \hat{\mathbf{e}}_2 \sin \alpha], \quad (2.28)$$

and $\boldsymbol{\rho}$ is the gyroradius vector pointing from the guiding centre to the particle's position, $\hat{\mathbf{e}}_{1,2}$ are arbitrary orthogonal unit vectors in the plane perpendicular to $\mathbf{b} = \mathbf{B}/B$, the magnetic field unit vector.

Using the above relations, expanding the vector potential about $\mathbf{x} \simeq \mathbf{X}$, and dropping terms beyond first order, we get:

$$\mathbf{A}(\mathbf{x}) = \mathbf{A}(\mathbf{X}) + \frac{v_{\perp}}{\Omega} \mathbf{g} \cdot \nabla \mathbf{A}, \quad (2.29)$$

$$d\mathbf{x} = d\mathbf{X} + \frac{1}{\Omega} \mathbf{g} dv_{\perp} + \frac{v_{\perp}}{\Omega} \mathbf{h} d\alpha, \quad (2.30)$$

where we have used $d\mathbf{g} \cong \mathbf{h} d\alpha$, with $\mathbf{h} = -\sin \alpha \hat{\mathbf{e}}_1 - \cos \alpha \hat{\mathbf{e}}_2$. the zeroth order part

of eq. (2.20) using eqs. (2.29) and (2.30), we get the guiding centre one-form:

$$\begin{aligned}\Gamma_0 = & \left\{ e\mathbf{A}(\mathbf{X}) + \frac{ev_\perp}{\Omega}(\mathbf{g} \cdot \nabla \mathbf{A}) + m\mathbf{v} \right\} \cdot d\mathbf{X} \\ & + \left\{ \frac{e}{\Omega}\mathbf{A}(\mathbf{X}) \cdot \mathbf{g} + \frac{ev_\perp}{\Omega^2}(\mathbf{g} \cdot \nabla \mathbf{A}) \cdot \mathbf{g} + \frac{m}{\Omega}(\mathbf{v} \cdot \mathbf{g}) \right\} dv_\perp \\ & + \left\{ \frac{ev_\perp}{\Omega}\mathbf{A}(\mathbf{X}) \cdot \mathbf{h} + \frac{ev_\perp^2}{\Omega^2}(\mathbf{g} \cdot \nabla \mathbf{A}) \cdot \mathbf{h} + \frac{mv_\perp}{\Omega}(\mathbf{v} \cdot \mathbf{h}) \right\} d\alpha \\ & - (\tfrac{1}{2}mv_\parallel^2 + \mu B)dt.\end{aligned}\tag{2.31}$$

This form of the Lagrangian still contains dependencies on α (terms containing \mathbf{g}, \mathbf{h}). We are free to choose the gauge thanks to eq. (2.17), so we choose

$$S = -\frac{ev_\perp}{\Omega}\mathbf{g} \cdot \mathbf{A} - \tfrac{1}{2}\frac{ev_\perp^2}{\Omega^2}(\mathbf{g} \cdot \nabla \mathbf{A}) \cdot \mathbf{g},\tag{2.32}$$

$$\begin{aligned}\Rightarrow dS = & -\frac{e}{\Omega}\left[(\mathbf{g} \cdot \mathbf{A})dv_\perp + v_\perp(\mathbf{A} \cdot \mathbf{h})d\alpha + v_\perp(\mathbf{g} \cdot \nabla \mathbf{A}) \cdot d\mathbf{X}\right] \\ & - \frac{ev_\perp}{\Omega^2}(\mathbf{g} \cdot \nabla \mathbf{A}) \cdot \mathbf{g}dv_\perp - \tfrac{1}{2}\frac{ev_\perp^2}{\Omega^2}\left[(\mathbf{h} \cdot \nabla \mathbf{A}) \cdot \mathbf{g} + (\mathbf{g} \cdot \nabla \mathbf{A}) \cdot \mathbf{h}\right]d\alpha\end{aligned}\tag{2.33}$$

and combine this with eq. (2.31) to give

$$\begin{aligned}\Gamma_0 = & \left\{ e\mathbf{A}(\mathbf{X}) + mv_\parallel \mathbf{b} \right\} \cdot d\mathbf{X} + \tfrac{1}{2}\frac{ev_\perp^2}{\Omega}\left\{ (\mathbf{g} \cdot \nabla \mathbf{A}) \cdot \mathbf{h} - (\mathbf{h} \cdot \nabla \mathbf{A}) \cdot \mathbf{g} \right\} d\alpha \\ & + \frac{mv_\perp}{\Omega}(\cos \alpha - \sin \alpha)dv_\perp - \frac{mv_\perp^2}{\Omega}(\cos \alpha + \sin \alpha)d\alpha - (\tfrac{1}{2}mv_\parallel^2 + \mu B)dt.\end{aligned}\tag{2.34}$$

Finally, we average eq. (2.34) over α and note that

$$(\mathbf{g} \cdot \nabla \mathbf{A}) \cdot \mathbf{h} - (\mathbf{h} \cdot \nabla \mathbf{A}) \cdot \mathbf{g} = B,\tag{2.35}$$

leaving us with the gyrophase-independent guiding centre one-form:

$$\Gamma_0(\mathbf{X}, v_\parallel, \mu, \alpha) = e\mathbf{A}^* \cdot d\mathbf{X} + \frac{m}{e}\mu d\alpha - H_0 dt,\tag{2.36}$$

where $\mathbf{A}^* = \mathbf{A} + (mc/e)v_\parallel \mathbf{b}$ is the generalised vector potential, and $H_0 = \tfrac{1}{2}mv_\parallel^2 + \mu B$ is the lowest order guiding centre Hamiltonian. Putting Γ_0 into the Euler-Lagrange equations recovers the gyromotion, $\dot{\alpha} = \Omega$, and the conservation of the magnetic moment $\dot{\mu} = 0$.

2.3.3 Gyro-centre transformation

In order to perform the transformation from the guiding centre frame to the gyro-centre frame, we use the Lie formalism. This transforms one system of coordinates,

z , into another, \mathcal{Z} , by the following operation:

$$\mathcal{Z}^\mu = T z^\mu. \quad (2.37)$$

where $T = \dots T_3 T_2 T_1$ is a sequence of near-identity transforms. These can be expressed as:

$$T_n = \exp(\epsilon_\delta^n L_n), \quad (2.38)$$

where ϵ is our small parameter and L_n are operators that act on scalars as

$$L_n f = g_n^\mu \frac{\partial f}{\partial z^\mu}, \quad (2.39)$$

and on vectors as

$$(L_n \Gamma)_n = g_n^\nu \left(\frac{\partial \Gamma_\mu}{\partial z^\nu} - \frac{\partial \Gamma_\nu}{\partial z^\mu} \right) = g_n^\nu \hat{\omega}_{\nu\mu}. \quad (2.40)$$

Here, g_n^ν are the generators of the Lie transform at order n . We make the transformation from guiding centre to gyro-centre using T :

$$\bar{\Gamma} = T^{-1} \Gamma + dS, \quad (2.41)$$

where S is an arbitrary gauge function. Because T is a near identity transformation, and ϵ_δ is small, we can expand T^{-1} :

$$T^{-1} = 1 - \epsilon_\delta L_1 + \epsilon_\delta^2 \left(\frac{1}{2} L_1^2 - L_2 \right) + \mathcal{O}(\epsilon_\delta^3). \quad (2.42)$$

Putting this into the transformation of the one-form we get:

$$\begin{aligned} \bar{\Gamma}_0 + \epsilon_\delta \bar{\Gamma}_1 + \epsilon_\delta^2 \bar{\Gamma}_2 + \mathcal{O}(\epsilon_\delta^3) &= \left[1 - \epsilon_\delta L_1 + \epsilon_\delta^2 \left(\frac{1}{2} L_1^2 - L_2 \right) + \mathcal{O}(\epsilon_\delta^3) \right] \cdot \left(\Gamma_0 + \epsilon_\delta \Gamma_1 + \epsilon_\delta^2 \Gamma_2 + \mathcal{O}(\epsilon_\delta^3) \right) \\ &\quad + dS_0 + \epsilon_\delta dS_1 + \epsilon_\delta^2 dS_2 + \mathcal{O}(\epsilon_\delta^3), \end{aligned} \quad (2.43)$$

then collecting terms of the same order, we finally arrive at

$$\bar{\Gamma}_0 = \Gamma_0, \quad (2.44)$$

$$\bar{\Gamma}_1 = \Gamma_1 - L_1 \Gamma_0 + dS_1, \quad (2.45)$$

$$\bar{\Gamma}_2 = \Gamma_2 - L_1 \Gamma_1 + \frac{1}{2} L_1^2 \Gamma_0 - L_2 \Gamma_0 + dS_2, \quad (2.46)$$

where, as we are free to choose S , we have set $dS_0 = 0$. The Lie-transform method allows us the freedom to choose the generators g_n^μ as well as the gauge functions S

such that our new one-form $\bar{\Gamma}$ does not depend on the gyro-angle α . This process requires a great deal of algebra, but it is almost entirely mechanical mathematics. We choose the generators to put the time dependent parts into the Hamiltonian, and then choose the first-order gauge, S_1 , such that the end result is:

$$\bar{\Gamma}_1 = -e\langle\phi\rangle dt, \quad (2.47)$$

where the angle brackets denote the average over the gyro-angle, otherwise known as the gyroaverage. The gyroaverage of a function g is given by

$$\langle g \rangle = \frac{1}{2\pi} \int_0^{2\pi} g d\alpha. \quad (2.48)$$

The Euler-Lagrange equations remain the same as for the guiding centre case - all our changes were to the Hamiltonian. It can be shown that there is no closed energy theorem at first order, therefore we must go to second order, at least for the Poisson equation. Our choices of the Lie derivatives and the gauges have consequences at higher orders. The procedure is the same as for the first order transformation, just inserting the choices we made for S_1 and L_1 into eq. (2.46). The Euler-Lagrange equations again do not change form, but the potential now has extra pieces and is replaced by the renormalised potential:

$$\bar{\phi} = \langle\phi\rangle - \frac{e}{2B} \frac{\partial}{\partial\mu} \langle\tilde{\phi}^2\rangle - \frac{m}{2eB^2} \langle\nabla\tilde{\phi} \cdot (\mathbf{b} \times \nabla\tilde{\phi})\rangle, \quad (2.49)$$

where $\tilde{\phi} = \phi - \langle\phi\rangle$. The second term in eq. (2.49) is the $E \times B$ energy while the second term will be dropped later. The renormalised potential is only used in the calculation of the field equations, whereas the equations of motion only use the first order potential. The full one-form to second order is now

$$\bar{\Gamma} = \mathbf{A}^* \cdot d\mathbf{X} + \frac{mc}{e} \mu d\alpha - H dt, \quad (2.50)$$

with the second order Hamiltonian

$$H = H_0 + H_1 + H_2 = \frac{1}{2} m v_{\parallel}^2 + \mu B + e\bar{\phi}. \quad (2.51)$$

2.3.4 The gyrokinetic equations of motion

The equations of motion can be formed from inserting eq. (2.36) and eq. (2.47) into eq. (2.15).

$$\frac{d\mathbf{X}}{dt} = \frac{\mathbf{b}}{eB_{\parallel}^*} \times \nabla H + \frac{\mathbf{B}^*}{mB_{\parallel}^*} \frac{\partial H}{\partial v_{\parallel}}, \quad (2.52)$$

$$\begin{aligned} \frac{dv_{\parallel}}{dt} &= -\frac{\mathbf{B}}{mB_{\parallel}^*} \cdot \nabla H, \\ &= -\frac{1}{mv_{\parallel}} \frac{d\mathbf{X}}{dt} \cdot H, \end{aligned} \quad (2.53)$$

$$\frac{d\mu}{dt} = 0, \quad (2.54)$$

$$\frac{d\alpha}{dt} = \Omega, \quad (2.55)$$

where $\mathbf{B}^* = \nabla \times \mathbf{A}^*$ and $B_{\parallel}^* = \mathbf{b} \cdot \mathbf{B}^*$. Here we can see that we recover the fast gyromotion of the particles as well as the conservation of the magnetic moment. If we now insert the Hamiltonian to first order, $H = H_0 + H_1 = \frac{1}{2}mv_{\parallel}^2 + \mu B + e\langle\phi\rangle$, into the eqs. (2.52) to (2.55) and simplify

$$\frac{d\mathbf{X}}{dt} = v_{\parallel}\mathbf{b} + \frac{1}{\Omega B_{\parallel}^*}(v_{\parallel}^2 + \frac{1}{2}v_{\perp}^2)(\mathbf{b} \times \nabla B) - \frac{v_{\parallel}^2}{\Omega B_{\parallel}^*}\mathbf{b} \times [\mathbf{b} \times (\nabla \times \mathbf{B})] + \frac{\langle\mathbf{E}\rangle \times \mathbf{B}}{B_{\parallel}^* B} \quad (2.56)$$

$$\begin{aligned} \frac{dv_{\parallel}}{dt} &= \frac{1}{2}v_{\perp}^2 \nabla \cdot \mathbf{b} + \frac{v_{\perp}^2 v_{\parallel}}{2\Omega B_{\parallel}^* B} \left\{ \mathbf{b} \times [\mathbf{b} \times (\nabla \times \mathbf{B})] \right\} \cdot \nabla B \\ &\quad + \langle\mathbf{E}\rangle \cdot \left\{ \frac{q}{m}\mathbf{b} + \frac{v_{\parallel}}{BB_{\parallel}^*} \left[(\mathbf{b} \times \nabla B) - \mathbf{b} \times \{ \mathbf{b} \times (\nabla \times B) \} \right] \right\} \end{aligned} \quad (2.57)$$

2.4 Vlasov equation and the δf formulation

The distribution function, F , of the plasma can be split into two parts,

$$F = F_0 + \delta f, \quad (2.58)$$

with a slowly varying equilibrium part F_0 and a smaller fluctuating part δf . According to our ordering, eq. (2.6), δf must be smaller than F_0 :

$$\frac{\delta f}{F_0} \sim \epsilon_B \ll 1. \quad (2.59)$$

That is, δf is everywhere smaller than F_0 . We employ here another set of orderings, based on the properties of tokamak turbulence. The motion of particles along field lines is on the order of the thermal velocity, smoothing out any parallel structures in the distribution function, while perpendicular structures may be on the order of the Larmor radius. Taking $k_{\parallel} \sim 1/qR$, $\omega \sim k_{\parallel}v_{th}$, we order the perpendicular and parallel structures as

$$\frac{k_{\parallel}}{k_{\perp}} \sim \epsilon_B \ll 1, \quad (2.60)$$

the reason for doing so is discussed in section 3.2. Now, as $k_{\parallel} \sim \nabla_{\parallel} = \mathbf{b} \cdot \nabla$, and $k_{\perp} \sim \nabla_{\perp} = \nabla - \nabla_{\parallel}$, we can order the gradients of the distribution function as

$$\nabla_{\parallel} \delta f \sim \epsilon_B \nabla_{\perp} \delta f. \quad (2.61)$$

Along with eq. (2.59), this means that the gradient length scales of F_0 are smaller than those of δf by ϵ_B only in the perpendicular direction, whereas they are the same order in the parallel dimension.

F_0 can be any function which depends solely on the constants of motion. In practice, F_0 is usually chosen to be a Maxwellian,

$$F_{0i}(\mathcal{E}, \mu, \psi_0) = \frac{n_{0i}(\psi_0)}{(2\pi)^{2/3} v_{thi}^3(\psi_0)} \exp\left(-\frac{\mathcal{E}}{T_i(\psi_0)}\right), \quad (2.62)$$

where $v_{th} = \sqrt{T/m}$ is the thermal velocity, n, T are the equilibrium density and temperature of species i , and $\mathcal{E} = \frac{1}{2}mv^2$ is the kinetic energy.

To evolve the distribution function, we put eq. (2.58) into eq. (2.1)

$$\frac{dF}{dt} = \frac{dF_0}{dt} + \frac{d\delta f}{dt} = 0, \quad (2.63)$$

and assuming that the equilibrium part does not change with time, we find

$$\frac{d\delta f}{dt} = -\frac{dF_0}{dt} = \frac{\partial F_0}{\partial t} - \frac{\partial F_0}{\partial \mathbf{X}} \cdot \frac{d\mathbf{X}}{dt} - \frac{\partial F_0}{\partial v_{\parallel}} \cdot \frac{dv_{\parallel}}{dt} - \frac{\partial F_0}{\partial \mu} \cdot \frac{d\mu}{dt}. \quad (2.64)$$

The first and last terms on the right-hand side are equal to zero. We now need to take derivatives of the Maxwellian:

$$\nabla F_0 = \left[\frac{n'_0}{n_0} - \frac{3T'_i}{2T_i} + \frac{\mathcal{E}T'_i}{T_i^2} \right] F_0 \nabla \psi_0 - F_0 \frac{\mu}{T_i} \nabla B, \quad (2.65)$$

$$\frac{\partial F_0}{\partial v_{\parallel}} = -\frac{mv_{\parallel}}{T_i} F_0, \quad (2.66)$$

where the derivatives are with respect to ψ_0 . Putting eqs. (2.65) and (2.66) into eq. (2.64) and making the simplification

$$\kappa(\psi_0) = \frac{n'_0}{n_0} - \frac{3T'_i}{2T_i} + \frac{\mathcal{E}T'_i}{T_i^2}, \quad (2.67)$$

we finally arrive at the equation for the evolution of δf

$$\frac{d\delta f}{dt} = \tau(\mathbf{E}) = -F_0\kappa(\psi_0)\frac{d\mathbf{X}}{dt} \cdot \nabla\psi_0 + \frac{q_i F_0}{T_i}\langle\mathbf{E}\rangle \cdot \frac{d\mathbf{X}}{dt}\bigg|_0, \quad (2.68)$$

with the last term being evaluated along unperturbed orbits, i.e. that the $\dot{\mathbf{X}}$ term does not include contributions from $\langle\mathbf{E}\rangle$.

2.5 Poisson's equation and quasi-neutrality

In addition to the equations of motion, we also need to solve the field equations for the electrostatic potential. The imposition of quasi-neutrality:

$$\sum_s q_s n_s(\mathbf{x}) = 0, \quad (2.69)$$

summing over all species, means that Poisson's equation cannot be used directly, as there is no charge density. Instead, the quasi-neutrality equation is used. However, this calls for the densities in particle space. It is possible to build a new density in the gyro-centre frame, which includes the effects of gyro-screening of the potential. This comes from the second order contribution to the Lagrangian, the renormalised potential.

In particle space, the density is given by

$$n(\mathbf{x}) = \int F(z)\delta(\mathbf{X} + \boldsymbol{\rho} - \mathbf{x})Jd^6z. \quad (2.70)$$

The near-identity transformations are used to not only transform the coordinate system, but also scalar fields on the phase space, such that

$$F(\mathbf{Z}) = \bar{F}(\bar{\mathbf{Z}}). \quad (2.71)$$

Applying the Lie transform to the distribution function yields, to first order:

$$F(\mathbf{Z}) = T\bar{F}(\bar{\mathbf{Z}}) = 1 + L_1\bar{F}(\bar{\mathbf{Z}}) + \mathcal{O}(\epsilon^2). \quad (2.72)$$

Equation (2.39) tells us how the Lie transform acts on scalars. The same generating functions used in section 2.3.3 are used again here, to give

$$n(\mathbf{x}) = \int \left[\bar{F}(\bar{z}) + \frac{e^2}{m^2 B} \left(\tilde{\phi} \frac{\partial f}{\partial \mu} + \frac{1}{m \Omega} (\nabla \tilde{\phi}) \times \mathbf{b} \cdot \nabla \bar{F} \right) \right] \delta(\mathbf{X} + \boldsymbol{\rho} - \mathbf{x}) \bar{J} d^6 z, \quad (2.73)$$

where the Jacobian,

$$\bar{J} = B_{\parallel}^*, \quad (2.74)$$

can be calculated from the square root of the determinate of eq. (2.16).

The Poisson equation will eventually be linearised, meaning that ∇F will be replaced with ∇F_0 in the last term. This term is already $\mathcal{O}(\epsilon_\delta)$, and the introduction of the temperature and density gradients from ∇F_0 mean that it becomes one order smaller again and so may be neglected. Equation (2.73) can now be rewritten as

$$n_i(\mathbf{x}, t) = \langle n_i(\mathbf{X}, t) \rangle + n_{i,\text{pol}}(\mathbf{x}, t), \quad (2.75)$$

$$\langle n_i(\mathbf{X}, t) \rangle = \int d\mathbf{X} dv_{\parallel} d\mu d\alpha B_{\parallel}^* F \delta(\mathbf{X} + \boldsymbol{\rho}_i - \mathbf{x}), \quad (2.76)$$

$$n_{i,\text{pol}}(\mathbf{x}, t) = \frac{q_i^2}{m_i^2 \Omega_i} \int d\mathbf{X} dv_{\parallel} d\mu d\alpha B_{\parallel}^* [\phi(\mathbf{x}, t) - \langle \phi(\mathbf{X}, \mu, t) \rangle] \frac{\partial f}{\partial \mu} \delta(\mathbf{X} + \boldsymbol{\rho}_i - \mathbf{x}), \quad (2.77)$$

where $n_{i,\text{pol}}$ is the polarisation density. In the absence of other species, quasi-neutrality means setting $n_e = n_i$. A common assumption is one of adiabatic, or Boltzmann, electrons where the electron mass is neglected and they are assumed to respond instantaneously to perturbations in the electrostatic potential. The equation of motion for adiabatic electrons is then

$$\begin{aligned} m_e n_e \frac{dv_{\parallel}}{dt} &= e n_e \nabla_{\parallel} \phi - T_e \nabla_{\parallel} n_e \\ 0 &= e n_e \nabla_{\parallel} \phi - T_e \nabla_{\parallel} n_e \end{aligned} \quad (2.78)$$

$$\Rightarrow \frac{\nabla_{\parallel} n_e}{n_e} = \frac{e \nabla_{\parallel} \phi}{T_e}. \quad (2.79)$$

Equations (2.75) and (2.78) can be solved together to give the evolution of the perturbed density only with some additional assumptions. These are expounded in chapter 4.

2.6 Summary

In this chapter, the gyrokinetic equations have been derived, forming a closed set of equations consisting of the equations of motion, eqs. (2.56) and (2.57), the background distribution function and its evolution, eqs. (2.62) and (2.68), and the gyrokinetic Poisson equation, eqs. (2.69), (2.75) and (2.78). From the perturbed density, the electrostatic field can be found and the gyroaveraged electric field calculated and put into the equations of motion. The actual numerical implementation of this set of equations, and the further assumptions that are made, is detailed in chapter 4.

Chapter 3

Microinstabilities

The fluctuations responsible for the anomalous transport discussed in section 1.3.2 are now known to originate from turbulence driven by plasma instabilities[27]. While single fluid MHD predicts various large scale instabilities, the inclusion of finite Larmor radius and kinetic dissipation effects leads to other forms of instabilities. These typically have a much smaller scale than MHD instabilities, lending them the name of *microinstabilities*. The perpendicular wavelength of microinstabilities is on the order of the gyroradius, while the parallel wavelength is much longer due to the lack of confinement along the field lines. These properties are inherited by the turbulence that they drive, which forms part of the evidence that these drive the fine scale turbulence observed in tokamaks. Although predicting the turbulence saturation levels needs nonlinear effects, linear analysis of these modes can lead to useful identification of their drives and context, such as characteristic length and time scales, or the “stiff profiles” (see section 3.4). Drift waves are collective modes that exist in plasmas and are a consequence of different electron and ion dynamics. They were first experimentally identified in linear machines in the sixties[28] and in tokamaks in the late seventies[29, 30]. In tokamaks, they have a characteristic frequency of $f \sim 5 - 500$ kHz, and perpendicular wavenumbers of $k_{\perp} \sim 1 - 10 \text{cm}^{-1}$. While we can describe the linear modes well, it is not possible to observe them experimentally, as they exhibit exponential growth, with short growth times of 10 kHz or more. As a consequence, we always observe the saturated nonlinear state.

There are two broad categories of microinstabilities - dissipative and reactive[25]. Dissipative modes rely on dissipation to drive the instability, either through Landau damping¹ or collisions. Reactive, or interchange, instabilities do not need dissipation. Both types of modes can tap the free energy of temperature and density

¹A wave-particle interaction, somewhat akin to surfers riding waves[31].

gradients present in fusion devices. This chapter describes the main microinstabilities in tokamaks, and how they lead to turbulence.

3.1 “Universal drive”

One of the simplest drift waves can be derived using a fluid model for the ions and adiabatic electrons[25], which respond instantaneously to perturbations in the ion density to ensure quasineutrality. We use slab geometry, with the magnetic field uniform and homogeneous, pointing in the z direction, $\mathbf{B} = B\mathbf{e}_z$, cold ions, $T_i = 0$, and with a density gradient in the x direction, $\nabla \ln n_0 = -\mathbf{e}_x/L_n$. The ion mass continuity equation is

$$\frac{\partial n_i}{\partial t} + \nabla \cdot (n_i \mathbf{v}) = 0, \quad (3.1)$$

where \mathbf{v} is the fluid velocity of the ions. In this geometry, there are no magnetic drifts. We now linearise this equation, and assume a plane wave solution for the ion density perturbation:

$$n_i = n_0 + \delta n_i(\mathbf{x}, t), \quad (3.2)$$

$$\delta n_i(\mathbf{x}, t) = \tilde{n}_i \exp(i\{k_{\parallel}z + k_{\perp}y - \omega t\}), \quad (3.3)$$

where $\delta n_i \ll n_0$, k_{\parallel}, k_{\perp} are the parallel and perpendicular wavenumbers respectively of the perturbation with complex frequency $\omega = \omega_0 + i\gamma$. The perturbed potential, ϕ , gives rise to an $E \times B$ velocity, which, assuming a plane wave solution again, can be written as

$$\tilde{\mathbf{v}}_{E \times B} = \frac{\mathbf{b} \times \nabla \phi}{B} = \frac{1}{B} \frac{d\phi}{dx} \mathbf{e}_y - \frac{1}{B} \frac{d\phi}{dy} \mathbf{e}_x = \frac{1}{B} \frac{d\phi}{dx} \mathbf{e}_y - \frac{1}{B} k_{\perp} \phi \mathbf{e}_x. \quad (3.4)$$

Putting this equation into eq. (3.1), and using $\nabla \cdot \tilde{\mathbf{v}}_{E \times B}$, we get

$$\frac{\partial \delta n_i}{\partial t} + \tilde{v}_{E \times Bx} \frac{dn_i}{dx} + n_i \frac{\partial \tilde{v}_{\parallel}}{\partial z} = 0, \quad (3.5)$$

$$\omega \delta n_i = \omega_* n_0 \frac{e\phi}{T_e} + k_{\parallel} n_i \tilde{v}_{\parallel}, \quad (3.6)$$

where ω_* is the diamagnetic frequency:

$$\omega_* = -\frac{k_{\perp} T_e}{e B L_n} \quad (3.7)$$

The equation for the parallel electron dynamics is given by eq. (2.79). Assuming $n_e = n_0$ when there is no perturbation, the solution to this equation is

$$n_e = n_0 \exp\left(\frac{e\phi}{T_e}\right). \quad (3.8)$$

The Taylor expansion of this gives us the so-called “Boltzmann response”:

$$\delta n_e = n_0 \frac{e\phi}{T_e}. \quad (3.9)$$

However, this solution leaves us with a purely real frequency - meaning that the wave is only propagating, and does not grow or decay. In order to make the mode unstable, it is necessary to induce some phase difference between some of the perturbed quantities. There are many different ways to bring about this phase difference, and each mechanism leading to its own particular form of drift wave. Merely the addition of dissipation to this model leads to an exponentially growing mode, and this general mechanism was once thought to be so ubiquitous that it was named the “universal instability”. However, in the derivation of this mode some important assumptions were made about the magnetic geometry. Firstly, it ignores magnetic shear, which turns out to have a damping influence. The introduction of toroidal effects, such as the magnetic drifts, complicates matters further, as these moderate the damping from magnetic shear, but bring in their own additional drives.

In this thesis, we focus on only two particular instabilities: the ion temperature gradient mode (ITG) and the trapped electron mode (TEM).

3.2 Toroidal ITG mode

There are several branches of the ITG mode, such as the slab, impurity and toroidal[32]. We focus on the toroidal version, as it is the most relevant in tokamaks, and present here only an outline of the mechanism[33]. For a more in-depth derivation and discussion, see [25, 32].

Figure 3.1 shows a poloidal cross-section of a tokamak with both temperature and density gradients. The red region represents a hot, dense core, with temperature T_1 and density n_1 , while the blue region is cooler and rarefied, with its corresponding temperature and density T_2, n_2 , and with $T_1 > T_2, n_1 > n_2$. As the magnetic drifts go as the kinetic energy, $v_D \sim v^2$, an initial temperature perturbation results in a differential drift across the perturbation. The ions in the cooler (negative) perturbation have a smaller drift than those in the hotter (positive) perturbation,

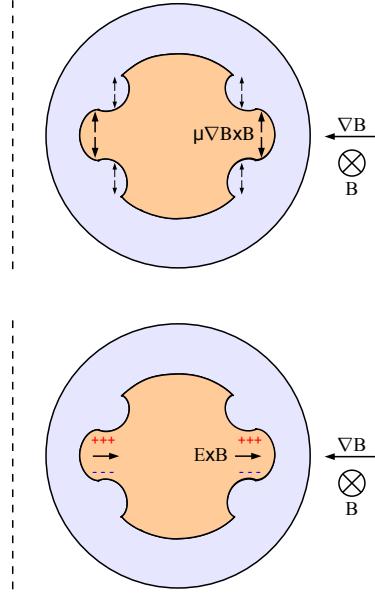


Figure 3.1: Schematic of toroidal ITG mode mechanism. The ∇B drift is dependent on the particle's velocity, so those particles in the hotter, denser inner region have a larger drift than those in the cooler, rarefied outer region. This leads to a build up of charge on the edges of the perturbation, in turn leading to an $E \times B$ drift radially outwards on the outboard side, and inwards on the inboard side. The $E \times B$ drift enhances the perturbation on the outboard side, as it brings hotter plasma into the positive perturbation, and vice versa on the inboard side.

resulting in a build up of ions on edge of the positive perturbation and a deficit on the other side. This density build up/deficit leads to a potential perturbation as the adiabatic electrons stream in to balance the density and preserve quasineutrality. The potential sets up an $E \times B$ drift which drags hot plasma into the positive perturbation and cool plasma into the negative perturbation, enhancing both of them. This feedback loop is what drives the instability, causing it to undergo exponential growth.

This mechanism not only applies on the outboard, low-field side of the tokamak, but also on the inboard side, where ∇B is pointing in the opposite direction to ∇p . All the drifts are in the same directions, but now the $E \times B$ drift drags cool plasma into the *positive* perturbation and hot plasma into the *negative* perturbation, suppressing the instability. For this reason, the inboard side is often called the “good curvature” region, as the curvature drift acts to damp instabilities; correspondingly, the outboard side is known as the “bad curvature” region.

An important effect not discussed so far is that of finite Larmor radius (FLR)

effects. The finite size of the gyroradius means that particles only feel the gyroaveraged electrostatic potential perturbations with length scales smaller than the gyroradius. This leads to a suppression of the instability for modes with $k_\theta \rho_i \gg 1$. Neglecting FLR effects, the growth rate of the ITG mode is proportional to $k_\theta \rho_i$ - the inclusion of FLR is responsible for the turn over in the growth rate spectrum as the mode wavelength approaches the Larmor radius.

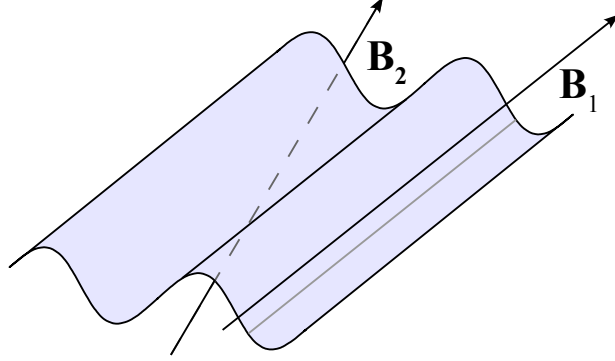


Figure 3.2: Magnetic shear damps modes with parallel variation.

Figure 3.2 illustrates the reason for instabilities in tokamaks to align themselves along the magnetic field[34], that is, align themselves such that $\mathbf{k} \cdot \mathbf{B} = 0$. The blue sheet represents the surface of constant perturbed potential in a sheared magnetic field. The mode has $k_\parallel = 0$ along the field line labelled \mathbf{B}_1 , and this is roughly true for a small radial excursion from this flux surface. However, because the magnetic field is sheared, at some nearby flux surface, the mode must have $k_\parallel \neq 0$ along \mathbf{B}_2 . The rapid parallel dynamics act to quickly damp the perturbation at this flux surface². Hence the tendency for microinstabilities and turbulence to align with the field lines. We can be more precise than this. Given a mode with toroidal and poloidal mode numbers n and m respectively, we can state that we expect to see modes[25] with

$$m = -nq(\psi), \quad (3.10)$$

where $q(\psi)$ is the safety factor on a flux surface ψ , defined in section 1.2.2. Modes that follow eq. (3.10) will find that they have $\mathbf{k} \cdot \mathbf{B} = 0$ across the whole flux surface, on average.

The electron drift wave discussed in section 3.1 does not lead to any radial

²Of course, this is only true for those instabilities susceptible to parallel stabilisation, which is the case for the microinstabilities discussed in this thesis.

flux. This can be seen immediately from the formula for radial particle flux:

$$\Gamma = \overline{\delta n \delta v_{\perp}}, \quad (3.11)$$

where the overline indicates an average over time, and $v_{\perp} = \mathbf{v}_{E \times B} \cdot \mathbf{e}_{\psi}$ is the radial component of the $E \times B$ velocity. Given that the time-average of a single fluctuating quantity is zero (as the mean is zero), and that δn and δv_{\perp} are out of phase by $\pi/2$ (as δn and ϕ are in phase), then eq. (3.11) must also be zero. In fact, the version of the ITG mode presented here also lacks a radial particle flux, but it does lead to a time-average radial heat flux:

$$Q = \overline{\delta T \delta v_{\perp}}. \quad (3.12)$$

3.3 Trapped particle effects

Spherical tokamaks have a larger fraction of trapped particles than conventional tokamaks, and so instabilities driven by trapped particle effects play a bigger role[35]. There are several different possible modes, depending on the ordering of the instability, collisionality and bounce frequencies of the varying species[25]. For MAST, the most relevant trapped particle microinstabilities are those with frequencies between the ion and electron bounce frequencies, existing at low collisionality[35].

When electrons become trapped on the outboard side, they can no longer respond “instantaneously” to deviations in the ion density as their parallel motion is now restricted - averaged over one bounce period, their parallel velocity is zero. Because trapped electrons spend a lot longer in the bad curvature region, magnetic drifts are more important for them than for passing particles. The magnetic drifts for ions and electrons are in different directions, but because passing electrons average the drifts over the whole poloidal domain, they tend to damp this instability. However, for trapped particles, they keep this effect. The different signs of ion and electron magnetic drifts leads to a charge separation in a similar fashion to that described in section 3.2 and so to the entailed $E \times B$ drift, which enhances any initial perturbation.

3.4 Turbulence

The linear instabilities discussed in this chapter can only grow so much before they saturate. The amplitude at which they do saturate requires including the full non-

linear physics to determine³. The exact physical process of nonlinear saturation is currently an open question, with several players already known[27]. Coupling between different scales via the convective derivative in the fluid conservation equations leads to energy being transferred from the linear microinstabilities that exist at a given scale to other modes, which may even be linearly stable[36]. These modes can then go on to generate further modes at different scales again, leading to a “cascade” of energy into broad range of scales, including down to the smallest scales where the fluctuations dissipate and turn into heat. This eventually leads to saturation when the nonlinear transfer of energy to the damping scales balances the release of free energy from the driving gradients. Broad fluctuation spectra are one of the characteristic features of turbulence, and this has been observed in linear machines, where it is possible to drive and observe single, coherent drift waves. For example, using parallel-current driven instabilities, researchers using linear devices[37] were able to observe the change from a narrow band of fluctuation frequencies to a broad spectrum by increasing the drive for the mode. This forms part of the experimental evidence for drift wave turbulence in tokamaks. For a more complete review, see [25, 27]. It is also possible for secondary instabilities to develop, generated by the locally increased gradients formed by the movement of plasma parcels around a drift wave[32].

Turbulence often has a threshold gradient value, which, when exceeded, leads to a drastic increase in the transport of equilibrium quantities. This increased transport then acts to reduce the gradients back down to the critical value. For this reason, profiles in tokamaks are often described as “stiff” - they become insensitive to the heating. Any increase in the heating only leads to a correspondingly increased transport. Equilibrium profiles, then, should be marginally stable - that is, they exist near the critical gradient.

Equations (3.11) and (3.12) lead to two different diffusivities. The Bohm diffusivity[25] is given by

$$D_B = \frac{cT_e}{eB}, \quad (3.13)$$

and the gyro-Bohm diffusivity is

$$D_{GB} = \rho_* D_B. \quad (3.14)$$

The Bohm diffusivity is independent of the system size, and arises due to mesoscale

³The difference between linear and nonlinear simulations generally means whether or not the particles are influenced by the perturbed electrostatic field, with nonlinear simulations including the $\delta\phi$ term in the v_{\parallel} and $\dot{\mathbf{X}}$ equations.

structures, whereas the gyro-Bohm diffusivity scales with the system size and is due to turbulence at the gyroradius scale. There are a variety of mechanisms predicted from theory, or seen in simulations and experiments that can explain the reason for these two different diffusivities. In certain conditions, turbulence can lead to non-diffusive, non-local transport. Avalanches are intermittent events with two fronts - a positive fluctuation of heat or particles propagates down the corresponding gradient, while a negative perturbation propagates up the gradient. Streamers are radially elongated structures, larger than the transport scale length of the driving microinstability. Both these processes can lead to increased cross-field transport as their sizes scale with the system size, but they can also both be regulated by sheared flows (see sections 3.4.1 and 3.5). Turbulence can also spread into linearly stable regions via nonlinear processes, leading to increased transport in those regions.

3.4.1 Zonal Flows

One of the most important physical processes for determining the saturation level is zonal flows[36, 38], which are axisymmetric structures, with $m, n = 0$, and are well-localised radially (i.e. they have large k_r). They arise from the divergence of the Reynolds stress[36], $\nabla \langle \delta v_x \delta v_y \rangle$, where $\delta v_{x,y}$ are fluctuating velocities in different directions, and $\langle \rangle$ is a time-average. The Reynolds stress merely rearranges momentum, and does not act as a source or sink[34]. Alternatively, one can think of the generation of zonal flows as being due to a nonlinear transfer of energy in the Fourier domain, with large k structures driving energy in small k (specifically $k = 0$).

Their symmetric structure has two important consequences. The first is that they are not subject to Landau damping[38]. Secondly, due to their flows being perpendicular to the temperature and density gradients, they cannot access the free energy locked up in the gradients[36]. Their structure also means that they can suppress turbulence due to their shear flows (see section 3.5).

Zonal flows are linearly stable, therefore they have to be driven solely by nonlinear turbulent processes[27]. The effect of this is that they are a form of self-regulation for the turbulence, as they both regulate the level of turbulent transport and die away without the background turbulence. At low collisionality, therefore, they can be a significant yet harmless store of free energy.

3.4.2 Turbulence diagnostics

The diagnosis of turbulence in tokamak plasmas is a complicated and tricky practice, but there are several different techniques available to experimentalists (a review of the techniques discussed here, as well as several others may be found in [27]). One of the earliest methods, Langmuir probes, used on the first plasma devices is still in everyday use on state-of-the-art machines. These measure δn , $\delta\phi$, and δT_e , and the correlations between the fluctuating quantities by physically probing the plasma with a biased electrode. The particle, heat and momentum fluxes can all be deduced from these measurements. However, as Langmuir probes require a physical intrusion into the plasma, they are only suitable for use in low-temperature, low-density regions of the tokamak (i.e. outside the separatrix), lest they be vapourised. Short-wavelength lasers may be used to measure δn , as the light will be scattered via Thomson scattering due to the change in refractive index caused by the density perturbations. By measuring at different scattered angles, the wavenumber spectrum may be obtained, as the scattered angle is determined by the wavelength of the fluctuations. Microwaves can also be used, in a technique called reflectometry, whereby microwave radiation is bounced off the cutoff layer in the plasma. This gives the radial location of a particular density. There are various different subclasses of reflectometry, that can be used to get a wide variety of information - from ω, k spectra of the fluctuating density to $2D$ imaging of the turbulence and poloidal velocity measurements.

The above diagnostics are all active methods - passive methods are also possible. For example, beam emission spectroscopy (BES) measures the light emitted from collisional processes due to the injection of neutral heating beams[39]. This will be expanded upon in section 6.5, where we discuss how to directly compare simulation and experiment.

3.5 Sheared flow stabilisation

It is well known that sheared flows can suppress turbulence and stabilise the linear microinstabilities that drive it[40, 41, 42, 43, 44, 45, 46, 47, 48, 49, 50, 51, 52]. The basic picture of stabilisation of linear instabilities by flow shear is as follows: the flow acts on opposite ends of the mode structure differentially. This tilts the mode, which reduces its radial wavenumber, which in turn reduces its growth rate. In ballooning theory, sheared flows stabilise small amplitude modes by advecting the mode structure in the ballooning angle, θ_0 [48], rotating from the outboard, “bad curvature” side to the inboard, “good curvature” side. Because a rotating mode

samples the good curvature region, the growth rate of a bad curvature driven mode is necessarily smaller than one whose θ_0 stays fixed in the bad curvature region on the outboard side. Alternatively, this process can be viewed as coupling modes with $\theta_0 = 0$ to those with $\theta_0 = \pi$. Ballooning theory predicts that the toroidal ITG mode is stabilised when $|\theta_0| \sim \pi/2$ [46].

The nonlinear picture is similar, with sheared flows tilting the eddies, which reduces their radial correlation lengths[47, 51]. The correlation length is roughly the distance between two turbulent eddies of comparable sizes[25]. A fluid parcel moved by one correlation length finds itself no longer in its original context - it is no longer the same eddy. Without flow, the time taken for this to happen is the turbulent correlation time, τ_{corr} , or, equivalently, the eddy turnover time[34]. Flow with a shearing rate⁴ greater than τ_{corr}^{-1} stretch the turbulent eddies to the correlation length in less than one correlation time, essentially reducing their lifetimes. Shorter lifetimes are also accompanied by a reduction in turbulent intensity. Clearly, shorter lifetimes and reduced correlation lengths have the consequence that fluid parcels don't move as far perpendicular to the flow direction during one correlation time, leading to a decrease in the transport of particles and heat. This can be seen simply by using a random-walk argument. A more complete review of flow shear stabilisation can be found in [34].

There are actually three other conditions required for flow shear to be able to suppress turbulence[34]. The sheared flow needs to be stable, the turbulence must stay within the flow for longer than τ_{corr} and the dynamics should be limited to two dimensions. These are all features typical of tokamak plasma turbulence, but not necessarily of other fluids. Shear flows can drive instabilities in non-ionised fluids, for example⁵.

Magnetic shear is also deeply intertwined with $E \times B$ shear[46, 49]. The existence of rational surfaces⁶ in tokamaks tends to localise turbulent fluctuations close to those surfaces, unless there is significant coupling between flux surfaces. Magnetic shear and flow shear then can have a synergistic effect on both linear microinstabilities and turbulent fluctuations. Magnetic shear can also change the stability of sheared flows by, for example, increasing the threshold for the Kelvin-Helmholtz instability, which is a flow shear-driven instability.

The $E \times B$ drift has a central role in many theoretical frameworks of plasma

⁴The shearing rate is the gradient of the flow velocity and has units of inverse time.

⁵Gradients in the parallel velocity in tokamaks can also drive instabilities, but this effect is typically far outweighed by the suppression caused by perpendicular flow shear.

⁶These are flux surfaces where q is a rational number. That is, the number of complete toroidal revolutions the magnetic field makes per poloidal revolution is a rational number.

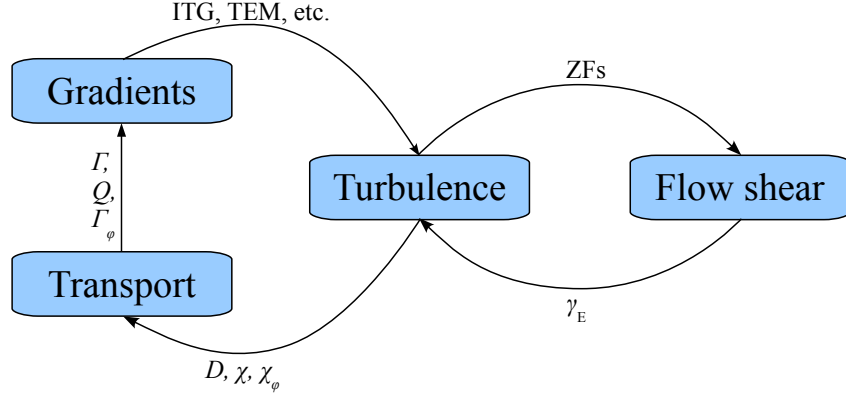


Figure 3.3: Schematic of the interaction of turbulence, sheared flows and equilibrium quantities. The free energy in the density and temperature gradients drives linear microinstabilities which go on to nonlinearly interact and develop into turbulence. Turbulent fluctuations drive increased transport which affects the profile gradients. At the same time, Reynolds stresses from the fluctuating velocities can generate sheared flows (such as zonal flows) which can suppress turbulence and the microinstabilities that drive it. These complex interactions form a synergistic self-regulation process whereby the plasma can self-organise into a more quiescent state.

physics as it affects all species equally - independent of mass or charge. Flow shear also has a kind of universality, reducing turbulent fluctuations and transport in almost all classes of magnetic confinement devices and plasma regimes, even though the driving microinstabilities change from case to case[49]. The combination of these facts has led to sheared $E \times B$ flows being an area of intense study.

The reduction in transport due to flow shear suppression of turbulence can lead to steepening of gradients[53]. Often, this is confined to a small radial region of the tokamak, this region being referred to as a transport barrier. The first transport barriers were observed at the edge[27]. Later, experiments found the existence of internal transport barriers (ITBs). The transport in transport barriers can be reduced as far as neoclassical levels.

The H-mode (“high confinement” mode, in contrast to the “low confinement” L-mode) was discovered on ASDEX in 1982[54]. This is a regime with steep density gradients near the edge which spontaneously develops (given certain conditions). At the same time, density fluctuations die down and a radial electric field, E_r , develops at the edge. The spatial structure of the E_r leads to strong sheared $E \times B$ flows[49]. The H-mode has since been found on every machine with external heating and a divertor[34]. H-mode plasmas are of great interest to the fusion programme, as they often have a doubling or more of the confinement time, as well as an increased

central density[35]. This combination leads to a greater fusion power in the core of the tokamak. However, the exact physical processes that underlie the L-H transition are still a matter of active research. There are a number of universal features of H-modes, with one of the central ones being $E \times B$ flow shear.

There are a whole host of different mechanisms to generate sheared flows, for example by turbulent Reynolds stresses, momentum input from neutral beams, or symmetry breaking (so-called “intrinsic” rotation). MAST achieves high rotation rates from a combination of neutral beam injection (NBI) and its low moment of inertia.

3.6 Summary

In this chapter, we have discussed the origins of turbulence in tokamak plasmas and the main drives for the most common microinstabilities. The free energy in the equilibrium profile gradients can be tapped by various microinstabilities, which can nonlinearly interact, developing into chaotic turbulence. Strong turbulence in tokamaks is responsible for the anomalous transport, with levels well above that predicted by neoclassical theory. The turbulence may drive linearly stable zonal flows which act as a self-regulation mechanism, damping the turbulence through sheared flows and acting as a benign store of free energy.

Chapter 4

The global gyrokinetic PIC code NEMORB

NEMORB is a numerical code, employing the particle-in-cell method, to solve the gyrokinetic equation on the full global domain in tokamaks. It has been used to investigate various microinstabilities in several tokamaks, such as ASDEX, TCV and MAST. NEMORB is capable of not only calculating the growth rates of the linear microinstabilities, but also the full nonlinear steady-state of turbulence in these devices. In this chapter, the numerical methods behind NEMORB are delineated. Details of NEMORB (previously ORB5) can be found in [14, 55, 56, 57]. NEMORB is written in Fortran 95 and is parallelised using MPI.

4.1 Particle-in-cell method

There are almost as many approaches to simulating plasmas as there are codes that do so. Most of the methods have been developed from the computational fluid dynamics community. Broadly, there are two main approaches: Eulerian and Lagrangian[35]. In a Eulerian scheme, the fluid is described in terms of flowing past fixed points in space, whereas Lagrangian methods describe the system from the point of view of the fluid. Both schemes have their own advantages and disadvantages, and both are routinely used in gyrokinetic codes. Eulerian codes can suffer from numerical diffusion due to their finite velocity grids, and may be tricky to implement in general tokamak geometries. Lagrangian codes, on the other hand, are much easier to implement in any geometry and are simple to parallelise. However, given N interacting particles, it is necessary to perform N^2 calculations at each time step. In addition, flow shear can distort the mesh, adding severe complications to

calculating derivatives.

The Particle-in-Cell (PIC) concept builds upon the Lagrangian approach to solve its difficulties[58]. To do so, the distribution function is discretised in phase space into “markers” or “super-particles”. The markers have a volume in phase-space and an associated weight, which represents the number of real particles within that region of phase-space. Either the weight or the volume is evolved in time, with the other kept constant. The markers are then pushed in phase-space according to the equations of motion and are free to move anywhere in phase-space (subject to the applicable boundary conditions). The calculation of the electromagnetic fields is done on a 3D grid (the “cell” part of PIC) in real- or Fourier-space. In order to do this step, the marker weights are interpolated onto the grid before being used in the Poisson/quasi-neutrality equation, which requires only N calculations per time step. The grid is fixed in space, and does not evolve in time, so cannot be distorted by flow shear.

The cost of the PIC scheme is the numerical noise introduced by discretising the distribution function[55]. The ratio of signal to noise goes as $N^{-1/2}$, and vanishes in the limit $N \rightarrow \infty$. Unless steps are taken to control the noise, it grows with time.

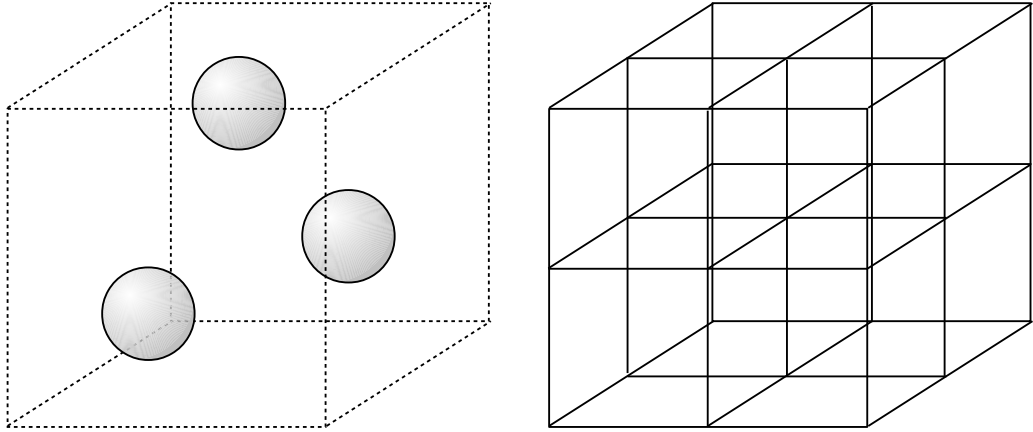


Figure 4.1: In a particle-in-cell (PIC) scheme, the distribution function is discretised in phase space (left), while the electromagnetic fields are discretised on a 3D grid (right).

4.2 Straight-field line coordinates

Clearly, the Cartesian co-ordinate system is not the best frame to formulate the equations of motion for a tokamak, and while cylindrical co-ordinates are a step better, there is a more natural frame to consider. Given the nature of turbulence

in a tokamak, which tends to align itself along the field lines, we would like to have a coordinate system which exploits this. There are an array of different coordinate systems used in tokamak theory, from field-aligned to Hamada to Boozer, all of which have their particular strengths and weaknesses. For example, field-aligned coordinates lend themselves especially well to solving the Poisson equation, but are hard to implement outside of local codes, which exist on a single flux surface. Another type of coordinates involve straightening the field lines. Unrolling a flux surface, the magnetic field lines are revealed to have periodic, oscillating character (see section 4.1). By deforming the poloidal and/or the toroidal angle, the field lines can be stretched or squashed so that they become straight lines. In NEMORB, the poloidal angle is transformed from the geometric angle, θ to the straight-field line angle, θ_* :

$$\theta_* = \frac{1}{q(s)} \int_0^\theta \frac{\mathbf{B} \cdot \nabla \varphi}{\mathbf{B} \cdot \nabla \theta'} d\theta', \quad (4.1)$$

where s is a radial coordinate defined by

$$s = \sqrt{\frac{\psi}{\psi_e}}, \quad (4.2)$$

where ψ_e is the value of the poloidal flux at the edge. Other codes may deform the toroidal angle, transform to field-aligned coordinates or set the Jacobian equal to unity. The coordinate system used throughout NEMORB is (s, θ_*, φ) .

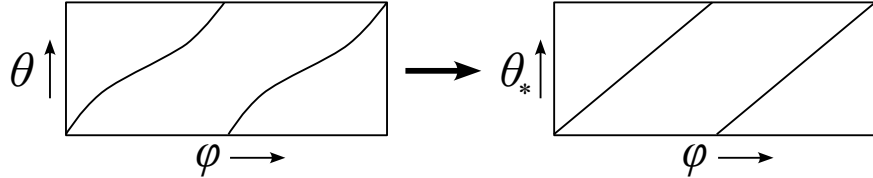


Figure 4.2: Field lines on a flux surface are normally bent. To take advantage of the nature of tokamak turbulence, which is elongated along the field lines, NEMORB deforms the poloidal angle ($\theta \rightarrow \theta_*$) in order to straighten the field lines.

It is worth pointing out here the difference between the various radial coordinates used in this thesis. The minor (r) and major (R) radii are used when it is important to make a connection to the physical size of the device or plasma, or for ease of comparison between numerical codes which may define ψ differently (such as the inclusion of a factor of 2π). The radial coordinate defined above, s , is useful for the numerics, as an array evenly spaced in s will have more points in the outer half of the plasma, where the microinstabilities tend to be stronger (i.e.

where there is interesting physics). The inner core of the plasma is often stable to microinstabilities, and so it is less useful to focus limited computing resources there.

4.3 Parallelisation scheme

PIC methods are inherently parallelisable, as the markers can be moved completely independently and the 3D grid may be split up across processors. Numerical codes which use PIC schemes are a natural fit for high performance computing. ORB5, the predecessor of NEMORB, has been found to show good scaling up to 4096 cores, and NEMORB is regularly used on 8192 cores. NEMORB uses the Message Passing Interface (MPI) to parallelise the equations and employs a 2D parallelisation, with the 3D torus being split up along φ and also being “cloned”. P processors are then split up as

$$P = CP_\varphi, \quad (4.3)$$

where C is the number of clones and P_φ is the number of processors in the φ direction. Each clone contains a copy of the whole torus, while each processor has a toroidal wedge. Decomposing the domain in the poloidal plane is impractical, as the geometry varies both with s and θ_* . This decomposition exploits the axisymmetry of the tokamak, while ensuring that the toroidal slice held by each processor does not become inordinately thin. The number of clones must be tuned by hand. Too few, and the communication starts to bog down the simulation, while too many drastically increases the memory required and may also lead to excessive communication between processors. This is due to the communication between clones becoming dominant, as the particles have to be summed on the grids across all the clones each time-step.

4.4 Numerical discretisation of equations

4.4.1 Equilibrium

The equilibrium can be either a numerical MHD equilibrium from CHEASE, or it can be an analytic *ad-hoc* equilibrium. *Ad-hoc* equilibria are not solutions of the Grad-Shafranov equation. They have circular, concentric cross-sections, but there should be a finite Shafranov shift due to the pressure gradient. CHEASE (Cubic Hermite Element Axisymmetric Static Equilibrium) is a numerical equilibrium solver for the Grad-Shafranov equation for toroidal MHD equilibria. It uses Hermite bicubic finite element discretisation, and takes pressure and current profiles, along with plasma

boundaries, either from analytic expressions or from real experimental data. Details of the code can be found in [59].

Equilibrium quantities are mapped onto a (s, θ_*) grid and are interpolated using splines. Flux function quantities are one-dimensional functions of s .

The background part of the distribution function is a Maxwellian, described in eq. (2.62).

Normalisations

Length and magnetic field strength are expressed in NEMORB in units of $d_{norm} = \rho_*$, and $B_{norm} = B_{axis}$, respectively. All relevant equilibrium quantities can be normalised to combinations of these two normalisations.

4.4.2 Equations of motion in straight field line coordinates

The equation of motion in the direction of a general coordinate A can be found from

$$\frac{dA}{dt} = \frac{d\mathbf{X}}{dt} \cdot \nabla A. \quad (4.4)$$

The magnetic field in a toroidal equilibrium can be written as

$$\mathbf{B} = f(\psi)\nabla\varphi + \nabla\psi \times \nabla\varphi, \quad (4.5)$$

where $f(\psi)$ is the poloidal current flux function. Using eqs. (2.56), (4.4) and (4.5), the equations of motion in NEMORB coordinates can be derived:

$$\frac{ds}{dt} = \frac{m(v_{\parallel}^2 + \frac{1}{2}v_{\perp}^2)}{qB^2B_{\parallel}^*J_{s\theta_*\varphi}}f(\psi)\frac{\partial B}{\partial\theta_*} + \langle E_{\varphi} \rangle \frac{\nabla\psi \cdot \nabla s}{R^2BB_{\parallel}^*} - \langle E_{\theta_*} \rangle \frac{f(\psi)}{BB_{\parallel}^*J_{s\theta_*\varphi}} \quad (4.6)$$

$$\begin{aligned} \frac{d\theta_*}{dt} = & \frac{v_{\parallel}}{BJ_{\psi\theta_*\varphi}} - \frac{m(v_{\parallel}^2 + \frac{1}{2}v_{\perp}^2)}{qB^2B_{\parallel}^*J_{s\theta_*\varphi}}f(\psi)\frac{\partial B}{\partial s} - \frac{mv_{\parallel}^2p'(\psi)f(\psi)}{qB^3B_{\parallel}^*J_{\psi\theta_*\varphi}} \\ & + \langle E_{\varphi} \rangle \frac{\nabla\psi \cdot \nabla\theta_*}{R^2BB_{\parallel}^*} + \langle E_s \rangle \frac{f(\psi)}{BB_{\parallel}^*J_{s\theta_*\varphi}} \end{aligned} \quad (4.7)$$

$$\begin{aligned} \frac{d\varphi}{dt} = & \frac{v_{\parallel}f(\psi)}{BR^2} + \frac{m(v_{\parallel}^2 + \frac{1}{2}v_{\perp}^2)}{qB^2B_{\parallel}^*R^2} \left[\frac{\partial B}{\partial s}(\nabla\psi \cdot \nabla s) + \frac{\partial B}{\partial\theta_*}(\nabla\psi \cdot \nabla\theta_*) \right] \\ & + \frac{mv_{\parallel}^2p'(\psi)|\nabla\psi|^2}{qB^3B_{\parallel}^*R^2} - \langle E_s \rangle \frac{\nabla\psi \cdot \nabla s}{BB_{\parallel}^*R^2} - \langle E_{\theta_*} \rangle \frac{\nabla\psi \cdot \nabla\theta_*}{BB_{\parallel}^*R^2} \end{aligned} \quad (4.8)$$

$$\begin{aligned}
\frac{dv_{\parallel}}{dt} = & -\frac{v_{\perp}^2}{2B^2 J_{s\theta_*\varphi}} \frac{\partial B}{\partial \theta_*} + \frac{mv_{\parallel}v_{\perp}^2}{2qB_{\parallel}^*} \frac{p'(\psi)f(\psi)}{B^4 J_{\psi\theta_*\varphi}} \frac{\partial B}{\partial \theta_*} + \langle E_s \rangle \frac{v_{\parallel}f(\psi)}{B^2 B_{\parallel}^* J_{s\theta_*\varphi}} \frac{\partial B}{\partial \theta_*} \\
& + \langle E_{\theta_*} \rangle \left\{ \frac{q}{mB J_{\psi\theta_*\varphi}} - \frac{v_{\parallel}f(\psi)}{B^2 B_{\parallel}^* J_{s\theta_*\varphi}} \frac{\partial B}{\partial s} - \frac{v_{\parallel}p'(\psi)f(\psi)}{B^3 B_{\parallel}^* J_{\psi\theta_*\varphi}} \right\} \\
& + \langle E_{\varphi} \rangle \left\{ \frac{qf(\psi)}{mBR^2} + \frac{v_{\parallel}}{B^2 B_{\parallel}^* R^2} \left[\frac{\partial B}{\partial s} (\nabla s \cdot \nabla \psi) + \frac{\partial B}{\partial \theta_*} (\nabla \psi \cdot \nabla \theta_*) \right] \right. \\
& \left. + \frac{v_{\parallel}p'(\psi)|\nabla \psi|^2}{B^3 B_{\parallel}^* R^2} \right\}
\end{aligned} \tag{4.9}$$

Boundary conditions

Particles that end a time step with $s > 1$ are put back into the plasma via a simple reflection in their poloidal angle: $\theta_* \rightarrow -\theta_*$. This does not violate conservation of unperturbed invariants in up-down symmetric plasmas, but may do so in up-down asymmetric equilibria. In this thesis, all studies have involved up-down symmetric equilibria.

4.4.3 Vlasov equation

Discretisation of markers

The perturbed distribution function is split up into N markers:

$$\delta f = \frac{N_p}{N} \sum_{i=1}^N \frac{1}{2\pi B_{\parallel}^*} w_i(t) \delta(\mathbf{X} - \mathbf{X}_i(t)) \delta(v_{\parallel} - v_{\parallel,i}(t)) \delta(\mu - \mu_i(t_0)), \tag{4.10}$$

where N_p is the number of physical particles, and $w_i(t)$ is the weight of the i th marker with position $\mathbf{X}_i(t)$, $v_{\parallel,i}(t)$, $\mu_i(t_0)$ in phase space at time t . The distribution function is actually continuous over phase space, but this discretisation uses delta functions. Replacing the delta functions with B-splines is currently under development.

The perturbed distribution function is assumed to be constant over a small volume, Ω_i . Integrating over this volume, and using eq. (2.68), we find that

$$\delta f_i \Omega_i = \frac{N_p}{N} w_i(t) \tag{4.11}$$

$$\Rightarrow \frac{dw_i(t)}{dt} = \frac{N}{N_p} \tau_i \Omega_i, \tag{4.12}$$

where τ_i contains the evolution of δf for species i . The volume of a marker in phase space is

$$\Omega_i = B_{\parallel}^* \frac{d\mathbf{X} dv_{\parallel} dv_{\perp}}{dN}, \tag{4.13}$$

where

$$dN = \frac{N}{N_p} f_L(\mathbf{X}, v_{\parallel}, v_{\perp}) J(s, \theta_*, \varphi) ds d\theta_* dv_{\parallel} dv_{\perp} d\alpha \quad (4.14)$$

f_L specifies the marker loading:

$$f_L(\mathbf{X}) = f_L(s) = K \left[1 - f_g + f_g \exp\left(\frac{s - s_0}{\Delta s}\right) \right] \equiv K p(s), \quad (4.15)$$

where s_0 and Δs are input parameters, f_g is a constant parameter $\in [0 : 1]$, and K is the normalisation constant defined by

$$K = \frac{1}{\int p(s) J_{s\theta_*\varphi}(s, \theta_*) ds d\theta_* d\varphi}, \quad (4.16)$$

i.e. the integral of $p(s)$ over the volume of the whole torus. This loading loads more markers close to s_0 , which is the peak temperature gradient, i.e. the location of the strongest drive for the ITG. Velocities are loaded uniformly in velocity space, up to a cut-off κ_v , which is an input parameter, but is usually set $\kappa_v = 5v_t$, with v_t the thermal velocity.

Marker initialisation

In addition to loading the markers in phase space, their weights also need to be initialised. There are numerous ways of doing so, for example, one of the simplest methods is a white noise initialisation, where the weights are determined by a pseudo-random number generator. However, this can result in the simulation taking a long time to develop a physical mode. More sophisticated initialisations start the weights in configuration close to that of a physical mode. NEMORB has a few of these, with the most commonly used one being the so-called mode initialisation:

$$\begin{aligned} \delta f(t_0) = & \frac{A_0 F_0(\mathbf{X}(t_0) v_{\parallel}(t_0), \mu(t_0))}{(m_2 - m_1 + 1)(n_2 - n_1 + 1)} \left| \frac{T(s_0)}{\nabla T(s_0)} \right| \left| \frac{\nabla T(s(t_0))}{T(s(t_0))} \right| \\ & \times \sum_{m=m_1}^{m_2} \sum_{n=n_1}^{n_2} \cos(m\theta_*(t_0) - n\varphi(t_0)), \end{aligned} \quad (4.17)$$

which loads more markers closer to the peak of the temperature gradient in a sinusoidal configuration, according to the modes in the system, with the result that the initial perturbation is already close to the expected structure of the physical modes. This means that the initial phase of the simulation, before the physical modes start growing, is independent of the number of markers.

Pushing of markers

The equations are evolved with time by integrating with a fourth order Runge-Kutta scheme. The equation of motion for θ_* , eq. (4.7), has a singularity near the magnetic axis, as $\frac{\partial\theta_*}{\partial t} \sim \frac{1}{s}$. In order to avoid this, a new coordinate system is used for $s < s_{push}$, where s_{push} is an input parameter. The following coordinates are used:

$$\xi = s \cos \theta_*, \quad (4.18)$$

$$\eta = s \sin \theta_*, \quad (4.19)$$

which yield following equations of motion:

$$\frac{\partial \xi}{\partial t} = \frac{\partial s}{\partial t} \cos \theta_* - \frac{\partial \theta_*}{\partial t} s \sin \theta_*, \quad (4.20)$$

$$\frac{\partial \eta}{\partial t} = \frac{\partial s}{\partial t} \sin \theta_* + \frac{\partial \theta_*}{\partial t} s \cos \theta_*, \quad (4.21)$$

with the result that these equations now have terms proportional to $s d\theta_*/dt$, which will not diverge at the magnetic axis.

4.4.4 Poisson equation

The Poisson equation is solved on a 3D grid using a finite elements method. The perturbed potential is discretised on a (s, θ_*, φ) grid as

$$\phi(\mathbf{x}, t) = \sum_{\mu} \phi_{\mu}(t) \Lambda_{\mu}(\mathbf{x}), \quad (4.22)$$

where $\phi_{\mu}(t)$ are real numbers, and $\Lambda_{\mu}(\mathbf{x})$ are B-splines¹. The Λ_{μ} are really tensor products of 1D B-splines: $\Lambda_{\mu}(\mathbf{x}) = \Lambda_j(s) \Lambda_k(\theta_*) \Lambda_l(\varphi)$. The Galerkin method can be used to turn eq. (4.22) into a linear system which can then be solved with standard numerical libraries. The linear system is

$$\sum_{\mu} A_{\mu\nu} \phi_{\mu}(t) = b_{\nu}(t), \quad (4.23)$$

¹Splines are smooth polynomials constructed piecewise and are used for interpolating other functions. In general, they are the computationally cheapest, fastest method of doing so. Linear combinations of B-splines (also known as basis splines) can be used to represent any other spline function.

where

$$A_{\mu\nu} = \int \frac{n_0(\psi)}{Z_i T_e(\psi)} \left[\Lambda_\mu(\mathbf{x}) \Lambda_\nu(\mathbf{x}) - \bar{\Lambda}_\mu(s) \bar{\Lambda}_\nu(s) \right] d\mathbf{x} + \frac{n_0(\psi)}{B \Omega_i} \nabla_\perp \Lambda_\mu(\mathbf{x}) \cdot \nabla_\perp \Lambda_\nu(\mathbf{x}), \quad (4.24)$$

$$b_\nu(t) = \frac{N_p}{N} \sum_{j=1}^N \frac{w_j(t)}{2\pi} \int_0^{2\pi} \Lambda_\nu(\mathbf{X}_j + \boldsymbol{\rho}_{i,j}(\alpha)) d\alpha. \quad (4.25)$$

Importantly, $A_{\mu\nu}$ is a real, symmetric matrix, allowing the use of relatively cheap numerical methods in its solution. It is also time-independent, requiring calculation only once. The construction of b_ν by the projection of the markers onto the 3D grid is called charge assignment. This is the largest source of noise in PIC simulations. The perpendicular gradients in eq. (4.24) are assumed to lie in the poloidal plane, giving

$$\nabla_\perp \simeq \nabla_{\text{pol}} = \nabla_s \frac{\partial}{\partial s} + \nabla_{\theta_*} \frac{\partial}{\partial \theta_*}. \quad (4.26)$$

The only dependence on φ of these forms of the equations is in the perturbed density. Therefore, a discrete Fourier decomposition can be used on ϕ_μ and b_ν , yielding

$$\sum_\mu A_{\mu\nu} \hat{\phi}_\mu^{(n)} = \frac{\hat{b}_\nu^{(n)}}{M^{(n),j}}, \quad (4.27)$$

where $\hat{\phi}_\mu^{(n)}$ and $\hat{b}_\nu^{(n)}$ are the Fourier coefficients and $M^{(n),j}$ is defined by

$$M^{(n),j} = \sum_{l'=1} N_\varphi \int \Lambda_{l'}^j(\varphi) \Lambda_l^j(\varphi) \exp\left(\frac{2\pi i}{N_\varphi} n(l' - l)\right) d\varphi. \quad (4.28)$$

In addition, the Dirichlet boundary condition $\phi(s = 1, \theta_*, \varphi, t)$ is applied at the edge and the regularity condition at the axis $\phi(s = 0, \theta_*, \varphi) = \phi(s = 0, \theta_* = 0, \varphi)$. This system of equations is solved using the direct solver, LAPACK (or its parallel version, ScaLAPACK).

Filter

For the linear simulations, we select a single toroidal mode in each simulation, and use a surface-dependent filter (the “diagonal” filter[55]) which suppresses high k_\parallel modes and keeps only poloidal modes with $m = [-nq(s) \pm \Delta m]$, where $\Delta m = 5$. This is done by applying a Fourier filter to the density. First, a 2D Fourier transformation

is done

$$\rho(\mathbf{x}, t) = \sum_{m,n} \hat{\rho}_{m,n}(s, t) e^{im\theta_*} e^{in\varphi} \quad (4.29)$$

and then filtered:

$$\mathcal{F}\rho(\mathbf{x}, t) = \sum_{m,n} \hat{\mathcal{F}}_{m,n} \hat{\rho}_{m,n}(s, t) e^{im\theta_*} e^{in\varphi}, \quad (4.30)$$

where the filter function is

$$\hat{\mathcal{F}}_{m,n}(s) = \mathcal{H}(m - (-nq(s) - \Delta m)) \mathcal{H}((-nq(s) + \Delta m) - m) \mathcal{H}(n - n_{\min}) \mathcal{H}(n_{\max} - n), \quad (4.31)$$

where \mathcal{H} is the Heavyside function, and $\Delta m, n_{\min}, n_{\max}$ are all input parameters. It can be shown that the noise scales with the square root of the number of Fourier modes in the system. This “diagonal” filter reduces the number of modes, and so reduces the noise.

Gyro-averaging

NEMORB uses an adaptive gyro-averaging technique, with a minimum of 4 points and a maximum of 32. This acts as a Bessel filter to reduce noise by smoothing out perturbations smaller than the gyroradius. The gyro-averaged electric field is given by

$$\langle \mathbf{E} \rangle = -\frac{1}{2\pi} \sum_{\mu} \phi_{\mu}(t) \int \nabla \Lambda_{\mu}(\mathbf{X} + \boldsymbol{\rho}_{Lij}(\alpha)) d\alpha. \quad (4.32)$$

The same gyro-averaging technique must be used both for the electric field as for the charge assignment, for optimum energy conservation.

4.4.5 Diagnostics

Various quantities of the plasma can be diagnosed by taking moments of the distribution function. The moment \mathbf{M} is taken by

$$\mathbf{M}(\mathbf{x}, t) = \int F(\mathbf{x}, \mathbf{v}, t) \mathbf{g}(\mathbf{v}) d\mathbf{v}, \quad (4.33)$$

where \mathbf{g} is some function of the velocity. \mathbf{M} are split up into the equilibrium and perturbed parts:

$$\mathbf{M} = \mathbf{M}_0 + \delta\mathbf{M}, \quad (4.34)$$

$$\mathbf{M}_0(\mathbf{x}) = \int F_0(\mathbf{x}, \mathbf{v}) \mathbf{g}(\mathbf{v}) d\mathbf{v}, \quad (4.35)$$

$$\delta\mathbf{M}(\mathbf{x}, t) = \int \delta f(\mathbf{x}, \mathbf{v}, t) \mathbf{g}(\mathbf{v}) d\mathbf{v}, \quad (4.36)$$

where F is the distribution function. Most of the time, we will want a flux surface-average of a quantity. The radial domain can be split into N_ψ radial bins with width $\delta\psi$. The k th surface has moment

$$\langle M \rangle_\psi = \frac{1}{V_k} \int_{V_k} F(\mathbf{x}, \mathbf{v}, t) \mathbf{g}(\mathbf{v}) d\mathbf{v} d\mathbf{x}, \quad (4.37)$$

where the volume of a flux surface bin is

$$V_k = \int_{\psi_{k-1}}^{\psi_k} \iint J(\psi, \theta_*) d\theta_* d\varphi d\psi. \quad (4.38)$$

The flux-surface average moment is now

$$\langle \mathbf{M}_0(\mathbf{x}) \rangle_\psi = \frac{1}{V_k} \sum \frac{V}{N} F_0(\mathbf{X}, v_\parallel, \mu) \mathbf{g}(v_\parallel, \mu), \quad (4.39)$$

$$\langle \delta\mathbf{M}(\mathbf{x}, t) \rangle_\psi = \frac{1}{V_k} \sum \frac{V}{N} w \mathbf{g}(v_\parallel, \mu), \quad (4.40)$$

where the sums are over markers that fall within the k th bin.

Because the $E \times B$ drift is responsible for the radial transport of heat and particles, the relevant moments are $g = \frac{1}{2} m v^2 v_{E \times B} \cdot \nabla \psi$ and $g = v_{E \times B} \cdot \nabla \psi$ respectively.

4.4.6 Conservation properties

Liouville's theorem states that phase space is conserved and incompressible. The full time derivative in gyro-centre space is given by

$$\frac{d}{dt} = \frac{\partial}{\partial t} + \frac{d\mathbf{X}}{dt} \cdot \nabla + \frac{dv_\parallel}{dt} \frac{\partial}{\partial v_\parallel}, \quad (4.41)$$

which allows us to state eq. (2.1) in another way:

$$\frac{\partial}{\partial t}(FB_{\parallel}^*) = -\frac{d\mathbf{X}}{dt} \cdot \nabla(FB_{\parallel}^*) - \frac{dv_{\parallel}}{dt} \frac{\partial}{\partial v_{\parallel}}(FB_{\parallel}^*), \quad (4.42)$$

which, upon integration leads to the conservation of particle number N :

$$\frac{dN}{dt} = \frac{\partial}{\partial t} \int FB_{\parallel}^* d\mathbf{X} dv_{\parallel} d\mu d\alpha \quad (4.43)$$

We can also derive an expression for the conservation of energy. First, we define the kinetic energy as

$$\mathcal{E}_{\text{kin}} \equiv \int (\mu B + \frac{1}{2} v_{\parallel}^2) FB_{\parallel}^* d\mathbf{X} dv_{\parallel} d\mu d\alpha, \quad (4.44)$$

Putting eq. (4.44) into eq. (4.41), and making use of eq. (4.42), we get

$$\frac{d\mathcal{E}_{\text{kin}}}{dt} = \int (\mu \nabla B + v_{\parallel} \frac{dv_{\parallel}}{dt}) FB_{\parallel}^* d\mathbf{X} dv_{\parallel} d\mu d\alpha, \quad (4.45)$$

where we have also used the fact that the magnetic field is stationary. Now, inserting eqs. (2.52) and (2.53) into eq. (4.45), we finally end up with an expression for the rate of change of kinetic energy:

$$\frac{d\mathcal{E}_{\text{kin}}}{dt} = q \int \frac{d\mathbf{X}}{dt} \cdot \langle E \rangle FB_{\parallel}^* d\mathbf{X} dv_{\parallel} d\mu d\alpha. \quad (4.46)$$

This is the nothing more than the power exchanged between the perturbed electrostatic field and the particles, which is $\mathbf{j} \cdot \mathbf{E}$, where $\mathbf{j} = qn_0 \mathbf{v}$ is the current. It can be shown[60] that the electrostatic field energy is given by

$$\mathcal{E}_{\text{f}} = \frac{1}{2} q \int (\langle n \rangle(\mathbf{x}, t) - n_0(\mathbf{x})) \phi(\mathbf{x}, t) d\mathbf{x}, \quad (4.47)$$

and that this exactly balances the rate of change of kinetic energy:

$$\frac{d\mathcal{E}_{\text{kin}}}{dt} = -\frac{d\mathcal{E}_{\text{f}}}{dt}. \quad (4.48)$$

4.4.7 Noise control

Noise in numerical simulations is a serious problem, and the control of noise without affecting the physical results can be difficult. NEMORB makes use of the physical property of ITG turbulence to align along field lines to both diagnose and control the noise. Because modes with high- k_{\parallel} should be rapidly Landau damped, energy in those modes is likely to be non-physical. The Fourier filter (\mathcal{F}) used in the solution

of the Poisson equation can be used to diagnose the noise. The signal is defined as:

$$\text{signal} = \frac{\frac{1}{a} \int_0^a \sum_{(n,m) \in \mathcal{F}} |\delta n^{(n,m)}(r)|^2}{\sum_{(n,m) \in \mathcal{F}}}, \quad (4.49)$$

while the noise is given by

$$\text{noise} = \frac{\frac{1}{a} \int_0^a \sum_{(n,m) \notin \mathcal{F}} |\delta n^{(n,m)}(r)|^2}{\sum_{(n,m) \notin \mathcal{F}}}. \quad (4.50)$$

Generally, simulations are assumed to only be physically relevant when the signal-to-noise ratio is above ~ 10 .

The noise-control technique used for nonlinear simulations in this thesis is coarse-graining, details of which can be found in [61]. The coarse-graining scheme involves binning the markers in the full 5D phase space, and moving the marker weights to the average value of their respective bins. This acts as an (unphysical) damping of small-scale (i.e. smaller than the bin size) phase-space structures. Therefore, care must be taken in determining the bin size so that only those scales which are not relevant to the transport are affected. Furthermore, in order for the coarse-graining to be effective, at each time-step there must be more than one marker per bin. Combined with the upper limit on bin size, this would place an unreasonable burden on the required number of markers. However, the coarse-graining does not have to be applied every time-step - typically it is only applied every tenth step - reducing the number of markers required by an equivalent factor.

4.5 Benchmarking

An important part of simulations is the benchmarking against other numerical codes. To this end, there has been an effort to standardise the testing of tokamak simulations using a set of reference parameters, known as the CYCLONE base-case[62]. These parameters have been taken from a high-confinement discharge on the DIII-D tokamak. They were then used as the basis for a series of simulations using a variety of different techniques, ranging from simple transport models and one-dimensional eigenmode calculations, to flux-tube gyrofluid and gyrokinetic simulations, to global gyrokinetic simulations. While NEMORB was not a part of this initial investigation, simulations have been performed using the CYCLONE parameters and compared to the original results[55], with excellent agreement.

Comparisons have also been performed for MAST equilibria, using the local gyrokinetic codes GS2[15] and GYRO[63]. As can be seen from fig. 4.3, there is

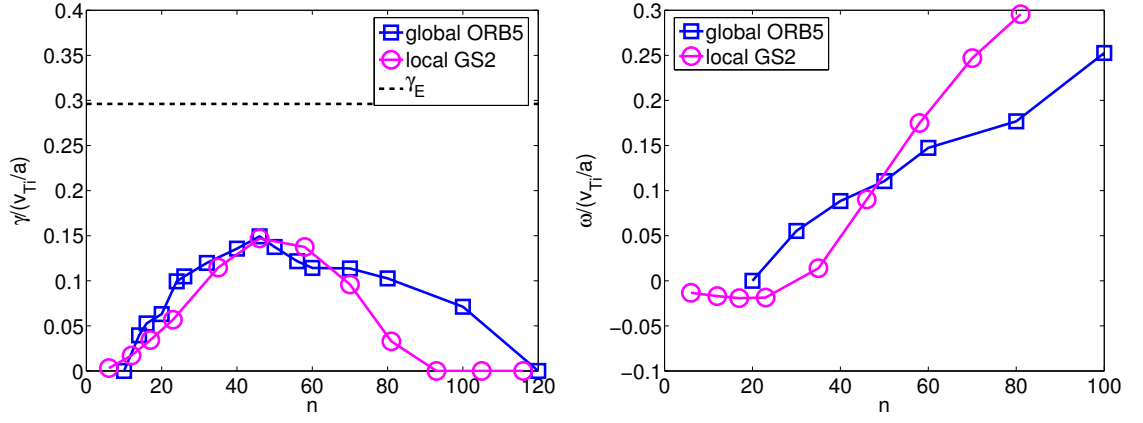


Figure 4.3: Comparison of linear growth rates (left) and real frequencies (right) between NEMORB (blue) and GS2 (magenta). Figure taken from [15], used with permission.

good agreement between NEMORB and GS2 when using adiabatic electrons in linear electrostatic simulations.

Chapter 5

Linear stability of global ITG modes in $E \times B$ flows

5.1 Introduction

It is well-known that sheared flows, whether the so-called “intrinsic” rotation[64, 65], self-generated by turbulence[34] or driven by external means (e.g. NBI)[22], can suppress turbulence[34, 49] or even stabilise the underlying linear mode driving the turbulence[34, 46]. There is an intuitive picture of how these sheared flows reduce turbulence; the flows tilt the eddies, stretching them and so reducing their perpendicular wavelength, allowing them to dissipate faster[34]. Sheared flow stabilisation is discussed in section 3.5. This suppression has been studied in the limit when the normalised gyro-radius $\rho_* = \rho_i/a$ becomes vanishingly small[45, 48, 66, 67], in both slab and toroidal geometries. In the $\rho_* \rightarrow 0$ (“local”) limit profile variations are neglected. Local codes often have a simulation domain on the order of hundreds of ρ_i . However, spherical tokamaks, such as MAST, have a small aspect-ratio and operate with finite ρ_* ($\sim 1/50$). The combination of these effects means that it is necessary to use global numerical codes which simulate the full 3D domain.

This Chapter focuses solely on electrostatic simulations. In general, due to their relatively high plasma β , electromagnetic effects are important in spherical tokamaks. However, simulations using the local gyrokinetic code GS2 show that while for H-mode discharges, electromagnetic effects are indeed crucial, they are not as important for L-mode shots[16], such as the one studied in this Chapter (discharge #22807). Electromagnetic effects have recently been included in NEMORB[14], and further work will incorporate these.

This chapter is structured as follows: in section 5.2 we present the physical

model used. We discuss the results of simulations with constant flow shear using an equilibrium model with concentric circular flux surfaces (section 5.3), and taking the equilibrium magnetic geometry from the MAST device (section 5.4), along with experimental flow profiles taken from MAST in section 5.5. In section 5.6, we briefly present the results of including kinetic trapped electrons in MAST geometry with experimental rotation profiles.

The work of this Chapter has been published as P. A. Hill, S. Saarelma, B. McMillan, A. Peeters, and E. Verwichte. *Perpendicular wavenumber dependence of the linear stability of global ITG modes on $E \times B$ flows* Plasma Phys. Control. Fusion, **54**, 065011, (2012).

5.2 Gyrokinetic Model

We model the plasma using the gyro-kinetic formalism (see chapter 2) and include a background radial electric field. This appears in the equations of motion as an $\mathbf{E} \times \mathbf{B}$ flow[68]. For a particle of mass m , electric charge q , parallel velocity v_{\parallel} , magnetic moment μ and real-space coordinates \mathbf{R} we have:

$$\frac{d\mathbf{R}}{dt} = \frac{v_{\parallel}}{B_{\parallel}^*} \mathbf{B}^* + \frac{v_{\perp}^2}{2\Omega_i B B_{\parallel}^*} \mathbf{B} \times \nabla B + \frac{(\mathbf{E}_0 + \langle \mathbf{E}_1 \rangle) \times \mathbf{B}}{B B_{\parallel}^*} \quad (5.1)$$

$$\frac{dv_{\parallel}}{dt} = \frac{\mathbf{B}^*}{m B_{\parallel}^*} \cdot [q \nabla(\phi_0 + \langle \phi_1 \rangle) + \frac{m v_{\perp}^2}{2B} \nabla B] \quad (5.2)$$

where $B_{\parallel}^* = \mathbf{b} \cdot \mathbf{B}^*$ is the parallel component of the generalised magnetic field, $\mathbf{B}^* = \mathbf{B} + (\frac{m v_{\parallel}}{e}) \nabla \times \mathbf{b}$, \mathbf{b} is the unit vector in the direction of the magnetic field, ϕ_0 is the equilibrium electrostatic potential, and $\langle \phi_1 \rangle$ is the gyro-averaged perturbed electrostatic potential. The equilibrium electrostatic potential does not appear in its gyro-averaged form as it does not vary on the length scale of the gyroradius. Therefore $\langle \phi_0 \rangle = \phi_0$. This formalism is valid in the “low-flow” regime, which holds when the equilibrium $E \times B$ speed is smaller than the thermal speed, $u_E \ll v_{th}$.

For the linear simulations, we select a single toroidal mode in each simulation, using a surface-dependent filter (the “diagonal” filter[55]) which suppresses high k_{\parallel} modes and keeps only poloidal modes with $m = [-nq(s) \pm \Delta m]$, where $\Delta m = 5$. The poloidal wavenumber spectra are then constructed by performing a scan in n and converting to $k_{\theta} \rho_i$ with the following equation:

$$k_{\theta} \rho_i = nq(s_0) \frac{r(s_0)}{R(s_0)} \rho_*, \quad (5.3)$$

where s_0 is the location of the peak temperature gradient (i.e. the location of the strongest drive).

We look at three different profiles of the background electrostatic potential:

1. an analytic profile that gives roughly constant flow shear across the domain in an *ad-hoc* equilibrium - concentric circular flux surfaces
2. the same profile in a true MHD equilibrium from MAST
3. an electrostatic potential that corresponds to an experimental profile of toroidal angular frequency in MAST

In the third case, we use the toroidal angular frequency profile (fig. 5.13) from TRANSP, a transport analysis code ¹, and the radial force balance equation[34]:

$$E_R = (Zen)^{-1} \nabla p - \mathbf{v} \times \mathbf{B}, \quad (5.4)$$

neglecting the pressure gradient term, to calculate the equilibrium electrostatic potential, ϕ_0 . ϕ_0 supports the perpendicular part of the toroidal rotation with the usual $E \times B$ drift. The parallel part is provided by a canonical Maxwellian[70] of the form:

$$f_0 = \frac{n_0(\psi_{\text{corr}})}{(2\pi T(\psi_{\text{corr}})/m)^{3/2}} \exp\left(-\frac{\epsilon - q\phi_0(\psi_c)}{T(\psi_{\text{corr}})}\right) \quad (5.5)$$

where m, q, T, n_0 and ψ are the mass, charge, temperature, density and poloidal magnetic flux, the energy is $\epsilon = \frac{1}{2}mv^2 + q\phi_0(\psi)$, and $\psi_c = \psi + mv_{\parallel}RB_{\varphi}/qB$ is the canonical momentum. ψ_{corr} is the “corrected” canonical momentum[71],

$$\psi_{\text{corr}} \equiv -\text{sign}(v_{\parallel}) \frac{q}{m} R_0 \sqrt{2(\epsilon - \mu B_0)} \mathcal{H}(\epsilon - \mu B_0), \quad (5.6)$$

which is used as a radial coordinate designed to reduce spurious parallel flows. Because $\psi - \psi_c$ is proportional to v_{\parallel} , parallel flows arise from the $\phi_0(\psi) - \phi_0(\psi_c) \propto E_R v_{\parallel}$ term in the exponent of f_0 . The poloidal part of this parallel flow almost entirely cancels the poloidal part of the $E \times B$ flow from ϕ_0 (there is a small residual poloidal flow from the temperature and density gradients), and the toroidal parts sum up to give the specified rotation profile. Because the parallel flow is provided by the Maxwellian, no new terms appear in the equations of motion; instead, new terms from the modification of the distribution function appear in $\frac{d\delta f}{dt}$ [70].

¹TRANSP is a time-dependent tokamak transport data analysis code, comprising numerous models for various transport and equilibrium process, including NBI heating, MHD equilibrium, neutral transport and angular momentum balance (which is used here to determine the angular frequency profile). While there is no single reference for the code, the TRANSP web page has collated references for most of the models it uses. Please see [69].

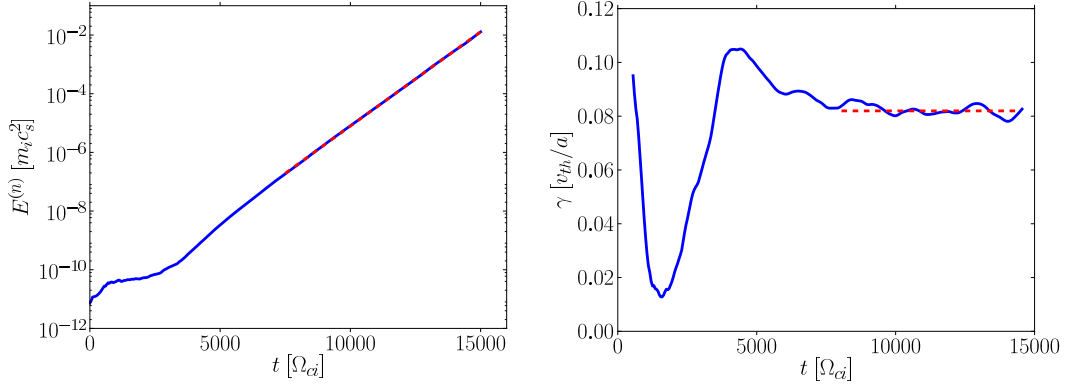


Figure 5.1: Typical plots of growth-rates. Left: Field energy in a single toroidal mode; Right: time-evolution of the growth rate. The red dashed lines in both figures indicate the time range over which the growth rate is calculated in the left-hand case, and over which it is averaged, in the right-hand case.

While the toroidal angular frequency is a flux function, it is not true that all other quantities are, for example, the density[72]. Because NEMORB is not currently able to handle poloidal variation of all these equilibrium quantities, and because we restrict ourselves to the low-flow regime, we perform the calculation of ϕ_0 on the outboard midplane and take this as a flux-surface function.

The growth rates are calculated from the field-energy, using MATLAB to perform the data analysis. NEMORB outputs the field-energy on an m, n, t grid in Fourier space for each time slice. This grid is summed over the m -modes to give the toroidal mode energy spectrum as a function of time and toroidal mode number. The energy for each mode is then logged (base-10) and a straight line fitted, the gradient of which is twice the growth-rate. The reason for doing it this way, as opposed to fitting an exponential straight away, is that the noise also grows exponentially. This can be very taxing for the fitting algorithms and often results in a poor fit compared with the former method. Another method is also used - the instantaneous growth-rate is found as a function of time by calculating the growth-rate for short time-periods and then averaging over some suitable period. The standard deviation of this average then gives us a better estimate of the uncertainty in the growth-rate compared to the first method, which often grossly over-estimates the error.

By looking at *ad-hoc* and MHD equilibria as well as analytic and experimental rotation profiles, we shall study flow shear stabilisation with a broad range of profiles. The *ad-hoc* case uses the *de facto* standard gyrokinetic case, the CYCLONE base case. The CYCLONE case is a set of standard parameters used to compare gyrokinetic codes and has been well studied. Using this scenario acts firstly as a

“sanity-check”, ensuring that we can reproduce well-established results. Secondly, it allows a degree of comparison between circular and shaped plasmas. The constant shear profile used in the first two cases is the simplest sheared flow profile but is not, however, a physical profile. This is because a flow driven solely by a radial electric field is necessarily mostly poloidal (due to the flow being perpendicular to the magnetic field), and poloidal flows are neoclassically damped in tokamaks. The last case uses a toroidal flow profile, computed using experimental data, allowing us to investigate the effects of a non-constant shear profile. This will also lay the groundwork necessary to perform nonlinear simulations, which permit direct comparison with experiment (see chapter 6).

5.3 The CYCLONE base case

We impose a purely radial, linear, electric field onto the CYCLONE base-case[62], with an *ad-hoc* equilibrium (circular, concentric flux surfaces). The main parameters are as follows: $T_e = T_i = 2$ keV, $B = 1.91$ T, minor radius $a = 0.625$ m, major radius $R = 1.70$ m, and normalised gyro-radius $\rho_* = 1/184.7$.

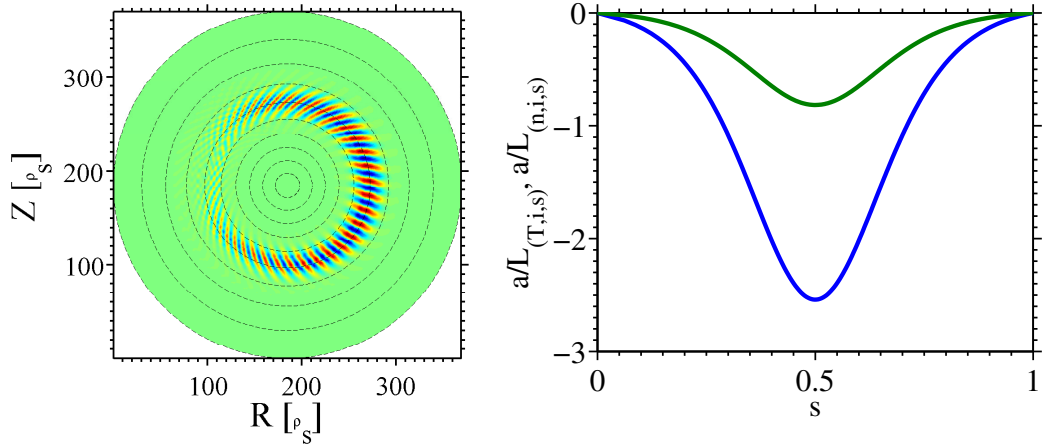


Figure 5.2: Left: poloidal cross section of perturbed electrostatic potential for the CYCLONE base case for $n = 30$, showing the equilibrium structure of concentric circular flux surfaces; Right: Radial profile of the logarithmic temperature (blue) and density (green) gradients

We use a temperature gradient profile, fig. 5.2, that peaks at $R/L_T = 6.9$ in the centre of the domain, and a similar density gradient profile that peaks at $R/L_n = 2.2$. This is different to the profile used in the global CYCLONE simulations, which had a constant R/L_T over most of the domain. This broad region of flat R/L_T leads to in a large drive everywhere, and modes may not be well localised.

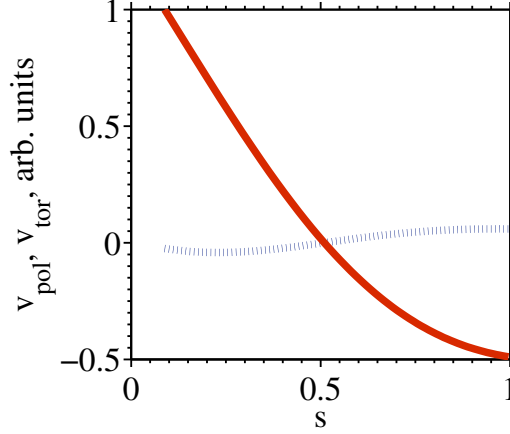


Figure 5.3: Shape of the components of the $E \times B$ velocity from the equilibrium potential; blue, dashed line: toroidal component; red, solid: poloidal component

For example, at zero flow shear, a mode with toroidal mode number n may start to grow at mid-radius. However, with the introduction of flow shear, it may shift and start to grow closer to the axis, with the result that its $k_\theta \rho_i$ will have changed (see eq. (5.3)). As we are trying to investigate the $k_\theta \rho_i$ dependence, we need to keep the modes well localised radially at high flow shear. A peaked profile localises the drive to the location of maximum R/L_T , and hence localises the modes. An unfortunate side-effect of this profile is that the narrow width increases k_r , which lowers the growth rate of the ITG mode[73].

The radial electric field creates an $E \times B$ flow mostly in the poloidal direction with constant shear across the whole domain. The inner and outer halves of the torus rotate in opposite directions in the laboratory frame. While poloidal flows are damped neoclassically, so this does not represent a physical rotation, it is the simplest rotation to impose, as it emerges from a radial electric field. Figure 5.3 shows the shape of the components of the imposed $E \times B$ flow. By scaling the size of the electric field we use, we change the size of these velocity profiles, though their relative amplitudes stay the same. We used a potential grid with a resolution of $N_s \times N_{\theta_*} \times N_\varphi = 64 \times 256 \times 128$ and $N_p = 1 \times 10^6$ markers.

In MAST, the relevant definition of the $E \times B$ shearing rate[66] is

$$\gamma_E = \frac{r}{q} \frac{d}{dr} \left(\frac{q v_{E \times B}}{r} \right) \quad (5.7)$$

where r is the minor radius and q is the safety function. This can be reduced to other, simpler, forms, given the large-aspect ratio and circular cross-section of the

CYCLONE case, but we use this definition in order to be consistent with the later MAST cases. Strictly, the $E \times B$ shearing rate is a function of poloidal angle - we ignore this variation and take γ_E at the outboard midplane.

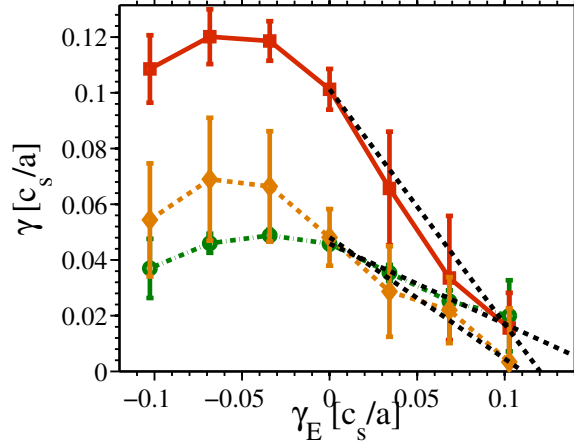


Figure 5.4: Growth rate against shearing rate for the CYCLONE case. green, circles: $k_\theta \rho_i = 0.19$; red, squares: $k_\theta \rho_i = 0.56$; orange, diamonds: $k_\theta \rho_i = 0.74$. Black dashed lines are fits used to calculate $\gamma_E^{\text{crit}}/\gamma_0$; γ_E^{crit} is defined as the value of γ_E where the lines cross $\gamma = 0$.

Figure 5.4 shows the growth rates of the fastest growing mode (FGM) against increasing flow shear, along with the growth rates for a shorter wavelength and for a longer wavelength mode. The growth rate and the shearing rate are both in terms of c_s/a , where $c_s = \sqrt{T_e/m_i}$ is the ion sound speed at $s = 0.5$ and a is the minor radius at the midplane. We calculate the uncertainties in the growth rates by first calculating the instantaneous growth rate using a rolling time window, usually around 1% of the total simulation time. We then take the mean growth rate of the latter half of the simulation and use the standard deviation as our uncertainty. Flow shear suppresses the faster growing modes more so than the shorter and longer wavelength modes. This is quantified in fig. 5.5.

We calculate $\gamma_E^{\text{crit}}/\gamma_0$ by fitting a straight line through the growth rates of individual modes and extrapolating the fit to $\gamma = 0$. The value of γ_E at this point is γ_E^{crit} . The black dotted lines in fig. 5.4 show the fits we used for those modes. We note that γ_E^{crit} is really the value of γ_E when the mode is effectively stabilised. The error-bars in fig. 5.5 come from the uncertainty in this fit. It is possible to observe a small remanent numerical growth rate for shearing rates larger than γ_E^{crit} , but this is no longer the physical mode with a given $k_\theta \rho_i$.

Here we see that the shearing rate needs to be at least 1.2 times the growth

rate at zero shear, γ_0 , for the FGM, and can be up to eight times γ_0 for other modes. While the value of $\gamma_E^{\text{crit}}/\gamma_0$ falls within the usual range (~ 1) for the FGM, it is much larger than expected (> 2) for other wavelengths, especially those with $k_\theta \rho_i < 0.2$, which have $\gamma_E^{\text{crit}}/\gamma_0 > 3$. We discuss a possible explanation in section 5.4.

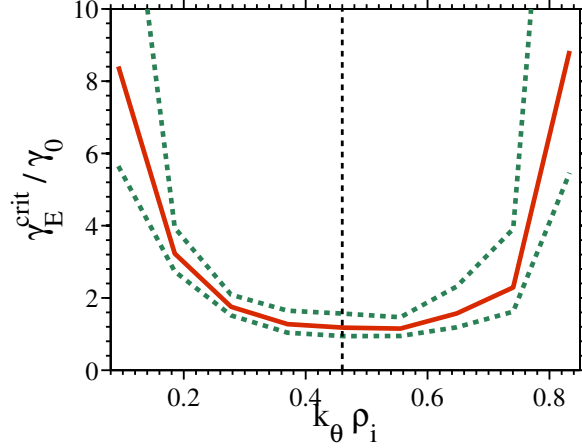


Figure 5.5: Variation of the ratio of $\gamma_E^{\text{crit}}/\gamma_0$ with $k_\theta \rho_i$ for CYCLONE base case. The green dashed lines show the 95% confidence intervals in $\gamma_E^{\text{crit}}/\gamma_0$. The black vertical dashed line shows the position of the FGM.

There are two factors responsible for the uncertainties in measuring γ . At low growth rates, the biggest factor is noise, which increases with time in PIC simulations without dissipation. The signal-to-noise scales proportionally to $\sqrt{N_p}$, while the cost of the simulation scales linearly with N_p . We have checked selected simulations for convergence by increasing the number of markers to 4×10^6 , 8×10^6 , and 16×10^6 . The growth rates and $\gamma_E^{\text{crit}}/\gamma_0$ change slightly - within the original uncertainties. The growth rates for modes with $\gamma_E \gg \gamma_E^{\text{crit}}$ do not converge for large numbers of markers. For the cases with $\gamma_E \neq 0$, we use 8×10^6 markers.

At large shearing rates, the modes start to exhibit Floquet-like behaviour - an exponential growth multiplied by some arbitrary periodic function, i.e. $\phi(\mathbf{x}, t) = \bar{\phi}(\mathbf{x}, t) \exp(\gamma t)$. In the local model, flow shear advects the mode structure poloidally into the good curvature region and then back into bad curvature. This effect means that the growth rate becomes time-dependent[48]. The mode is now no longer an eigenmode but has a new, time-dependent component and the growth rate has sinusoidal behaviour with a single frequency[42]. Unfortunately, this picture does not transfer to the finite ρ_* limit, and while only the eigenmode remains at long times[43, 74], there is still time-dependent behaviour in the growth rate. A large number of growth periods are then needed to accurately determine the true growth

rate. This can be seen directly in fig. 5.6, and indirectly in the increasing uncertainties in the growth rates in fig. 5.4 as the growth rates become smaller.

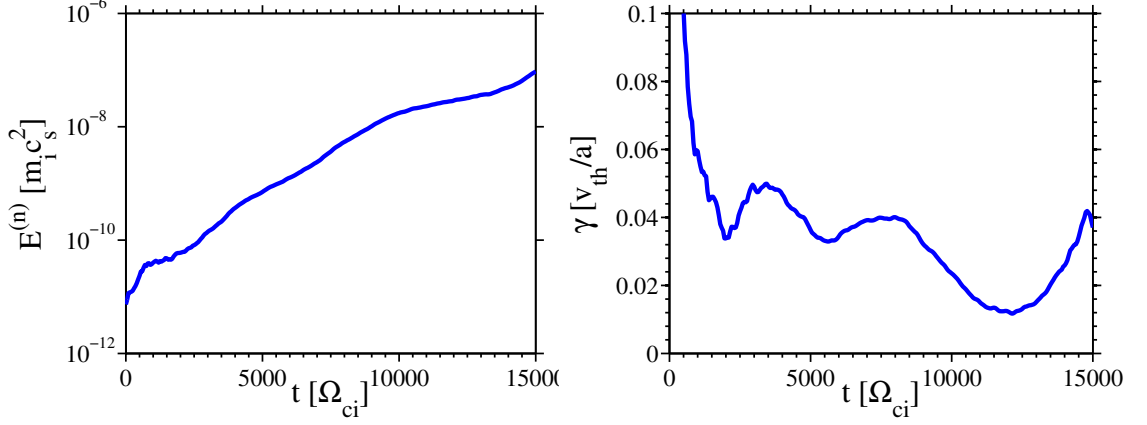


Figure 5.6: An example of the time-evolution of a mode with $\gamma_E \neq 0$. Left: Field energy; Right: growth rate. The growth rate shows time dependent behaviour, even at late times.

5.4 Small-aspect ratio, MAST-like equilibrium with analytic rotation profile

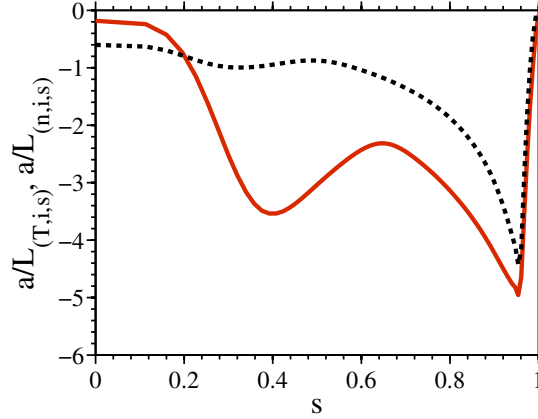


Figure 5.7: Radial profile of the logarithmic deuterium temperature (red, solid) and density (black, dashed) gradients. The gradients are reduced to zero from $s \geq 0.95$ in order to reduce the drive at the edge of the simulation domain. The electrons have the same profiles as the deuterium.

As a comparison to the CYCLONE case, we now turn our attention to a MAST

case (shot #22807), and use an equilibrium from a CHEASE[59] reconstruction of the magnetic field and temperature and density profiles from TRANSP (fig. 5.7). We use $\rho_* = 1/55.5$ and increase the poloidal resolution to $N_{\theta_*} = 512$ and the number of markers to 2×10^6 . While the temperature and density profiles are now both from real data, the electric field remains the same analytically presented radial field as in section 5.3. As poloidal rotation is strongly damped by neoclassical effects, this rotation profile is unphysical. However, there is still a similar dependence of $\gamma_E^{\text{crit}}/\gamma_0$ on $k_{\theta}\rho_i$. Figure 5.8 shows both positive and negative shearing rates, and it can be seen that there is an asymmetry in the suppression, with negative shearing rates requiring larger values of shear to effectively stabilise the mode. This is also seen in fig. 5.4. We have calculated the $\gamma_E^{\text{crit}}/\gamma_0$ values using the positive flow shear values.

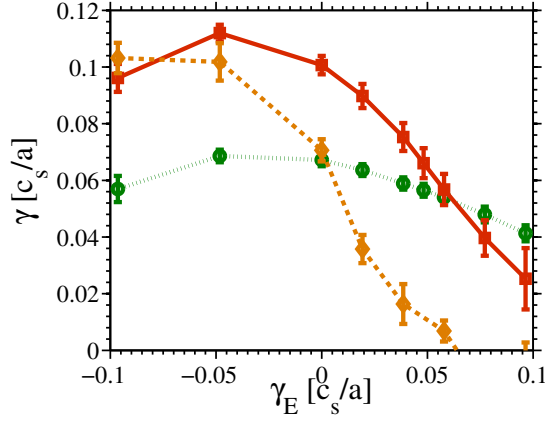


Figure 5.8: Growth rate against shearing rate for MAST equilibria and where the shearing rate is constant in radius. Green circles $k_{\theta}\rho_i = 0.14$, red squares $k_{\theta}\rho_i = 0.28$, orange diamonds $k_{\theta}\rho_i = 0.49$

Figure 5.9 shows the same variation in $\gamma_E^{\text{crit}}/\gamma_0$ as in the CYCLONE case, with the FGM having $\gamma_E^{\text{crit}}/\gamma_0 \sim 1$ and longer wavelengths needed a much larger ratio.

The Waltz quench rule[34, 45], that turbulent transport is eliminated when γ_E exceeds γ_0^{max} , is derived in the context of nonlinear turbulence and does not strictly apply to linear studies. Still, our finding of $\gamma_E^{\text{crit}}/\gamma_0 \sim 2$ for the FGM is in broad agreement with this rule. We can look at a similar nonlinear quench rule[75] of the form $\gamma_E^{\text{crit}}/\gamma_0 = (\Delta k_x/\Delta k_y)$, where $\Delta k_{x,y}$ are the radial and poloidal inverse turbulence correlation lengths, to see whether this rule, or a modified form, captures the variation of $\gamma_E^{\text{crit}}/\gamma_0$.

From ballooning theory[46, 74], the radial and poloidal widths of the ITG

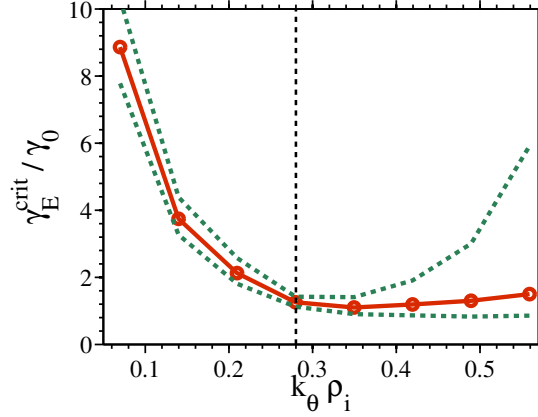


Figure 5.9: Variation of the $\gamma_E^{\text{crit}}/\gamma_0$ with $k_\theta \rho_i$ for MAST equilibrium with linear E_r for positive shearing rates. The green dashed lines show the 95% confidence intervals in $\gamma_E^{\text{crit}}/\gamma_0$. Vertical dashed line shows location of FGM.

mode are given by

$$\Delta r \propto (k_\theta \rho_i)^{-1/2}, \quad (5.8)$$

$$\Delta \theta \sim (k_\theta \rho_i)^{-1}. \quad (5.9)$$

The aspect ratio of the mode ($\epsilon_{\text{mode}} = \Delta \theta / \Delta R$) is then given by

$$\epsilon_{\text{mode}} \propto (k_\theta \rho_i)^{-1/2}. \quad (5.10)$$

We have measured the aspect ratio of the mode by looking at the poloidal cross-section of the potential with zero applied toroidal flow. Figure 5.10 illustrates how this was done. The full algorithm for measuring the aspect ratio of the mode structure is as follows:

- First, the potential is taken on an (s, θ_*) grid at some late time when the mode structure is fully developed.
- Next, the radial location, s_{max} , of the maximum potential amplitude is found
- The extrema of the potential along s_{max} are found, and the extrema closest to outboard midplane, $\theta_* = 0$, is determined.
- The contour at half the amplitude of this extrema is calculated using MATLAB's `contourc` routine.
- An open-source, specialised ellipse fitting routine is then used on this contour to determine the geometric properties of the mode structure.

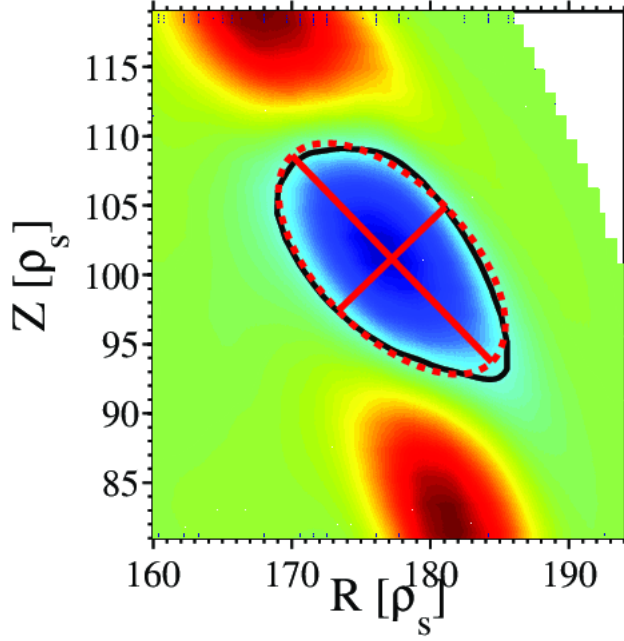


Figure 5.10: An illustration of measuring the aspect ratio and area of a mode structure. The black line is the contour level at half the peak amplitude of the perturbation closest to the outboard midplane. The dashed red line is an ellipse fitted to this contour.

Several methods were used to calculate the aspect ratio, though they all turn out to give equivalent results. The results presented here use

$$\epsilon_{\text{mode}} = \frac{|R_{\text{max}} - R_{\text{min}}|}{|Z_{\text{max}} - Z_{\text{min}}|}, \quad (5.11)$$

where $R_{\text{max,min}}$ are the maximum and minimum R values of the ellipse (and equivalently for Z). Due to the small angular size of the modes, we make the assumption that the height of this contour is equivalent to the poloidal width. Figure 5.11 shows the measured and predicted values of ϵ_{mode} for the static adiabatic electron case, with a constant of proportionality of 0.66 on the predicted value. While ϵ_{mode} may predict the value of $\gamma_E^{\text{crit}}/\gamma_0$ close to the FGM, it fails to capture the steep increase for long wavelengths as well as the turning point around $k_{\theta}\rho_i \sim 0.3$. However, the area of the mode, estimated by calculated the area of the fitted ellipse, does track the variation in $\gamma_E^{\text{crit}}/\gamma_0$ reasonably well, up to the FGM. Again, this does not capture the turning point close to the FGM, but as the shape of the growth rate spectrum itself is due to two competing mechanisms, it is plausible that the shape

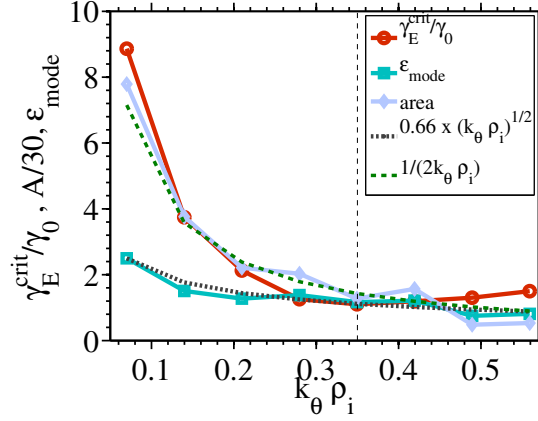


Figure 5.11: Area, cross-sectional aspect ratio as compared to $\gamma_E^{\text{crit}}/\gamma_0$

of the $\gamma_E^{\text{crit}}/\gamma_0$ is due to two different processes.

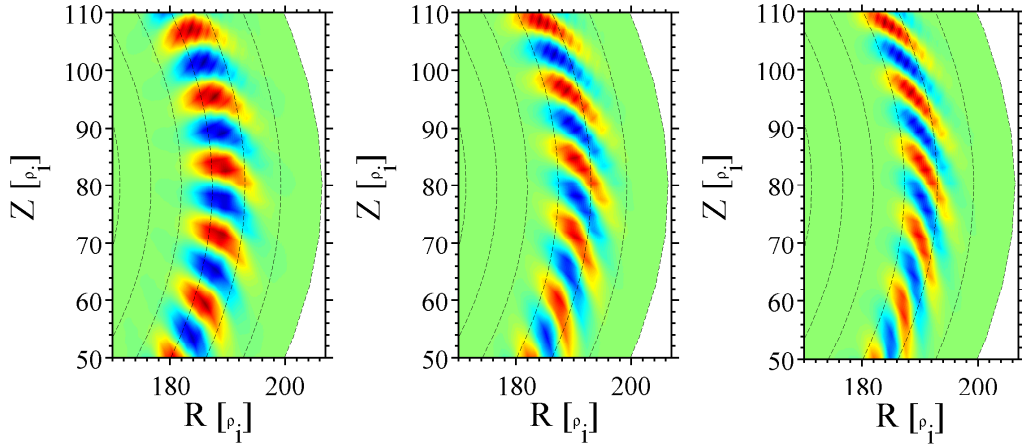


Figure 5.12: Poloidal cross-section of the perturbed electrostatic potential for different shearing rates. Left to right: $\gamma_E = -0.064$, $\gamma_E = 0.00$, $\gamma_E = 0.064$ (Experimental level $\gamma_E = 0.64$). Note that in the static case (centre figure), the mode structure is already tilted due to profile variation causing a shear in the local mode frequency, while with 10% of the experimental shear in the co-current direction, the mode structure is more radial.

Figure 5.12 demonstrates the cause of the asymmetry in the sign of the shearing rate. At zero flow shear, the longer wavelength modes are already tilted due to the diamagnetic shear[46, 76]. The equilibrium quantities vary over the length scale of the instability, changing its local mode frequency. This acts in a similar way to flow shear, tilting the structure and reducing its linear growth rate. Increasing the flow shear in one direction first acts to un-tilt the mode structure and

undoing the effects of the local mode frequency shear. Increasing the flow shear even further tilts the mode in the opposite direction, suppressing it. Because the local mode frequency shear is caused by profile variation, this suppression asymmetry is not captured by the local model. This is a clear example where a global code which retains all the profile variation effects is required to capture the suppression asymmetry.

It should be mentioned that the magnetic shear, \hat{s} , also twists the mode structure. At the outboard midplane, the mode will be tilted through an angle, θ_0 , which is approximately given by[46]:

$$\theta_0 \simeq \left| \frac{\omega'_r + \omega'_f}{2\hat{s}k_\theta\hat{\gamma}_0} \right|^{1/3} \quad (5.12)$$

where ω'_r, ω'_f are the diamagnetic and flow frequency shearing rates, and $\hat{\gamma}_0$ is the growth rate from 1D ballooning theory. In the absence of both profile and flow shear, the mode remains entirely radial at the outboard midplane, although the magnetic shear does twist it along the field line. It can be seen from (eq. (5.12)) that the flow shear only has to compete with the diamagnetic shear to “un-tilt” the mode.

5.5 Small-aspect ratio, MAST-like equilibrium with experimental rotation profile and adiabatic electrons

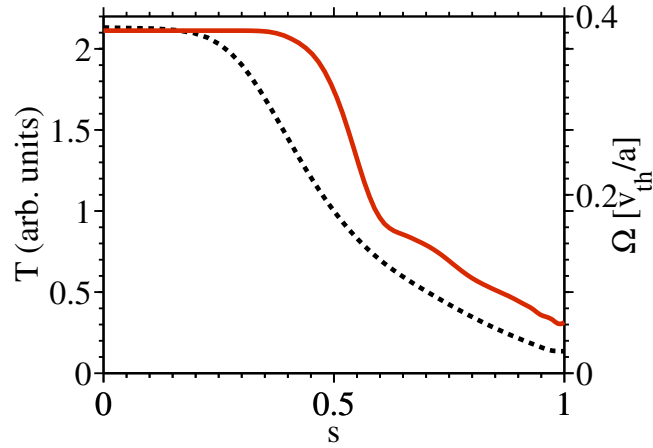


Figure 5.13: Toroidal angular frequency (red, solid, right axis) and deuterium temperature (black, dashed, left axis) profiles from MAST shot #22807. The temperature is normalised to its value at $s = 0.5$. The strong gradient in the rotation profile around $s = 0.5$ corresponds to a steepening in the temperature profile - an indication that there is a transport barrier.

Instead of the linear electric field used above, we use the field from a real MAST shot and the Maxwellian described in section 5.2. This combination of electric field and “shifted” Maxwellian produces a toroidal rotation profile, shown in fig. 5.13. We performed a scan in the flow shear by scaling the whole rotation profile by some factor and measuring the mean flow shear over the region $s = 0.6 - 0.8$, which is where the modes sit. The flow shear is roughly constant over this region and is $\gamma_E = 0.63$ for the experimental rotation profile. The parallel velocity shear introduced by the v_{\parallel} profile acts as an additional drive for the ITG – however, this drive only becomes important at Mach numbers larger than those investigated in this Chapter, as we restrict ourselves to the low-flow case. Compared with the constant shear case ($\gamma_E^{\text{crit}}/\gamma_0 \sim 1$), the FGM for the experimental rotation profile needs slightly more flow shear to effectively stabilise it, $\gamma_E^{\text{crit}}/\gamma_0 \sim 2$. The maximum growth rate occurs at $\gamma_E = -0.06$, 10% of the experimental shear.

The linear modes are easier to stabilise with flows in the negative toroidal direction (positive shearing rates). In our equilibrium, both the magnetic field and the current point in the anti-clockwise direction. The flow, then, is in the counter-current direction. This has a nice correspondence with experimental results, where better confinement is achieved with counter-current rotation[77].

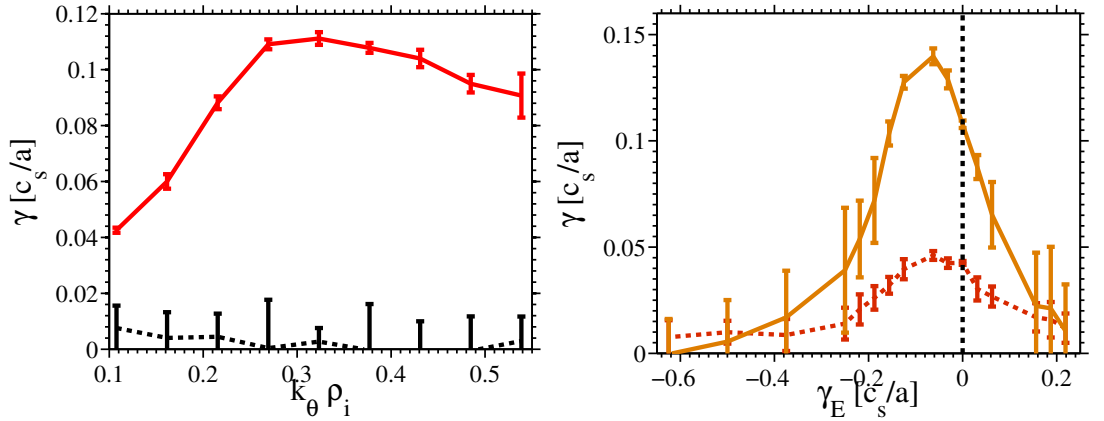


Figure 5.14: Left: Growth rate spectrum with (black, dashed) and without (red, solid) flow. Right: Asymmetry with respect to shear direction for the FGM (orange, solid; $k_{\theta} \rho_i = 0.32$) and a long wavelength (red, dashed; $k_{\theta} \rho_i = 0.11$) mode

The temperature gradient at the radial location where the mode with $k_{\theta} \rho_i = 0.33$ is confined is $a/L_T = 2.8$. In order to assess how close to marginal stability the experiment is, we use an analytic gradient profile which peaks at the mode location. We scan the peak gradient around $a/L_T = 2.8$ and find that the linear threshold appears around $a/L_T = 3.5 \pm 0.5$ for $k_{\theta} \rho_i = 0.33$. The uncertainty on the gradient

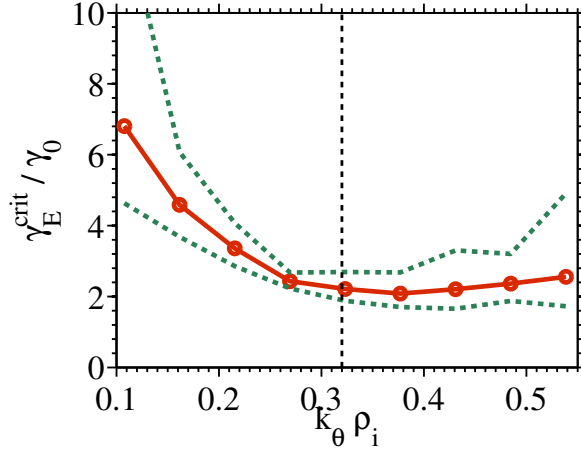


Figure 5.15: Variation of $\gamma_E^{\text{crit}}/\gamma_0$ with $k_\theta \rho_i$ for MAST shot #22807. Vertical dashed line indicates location of FGM.

threshold value is controlled by the accuracy by which we can determine growth rates in PIC simulations close to stability.

5.6 MAST-like equilibrium with experimental rotation profile and kinetic trapped electrons

We now include the effects of kinetic trapped electrons into the previous case, section 5.5. Because of the magnetic geometry of MAST, trapped electrons play a significant role in the turbulent dynamics of the device. There are some issues involved with simulating electrons in gyrokinetic models. The fast parallel motion of electrons means that a short time step is needed. This can be counteracted by decreasing the electron-ion mass ratio, but even then, numerical instabilities can develop in the electrostatic case if the time-step is too long[78]. The computational cost of a simulation is inversely proportional to its time-step, meaning that simulations with kinetic electrons can be computational prohibitive. An alternative hybrid model can be used instead[79], where the trapped electrons are treated kinetically and the passing electrons remain adiabatic. The trapped electrons are actually assumed to be drift-kinetic - that is, their gyroradius is taken to be negligible. This has several benefits. Firstly, the number of markers can be reduced, as only a fraction of phase space needs to be simulated; or, alternatively, the trapped part of phase space can be filled with the same number of markers, increasing the resolution for the same computational cost. Additionally, this hybrid scheme converges to the correct growth rate quicker (as a function of the mass ratio) than the fully kinetic

scheme[14]. This allows us to use a smaller ion/electron mass ratio, and thereby use longer time steps.

We use 8×10^6 markers for both the ion species and the electrons. Because the growth rates do not depend strongly on the electron-to-ion mass ratio, but the required temporal resolution does, we reduce the mass ratio from the physical value of 5.44×10^{-4} to 5×10^{-3} . We also increase the spatial resolution to $N_\theta = 1024$, $N_\varphi = 512$ in order to capture the smaller spatial scales associated with the TEM-ITG.

The trapped electrons couple to the ITG modes (see section 3.3), enhancing their growth rates without flow compared with adiabatic electrons by a factor of 5 or more (cf. section 5.5). Figure 5.16 shows the $k_\theta \rho_i$ spectrum of growth-rates.

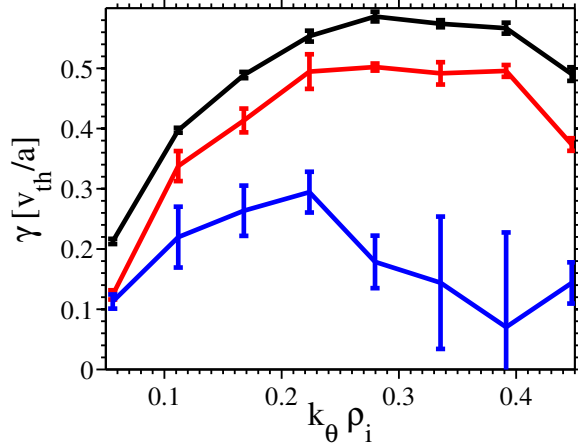


Figure 5.16: Growth rates against perpendicular wavenumber including the effect of kinetic trapped electrons (cf. fig. 5.14). Red: $\gamma_E = -0.63$; black: $\gamma_E = 0.0$; blue: $\gamma_E = 0.63$

In the co-current direction with the experimental flow level, the growth rates are reduced to about half the static case. The growth rates are reduced to a third of the static case with counter-current rotation. In both cases, the growth rates are above those of the ITG with adiabatic electrons.

The peak of the growth rate spectrum moves from $k_\theta \rho_i \sim 0.42$ in the static case to $k_\theta \rho_i \sim 0.35$ with co-current rotation and $k_\theta \rho_i \sim 0.28$ with counter-current rotation. Taking a quasi-linear estimate of the diffusivity, $\chi \sim \gamma/k^2$, the longer wavelengths will contribute more to the transport. So while the FGM from the static case has been reduced substantially, the overall effect on transport will be less significant. In order to calculate this effect properly, it is necessary to perform fully non-linear simulations[15].

The asymmetry caused by the local mode frequency shear is enough to cause

a significant difference in the linear growth rates of co- and counter-current flows, and thus for the quasi-linear transport. If this effect carries over to the non-linear case, then in order to accurately determine heat fluxes in MAST using gyrokinetic models, it will be necessary to use global simulations.

5.7 Conclusion

We have studied how the ratio of critical $E \times B$ shearing rate to the static growth rate, γ_0 , varies with $k_\theta \rho_i$. We have investigated this variation using both an analytic electric field which gives constant flow shear across the domain as well as a real rotation profile from the MAST experiment.

The amount of flow shear required to effectively stabilise the linear ITG mode depends strongly on $k_\theta \rho_i$ for all the cases. The constant shear profile in circular geometry with the CYCLONE parameters has $\gamma_E^{\text{crit}}/\gamma_0 \sim 2$ for the FGM. $\gamma_E^{\text{crit}}/\gamma_0$ increases for both longer and shorter wavelength modes, with $\gamma_E^{\text{crit}}/\gamma_0 \rightarrow 10$ for $k_\theta \rho_i < 0.2$. The same profile in a MAST equilibrium with experimental parameters has a similar dependence. When the experimental rotation profile is used, the dependence varies less strongly with $k_\theta \rho_i$, with the longest wavelengths ($k_\theta \rho_i < 0.2$) having $\gamma_E^{\text{crit}}/\gamma_0 \rightarrow 7$. This dependence of $\gamma_E^{\text{crit}}/\gamma_0$ on $k_\theta \rho_i$ appears to be related to the size/shape of the mode structure. The area of the mode, as calculated from ellipses fitted to the electrostatic potential structure on the outboard mid-plane, is correlated with $\gamma_E^{\text{crit}}/\gamma_0$ for wavelengths longer than the FGM.

Flow shear stabilisation acts asymmetrically, with negative shearing rates increasing growth rates of the instabilities before stabilising them. The maximum growth rate occurs at 10% of the experimental rotation level in the co-current direction (negative shearing rates) for simulations with adiabatic electrons. Rotation in the counter-current direction (positive flow shear) on MAST is more stabilising. The asymmetry is caused by profile variation creating a shear in the local mode frequency, requiring a fully global treatment of MAST plasmas.

While rotation at the experimental level does reduce growth rates of the TEM-ITG coupled mode, it remains above the level of the ITG mode with adiabatic electrons, regardless of the shear direction. The peak of the growth rate spectrum moves to longer wavelengths as shear in the counter-current direction increases. In order to ascertain the effect on transport, fully non-linear simulations will be performed[15].

Chapter 6

Nonlinear simulations of ITG/TEM turbulence and comparison with MAST experiments

The work presented in this Chapter was done in collaboration with Samuli Saarelma, Anthony Field and Young-chul Ghim. In particular, all simulations presented were performed by the author (except where otherwise mentioned). The synthetic BES analysis in section 6.5 was performed in part by S. Saarelma and A. Field. Figures 6.19 to 6.21 and 7.6 to 7.8 were produced by A. Field.

6.1 Introduction

The crucial difference between linear and nonlinear simulations is the inclusion of the $\langle E \rangle$ term in the v_{\parallel} and \mathbf{X} equations of motion. Essentially, this means that in linear simulations particles are not accelerated by the perturbed electric field. The linear modes do not saturate in linear simulations¹ and turbulence does not develop. Modes are linearly coupled, hence in linear simulations scans we include only a single mode per simulation. Nonlinear simulations must include several modes, and most importantly the $n = 0$ mode (the zonal flow, section 3.4.1), which is essential in determining the correct nonlinear saturation state as it regulates the turbulence (see section 3.4.1).

¹They may, however, develop numerical instabilities when they reach large amplitudes.

Turbulent transport in MAST has been an area of research focus for some time now[10, 16, 22, 23, 66, 77, 80, 81], and while simulations of particular effects have been compared to experiment, notably studies of ELMS[82, 83] and transport[77, 84, 85], there have been to date no direct comparisons of gyrokinetic turbulence simulations to experiment.

Nonlinear NEMORB simulations, in general, go through two or three distinct phases. The first phase is the linear phase, during which the initial perturbation grows exponentially, until it reaches a certain amplitude (which is not known *a priori*), whereupon it saturates. The length of the linear phase varies according to two main factors: the growth rate of the particular microinstability and the saturated amplitude. For the simulations presented in this thesis, the typical duration of the linear phase is in the region of $1 - 2 \times 10^3 \Omega_{ci}^{-1}$. This saturated amplitude may not be the real steady-state turbulence state, as the $n = 0$ zonal flow may take longer to reach a saturated level. After this so-called overshoot period (the length of which varies enormously between simulations, or may not be present at all), the turbulence maybe be damped by the zonal flow, leading to a reduction in the amplitude of the turbulence. In well-resolved simulations, this final phase is a (quasi) steady-state, and it is this phase which we seek to compare with experiments. The equilibrium profiles used in the simulations do not evolve in time, therefore we are seeking a time-independent state. This can present some difficulties, as it requires that the experiment is also in a time-independent steady-state (or for the simulation to be able to handle arbitrary, time-dependent sources and sinks). Due to the short discharges in MAST, this is not always possible. This represents a source of potential discrepancy between simulation and experiment, though it is hard to estimate the exact level of uncertainty arising due to this.

In general, nonlinear simulations are difficult to perform. Due to their chaotic nature, a small change in the initial starting conditions can lead to vastly different final states[73]. Nonlinear simulations can be incredibly sensitive to numerical, as well as physical, parameters, meaning that careful testing and tuning of numerous controls is necessary.

An unresolved question with simulations of plasma turbulence is that of the correct time to end them. It is not possible to know *a priori* when a simulation has reached a steady-state[86]. While a simulation may appear to have reached a time-independent turbulent state, there may be some slow growth or decay (either physical or numerical) which only manifests on time-scales much longer than a given simulation. This is an open problem in nonlinear gyrokinetic simulations.

It is important to remember that we are not trying to find the exact micro-

state of the turbulence, but rather statistical properties of the turbulence given some physical conditions. Ideally, therefore, we would repeat all the simulations, merely varying the initial perturbed state, ensemble average the results, and only talk about the properties of the ensemble average. However, given the cost (computational, temporal and economical) of performing one simulation, this is not always possible.

All of the nonlinear simulations performed in this Chapter have some basic physical and numerical parameters in common. The common physical parameters are taken from MAST shot #22807; the temperature, density and rotation profiles have all been processed through TRANSP, while the magnetic equilibrium is from CHEASE. This is the same MAST shot used in the previous chapter, and in the publications [1, 15]. The temperature, density and rotation profiles can be seen in figs. 5.7 and 5.13. The rotation profile for the counter-current flow case presented in this Chapter was obtained by multiplying the co-current rotation profile by a factor of -1 . The common numerical parameters have been tuned using linear simulations and are listed in table 6.1.

n modes	0-80
Δm	10
N_s	64
N_{θ_*}	512
N_φ	256

Table 6.1: Common simulation parameters

As discussed in section 5.6, kinetic electrons significantly increase the linear growth rates of the ITG. This larger growth rate leads to larger $v_{E \times B}$, and so to larger fluxes. Previous nonlinear simulations[15] show that the assumption of adiabatic electrons leads to fluxes below the neoclassical level (see fig. 6.1), clearly far too small to explain experimental results. Increasing the temperature gradient profile by up to 30% (fig. 6.1) demonstrates that this particular discharge is close to marginal stability, as the heat flux starts to grow to appreciable levels with increasing drive. Kinetic electrons must then be included in order to come close to the experimental fluxes as they increase the linear drive for the ITG, and so lead to larger heat fluxes.

6.2 Tuning parameters

One of the major difficulties in performing nonlinear simulations of plasma turbulence is the tuning of numerical parameters. Generally, to see the effect a parameter

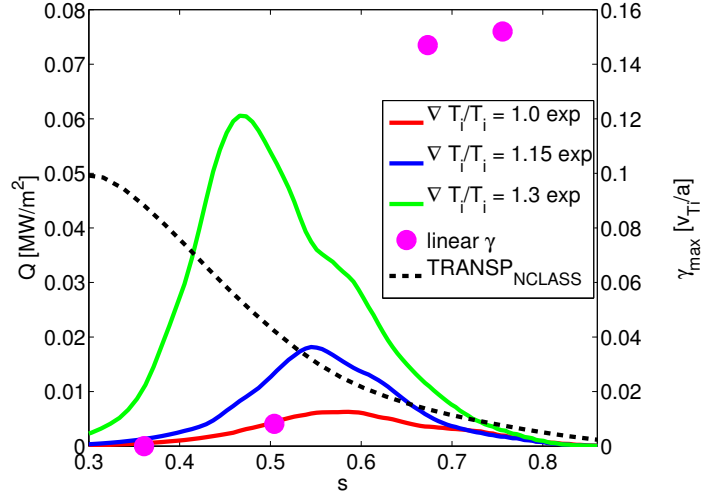


Figure 6.1: Heat fluxes from simulations using adiabatic electrons (red) are below the neoclassical level (black, dashed) predicted by TRANSP. Increasing the temperature gradient profile by 15% (blue) and 30% (green) indicate that this case is close to marginal stability. This figure used with permission from [15].

has requires several simulations per “control knob”. Thus, the cost of a single non-linear simulation has to also take into account the possibly dozen or more “tuning” simulations that were run beforehand.

6.2.1 Noise

It has been found empirically that nonlinear simulations have a practical signal-to-noise ratio (SNR) lower limit of 10 in order for them to be physically relevant[56]. Below this value, the results of simulations tend to start to diverge significantly. See section 4.4.7 for definitions of signal and noise - they are essentially the energy in the modes inside/outside of the Fourier filter, respectively. There are numerous ways to ameliorate the noise in nonlinear simulations, ranging from noise control schemes that explicitly try to reduce the noise, to improving the fidelity through the number of markers used. The Krook operator scheme[86] was used previously in ORB5 to reduce noise by introducing a linear damping rate applied to all the modes, with the zonal flow component being projected out². Currently, the coarse graining technique discussed in section 4.4.7 is used in the majority of NEMORB simulations run. We compare the two approaches, as illustrated in fig. 6.2. Please note that here, we have already tuned the parameters for each case. We want to increase the

²It is possible to find an analytic form for the zonal flows, which is why this is possible

SNR as much as possible without affecting the physics. Figure 6.2 compares the SNR for the coarse-graining scheme to that of the Krook operator, as well as the growth rate spectrum during the linear phase. The coarse-graining scheme not only has a better SNR by the end of the simulation, but it also reproduces the linear growth rates more accurately (cf. fig. 5.16). It is also compatible with collisions, which the Krook scheme is not.

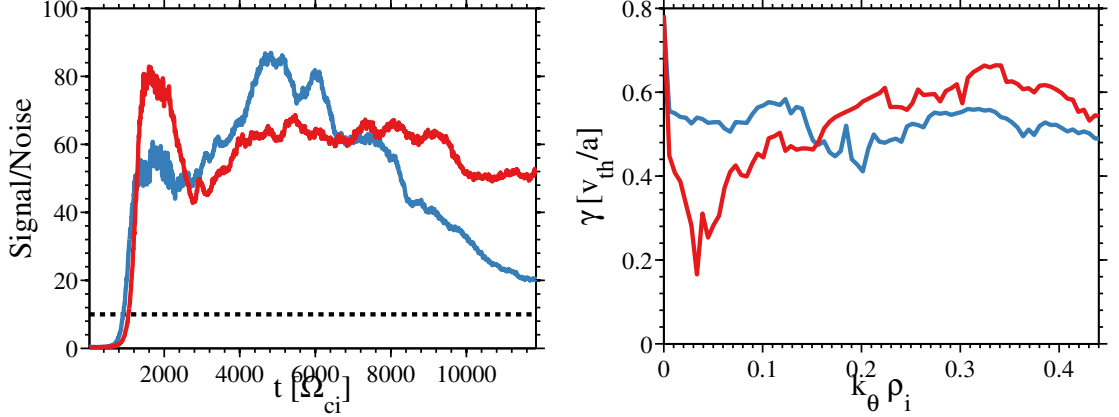


Figure 6.2: Left: Signal-to-noise ratio comparing the Krook operator (blue) and coarse-graining noise control (red) schemes. The SNR here excludes the signal in the $[n, m] = 0$ modes, which would otherwise dominate the ratio. Right: Growth rates during the linear phase ($t = 1 \times 10^3 \rightarrow 2 \times 10^3$) for the Krook operator (blue) and coarse-graining noise control (red) schemes.

The coarse-graining scheme has free parameters which, unfortunately, need to be adjusted by hand. This noise control scheme involves binning markers in 5D phase space and moving the markers' weights to the average weight of that bin. The nature of the coarse-graining is to damp fluctuations on scales smaller than the bin size. The size of the bins along each dimension of the phase space is therefore crucial to get right, in order to not affect those scales which are physically relevant to the turbulent transport. A sensible choice then for the spatial dimensions of the coarse-graining grid is choose them the same as the grid used to solve the electrostatic potential. Actually, this can be improved by choosing a field-aligned grid (detailed in [61]), allowing larger bin sizes than otherwise possible while still not damping physically relevant scales. The remaining two dimensions are those in normalised kinetic energy $E = v^2/2T(s)$ and pitch-angle $\xi = v_{\parallel}/v$, where v is the marker velocity and $T(s)$ is the temperature at radius s . The number of bins along E and ξ need to be adjusted by hand. Figure 6.3 compares how changing the number of bins in energy space affects the SNR. Note that here, we used 400M markers. While

it might be expected that more bins would affect the physical modes less, in fact the opposite occurs. The likely explanation for this is that, with more bins, there are now fewer markers per bin. This appears to have an adverse affect on both the SNR as well as the physical modes.

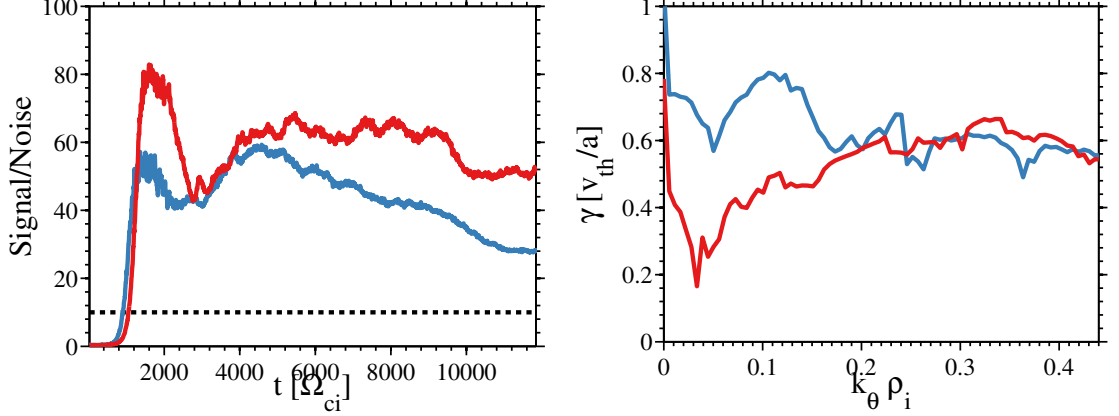


Figure 6.3: Signal-to-noise ratio comparing the number of bins per direction in energy space: 8 bins (red) versus 32 bins (blue). The larger number of bins decreases fidelity, most likely because there are now fewer markers in each bin. This could be moderated by decreasing the frequency of the coarse graining. Growth rates during the linear phase ($t = 1 \times 10^3 \rightarrow 2 \times 10^3 \Omega_{ci}^{-1}$) for 8 bins (red) and 32 bins (blue).

The other free parameter which needs to be adjusted by hand is the damping rate, γ_{cg} . This is the rate at which marker weights are relaxed towards the average weight of a given bin, and depends strongly on the physical quantities of a simulation. If the coarse-graining is applied every N time steps, which are of length δt , then the only requirement on γ_{cg} is that $N\delta t\gamma_{cg} \ll 1$. See section 7.3.1 for details of how this was adjusted.

6.2.2 Shielding

We have to include an artificial shielding term in the Poisson equation close to the LCFS. Particle flux hitting the edge of the simulation domain leads to numerical instabilities. These arise because the boundary condition $\phi = 0$ is imposed at the edge. Particle flux can lead to markers reaching the edge, causing there to be non-zero weight there. The combination of these two effects leads to the quasineutrality equation not being solved exactly, in turn leading to a spurious electric field at the edge. To reduce this as much as possible, in calculating the potential from the density during the poisson equation, a shielding term is included. This raises the effective background density near the edge and reduces the importance of fluctuations

there. The density is modified as

$$n_0(\psi) \rightarrow n_0(\psi)n_{sh}, \quad (6.1)$$

where the shielding term, n_{sh} , is:

$$n_{sh} = 1 + \kappa_{sh} \sinh\left(\frac{\psi}{\Delta_{sh}}\right) \left[\sinh\left(\frac{1}{\Delta_{sh}}\right) \right]^{-1}, \quad (6.2)$$

where $\kappa_{sh} = \frac{a}{L_{n,sh}}$ and Δ_{sh} are input parameters. This has to be carefully done so as not to affect important physical fluxes. Unlike the noise control mechanisms, this can be fairly easily tuned without having to run several large nonlinear simulations. This is done simply by selecting a large value of κ_{sh} (the simulations here all use $\kappa_{sh} = 50$), and then choosing an appropriate value of Δ_{sh} (here, $\Delta_{sh} = 0.02$) such that the shielding term is almost unity where there is substantial (physical) heat flux.

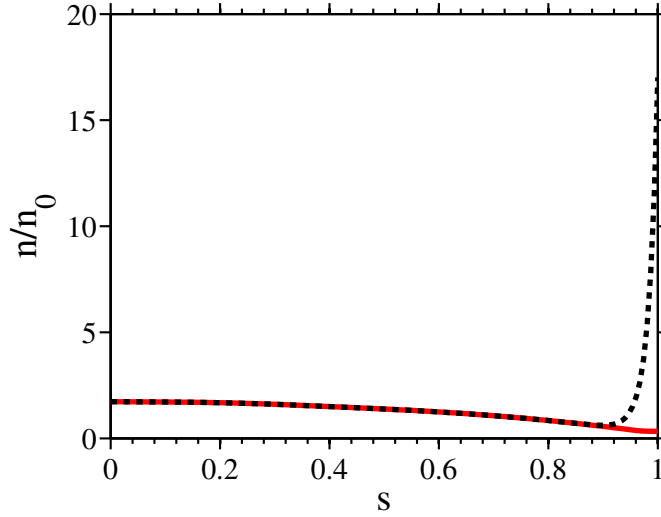


Figure 6.4: Normalised density profile with (black, dashed) and without (red) the additional shielding term. The shielding parameter used here are $\Delta_{sh} = 0.02$ and $\kappa_{sh} = 50$.

6.2.3 Heating

There exist two main types of nonlinear simulations: flux-driven, or gradient-driven[73, 87]. In the former case, the fluxes are set *a priori*, with the system evolving to a state where eventually the profiles are steady and can be measured. In the latter case, the gradients are known, and the system is evolved to the point where the

fluxes are steady and can be ascertained.

Anomalous radial heat flux from the turbulence tends to relax the profiles. This will inhibit the drive for the microinstabilities that drive the turbulence. Therefore, a source of heating is needed which will counteract/balance the profile relaxation without affecting the physics. This works by applying a source S_H to each flux surface, damping the perturbed distribution function on a characteristic time scale, γ_H :

$$S_H = -\gamma_H \left\{ \delta f(\epsilon, s) - F_0(\epsilon, s) \frac{\int \delta f(\epsilon, s) d\mathbf{v}}{\int F_0(\epsilon, s) d\mathbf{v}} \right\}, \quad (6.3)$$

where $\epsilon = \frac{1}{2}mv^2$ is the kinetic energy. The second term in eq. (6.3) is a correction designed to conserve the density on each flux surface. More details of the heating source can be found in [86]. While the input parameter γ_H must be adjusted manually, a reasonable estimate is to set it to one tenth the maximum linear growth rate [61]. The correct heating rate of $\gamma_H = 3 \times 10^{-4} \Omega_{ci}$ was found from previous simulations performed by S. Saarelma.

6.2.4 Markers

The noise in PIC simulations is proportional to $N^{-1/2}$, where N is the number of markers. When $N \rightarrow \infty$, the simulation accurately reproduces the model. Unfortunately, this slow dependence on the number of markers means that accurate simulations can be costly. Increasing the SNR by a factor two requires four times as many markers, and given that the computational cost of a run is proportional to N , this leads to a factor four increase in the cost³.

We increased the markers from 100M to 400M. It can be seen from fig. 6.5 that increasing the number of markers leads to a larger improvement in the SNR than expected (in this case). We get a factor 3 better SNR for 4 times as many markers - faster than the predicted factor 2 increase.

6.3 Transport

In linear simulations, the markers are not moved by the perturbed fields and so measures of flux from these simulations are therefore meaningless. To do this, the perturbed fields are simply not included in the v_{\parallel} equation of motion, eq. (4.9). Including the perturbed fields in the equations of motion leads to fluxes from the

³Slight gains can be made on this by changing the number of processors the problem is run on. Larger problems may fit more neatly onto a given number of cores. Of course, this is highly dependent on the architecture.

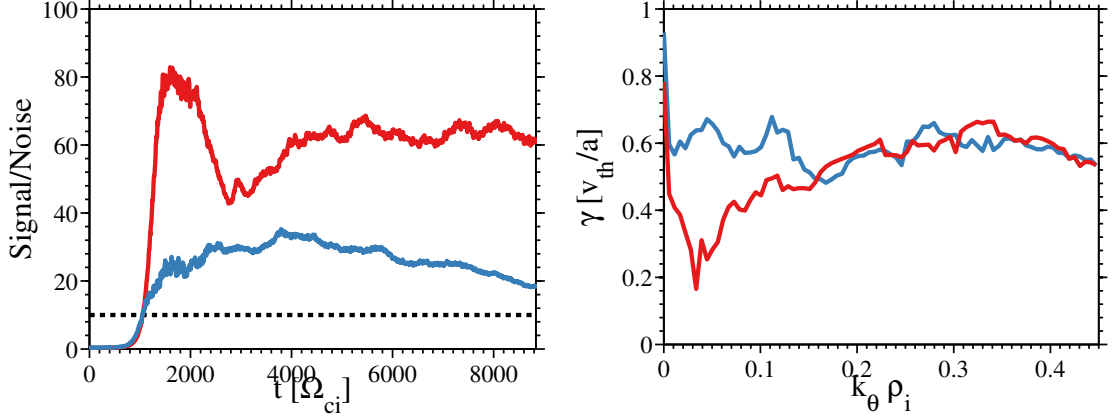


Figure 6.5: Signal-to-noise ratio comparing the number markers: 400M (red) versus 100M (blue). Growth rates during the linear phase ($t = 1 \times 10^3 \rightarrow 2 \times 10^3$) for 400M (red) and 100M (blue).

thereby generated turbulence (see section 1.3.2 for a discussion of the origin of these fluxes). The fluxes for nonlinear simulations are calculated using the diagnostics given in section 4.4.5.

The diffusivities for the various transported quantities (particles, heat and momentum) are calculated from the profiles. The exact transport mechanisms responsible are difficult to identify and break down, however, an effective diffusivity can be determined. This assumes that there is no convective process alongside the diffusion and that the turbulent transport is a purely diffusive process⁴. An effective diffusivity can then be calculated from

$$\chi^{\text{eff}} = \frac{\Gamma_G}{\nabla G}, \quad (6.4)$$

where Γ_G is the flux of quantity G with gradient profile ∇G .

In reality, there may be other contributions to the flux from gradients in other equilibrium quantities - so-called “off-diagonal” transport. This term comes from putting the fluxes of particles, heat and momentum into a 3×3 matrix. The diagonal terms take the form of eq. (6.4), while the off-diagonal terms are of the form $\chi = \Gamma_G / \nabla H$, where G, H are different equilibrium quantities. For example, thermo-diffusion is a particle flux arising from temperature gradients. The momentum transport may also have contributions from the Coriolis and centripetal forces.

The heat flux is calculated by using the function $g = \frac{1}{2} m v^2 v_{E \times B} \cdot \nabla \psi$ in eq. (4.40), which is the energy transported by the $E \times B$ velocity in the radial direc-

⁴Probably not the case.

tion. This then gives the heat flux, Q . The thermal diffusivity, χ_i , is then calculated by using Q and the temperature gradient, ∇T_i , in eq. (6.4).

It is possible to use data from the relevant shot to convert the simulation fluxes from normalised NEMORB units into SI. The normalisation from the heat flux in NEMORB units, Q^{NEMORB} , into SI units (MW m^{-2}), Q^{SI} is as follows:

$$Q^{SI} = Q^{NEMORB} n_0^{TRANSP} T_{e,s_0}^{TRANSP} c_{s,s_0}^{TRANSP} e^{SI}, \quad (6.5)$$

where n_0^{TRANSP} , T_{e,s_0}^{TRANSP} , c_{s,s_0}^{TRANSP} are the bulk density, electron temperature (eV) and sound speed (ms^{-1}), respectively, at the flux surface $s = s_0$ taken from TRANSP, and e^{SI} is the electron charge in SI units. Doing so reveals that the simulations predict fluxes a few times larger than experiment, as determined by TRANSP simulations.

The flux-surface average heat fluxes for the static and co-flow cases are depicted in fig. 6.6. These show avalanche-like bursts that propagate radially in both directions, a common feature of nonlinear ITG simulations. Various models of this bursty behaviour have been proposed[88, 89], all of which involve an interaction between the turbulent potential fluctuations and the zonal flows generated by the turbulence. The general principle of avalanches is that the turbulence leads to a local steepening of the temperature profile (say, for heat fluxes), triggering an instability which propagates in both directions. Bursty behaviour is an inherently nonlinear effect, as it involves a complex interplay between the turbulence and the self-generated shear flow which moderates the turbulence.

The momentum flux is calculated using the function $g = v_{\parallel} v_{E \times B} \cdot \nabla \psi$ in eq. (4.40), and the diffusivity is calculated from using the toroidal momentum associated with the parallel velocity, $G = P_{\parallel} = v_{\parallel}(s)|_{\varphi} R^2$, in eq. (6.4). However, it should be noted that is not quite the correct form for a small aspect ratio, highly shaped plasma, such as MAST, as it makes use of the large aspect ratio approximation. When the work in this thesis was performed, the correct momentum diagnostics had not yet been fully implemented. More advanced diagnostics are currently being implemented, such as Reynolds stress. Future work that makes use of these features would enable a more in-depth analysis of the interaction of rotation in MAST with the momentum flux.

Figure 6.7 depicts the momentum fluxes in the static and co-flow simulations. The other rotating cases are essentially similar in character to the co-rotation, differing mainly in the magnitude. The momentum flux in the simulation without flow is factor 3–4 smaller than the simulation with flow. In the static case, there is a small

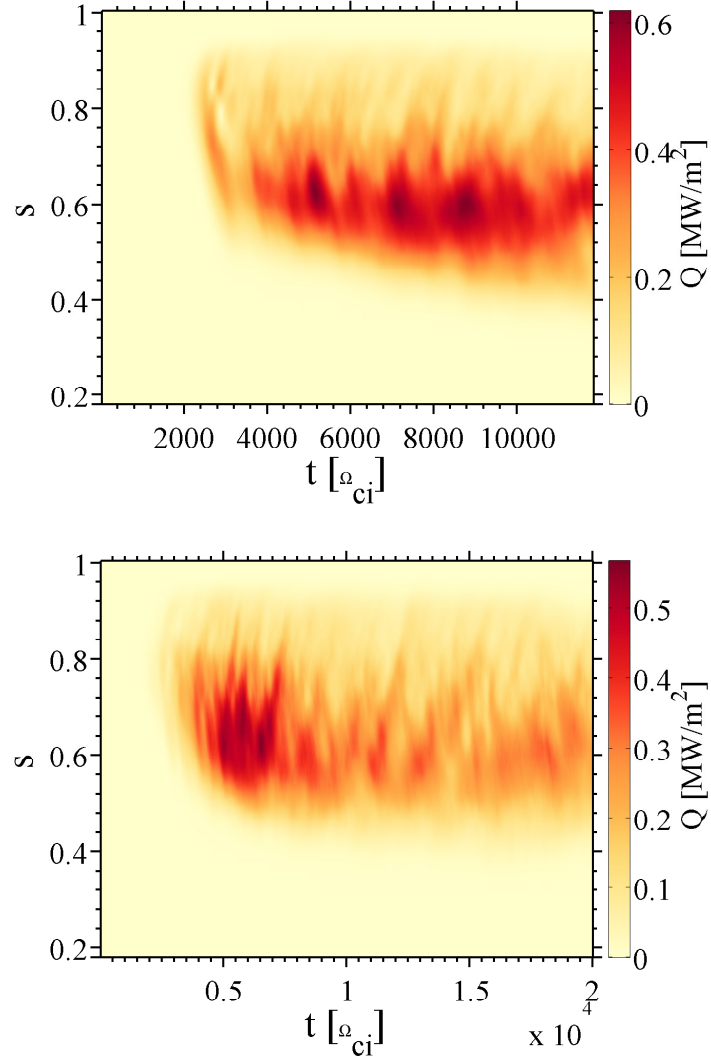


Figure 6.6: Flux-surface average heat fluxes as a function of radius and time for zero (left) and co-current rotation (right).

profile of P_{\parallel} which arises from the pressure gradient[70], which is 4 – 6 times smaller than the rotating case, and is almost flat across the whole radius. However, not only is the magnitude of the momentum diffusivity, χ_{φ} , more than triple the co-rotating simulation, but it also changes sign around $s = 0.75$, whereas the simulations with flow have a χ_{φ} which remains positive across almost the entire radial domain. This points to the momentum flux being essentially off-diagonal in character - that is, not arising from the rotation profile, which is monotonic and close to zero. The large χ_{φ} in the static simulation is due to the assumption that the flux is diffusive, which is clearly not the case. In simulations that contain a background rotation,

the diagonal part of the momentum flux becomes dominant (i.e. the flux becomes more diffusive), causing a reduction in the momentum diffusivity.

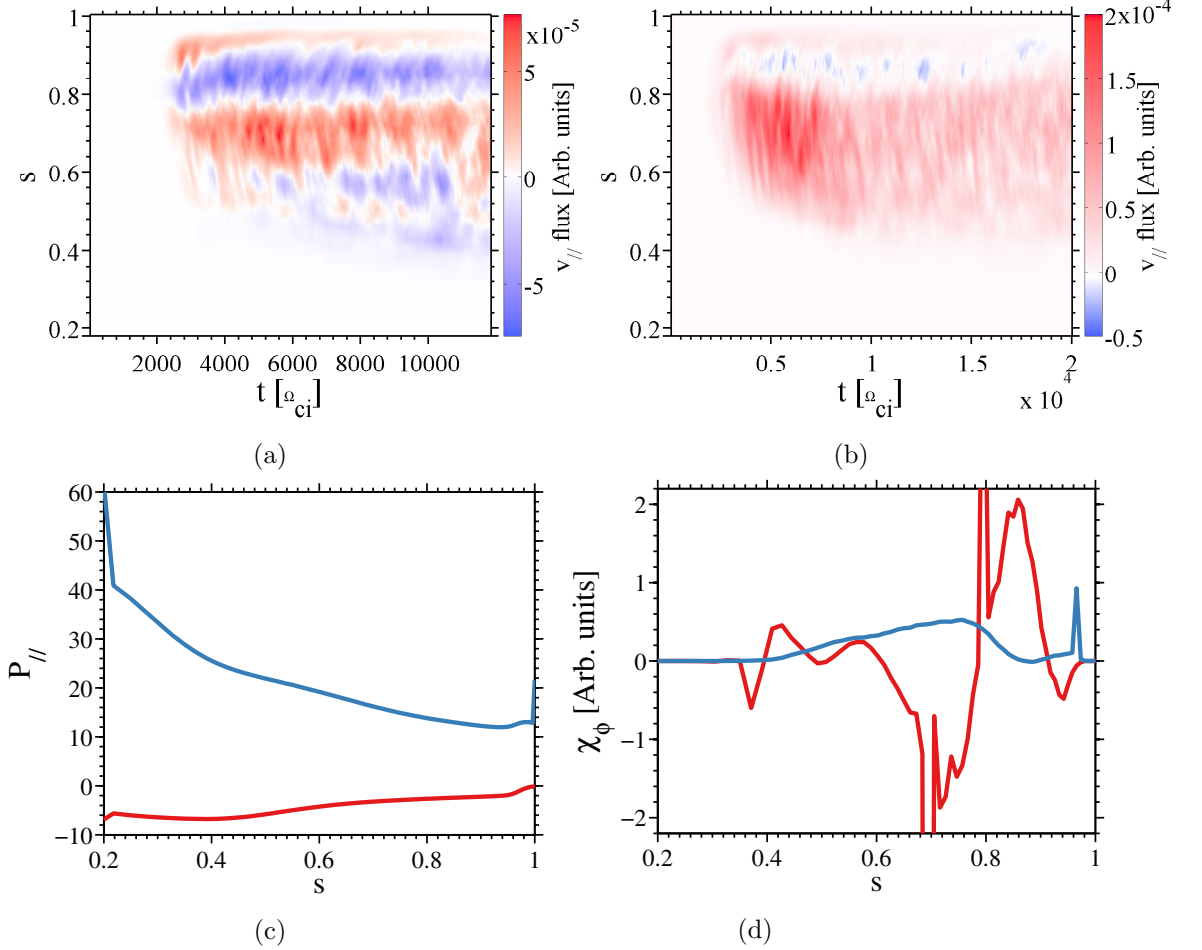


Figure 6.7: Parallel momentum fluxes for the static (a) and co-rotating (b) cases as a function of s and time. The parallel toroidal momentum is shown in (c), while the resulting momentum diffusivity is shown in (d) for the static (red) and co-rotating (blue) cases.

It is possible to characterise the momentum transport with a single number - the Prandtl number, Pr . This is defined as the ratio of momentum and thermal diffusivities: χ_ϕ/χ_i . The Prandtl number is typically of order unity. From MAST experiments, TRANSP values are in the range 0.1 to 10. Other simulations (of other cases) find 0.1-0.3 or ~ 1 . Figure 6.8 shows the late-time average, flux-surface average Pr as a function of radius for the simulations with flow. Note that the standard deviations are approximately 100% due to the large standard deviation from the momentum diffusivity. All the cases have $P_r \sim 0.1 - 0.2$ across most of the

radial domain, neglecting the edges where the momentum gradient profile becomes noisy. The counter-rotation cases have a peak around $s = 0.85$, where Pr reaches 0.6. The case without flow has a large Prandtl number of order unity.

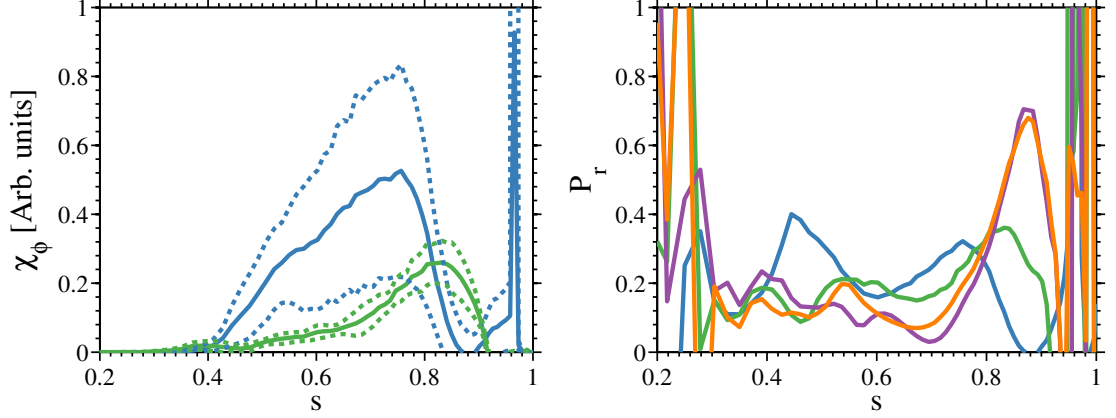


Figure 6.8: Left: Momentum diffusivity, Right: Prandtl number. Co-rotation (blue), counter-rotation (green), half-counter- (orange) and three-quarters-counter flow (purple) (see section 6.4.1).

6.4 Comparison with linear studies

After tuning the various numerical parameters in order to perform a simulation with a reasonable degree of confidence in the results, the next step is to compare the results with the linear simulations (the majority of which were already performed for the previous Chapter). There are three main features from the linear studies that we can compare with the nonlinear simulations:

1. the reduction in growth rates with increasing flow shear,
2. the shift in peak growth rate to longer wavelengths with increasing flow shear,
3. the asymmetry in shear stabilisation with respect to shear direction.

It is important to note here that these are effects of the flow shear on the linear growth rates, while we are interested in the flow shear's effects on (nonlinear) turbulence properties. There is not a one-to-one relation between the linear growth rates and any turbulent property, so it is not clear *a priori* that we should see, say, a comparable reduction in the heat flux to the reduction in the growth rates. If we could predict properties of the turbulence from linear simulations, then we could get away without performing the complex, expensive nonlinear simulations.

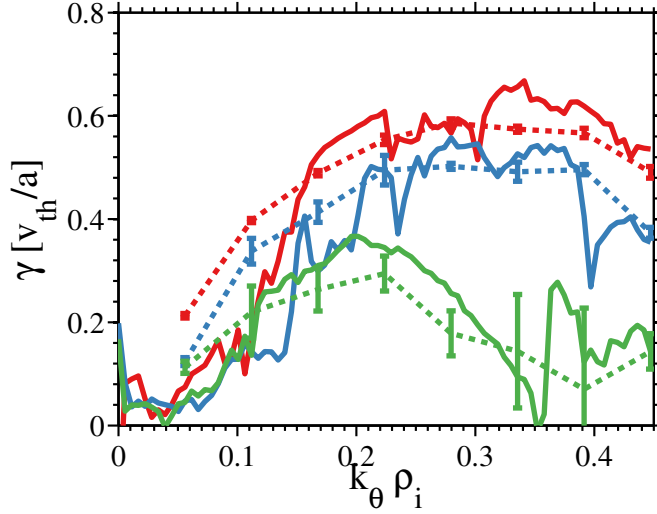


Figure 6.9: Growth rates during the linear phase of nonlinear simulations (solid lines) versus growth rates of linear simulations (dashed lines) for the static (red), co- (blue) and counter-rotating (green).

The first thing that we can verify is that the growth rates during the linear phase of the nonlinear simulations behave in a similar fashion to the linear growth rates. This is shown in fig. 6.9, and it is clear that, during the linear phase at least, there is no major change in the physics. The longer wavelengths, below $k_\theta \rho_i < 0.15$, appear to have smaller growth rates in the nonlinear simulations than in the linear runs. This is because the growth rates have to be calculated during a short time-window. Due to their smaller growth rates, the physical modes take longer to appear out of the initial noise, and so the time-window used may capture some of the period before some modes start growing. A later time-window can lead to a similar problem, as the modes start to saturate at different times, the window can capture some of the saturated state, also leading to a reduced growth rate for some of the modes. The relative “noisiness” of the nonlinear data is a result of the coupling between the modes. The linear growth rates appear comparatively well behaved, as they include only a single mode per run. Also note that the linear simulations do not include $k_\theta \rho_i = 0$, as this is linearly stable, and is driven through interaction with the other modes.

Figure 6.10 shows the flux surface averaged heat flux for the static and co-rotating cases. Please see section 6.4.1 for some important caveats as to the counter-flow data. The heat fluxes in fig. 6.10 have been averaged over “late times” - that is, after the overshoot period, and during the steady-state phase. However, due to the nature of nonlinear simulations, it is difficult to systematically define this period

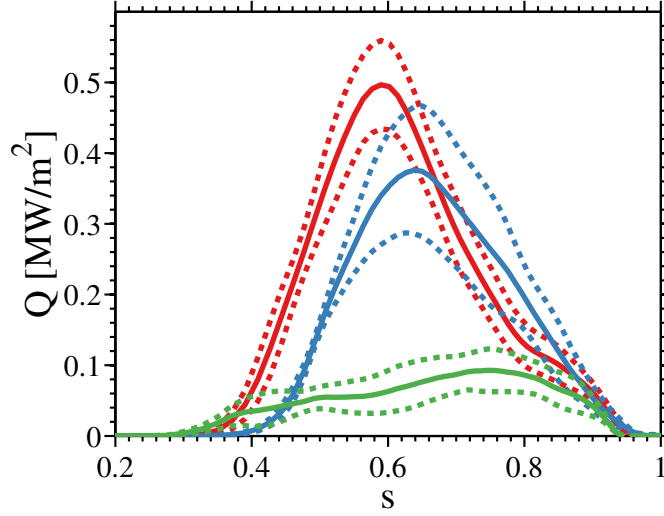


Figure 6.10: Late time average, flux surface averaged heat fluxes for static (red), co- (blue) and counter- (green) flows. Solid lines are the time-averaged values; dashed lines are the standard deviation. The counter-flow heat flux was still decreasing during this late time average, and the SNR was less than 10, so values should be treated with caution. Heat flux has been converted to SI units (see section 6.3)

across all cases. For example, looking at the static and co-flow cases (fig. 6.6), the static simulation does not appear to have any overshoot to speak of, while the co-rotating plasma has a significant overshoot before dropping down to a relatively stable steady-state. A possible diagnostic is the time-evolution of the zonal flow component of the electrostatic potential, illustrated in fig. 6.11. As the zonal flow component often takes longer to reach saturation than the other modes present in the system, it is then reasonable to assume that the whole system has reached a steady-state when the $n, m = 0$ mode stops evolving. For example, the zonal flow reaches saturation at $t \sim 7.5 \times 10^3 \Omega_{ci}^{-1}$ (fig. 6.11), which corresponds to the end of the overshoot period in the heat flux (fig. 6.6). This by no means a perfect diagnostic: in the static case (fig. 6.11), the zonal flow appears to still be evolving even during late times, even after the heat flux (fig. 6.6) has reached a (quasi-) steady state.

As expected, the inclusion of a background sheared flow results in a reduction in the heat flux from a peak of 0.5 MW/m^2 for the static case to 0.38 MW/m^2 for the co-flow case. The counter-current case has a peak Q of 0.09 MW/m^2 , though, as discussed in section 6.4.1, this value depends on the time-window used.. The peak Q moves outwards from $s = 0.6$ in the static case to $s = 0.64$ with co-flow, and to $s = 0.76$ with counter-flow. The reason for this is either due to the flow shear

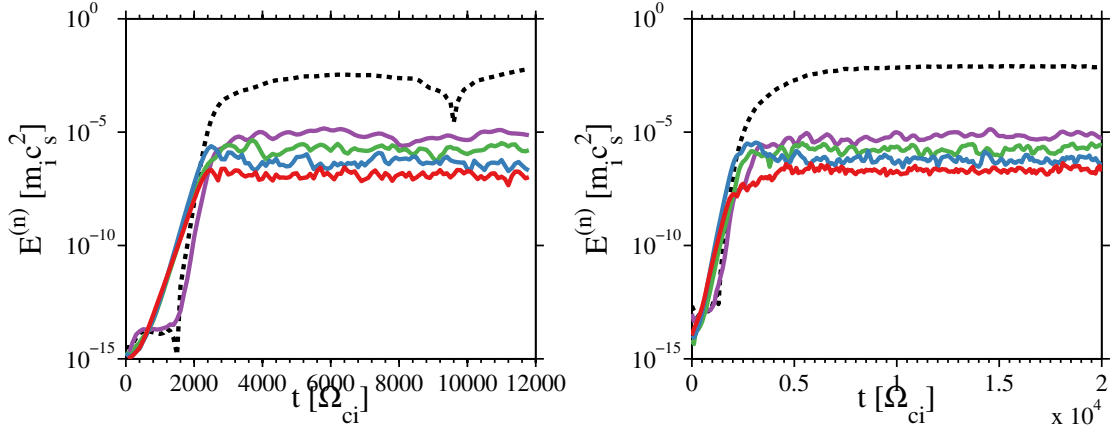


Figure 6.11: Evolution of the energy in certain modes with time. The zonal flow component (black, dashed), $n = 20$ (purple), $n = 40$ (green), $n = 60$ (blue) and $n = 80$ (red) are depicted. Left: The static case. Right: The co-flow case.

suppressing turbulence spreading to the linearly stable core region, or due to the flow shear stabilising weakly growing modes at the mid-radius, which may become dominant over the faster growing modes in the outer region during the nonlinear phase in the static case.

While we can compare the reduction in the linear growth rates with the reduction in the nonlinear heat flux, a better comparison would be between the reduction in the quasilinear diffusivity and the real nonlinear thermal diffusivities. The quasilinear diffusivities can be calculated using eq. (1.25). While the absolute value is unreliable, we can estimate the relative reduction in diffusivity due to the flow shear. Taking the data from the simulations in fig. 5.16, putting them into eq. (1.25) to get χ^{QL} and dividing by the quasilinear diffusivity for the static case, χ_{static}^{QL} , gives us fig. 6.12⁵. Figure 6.12 shows the reduction in the quasilinear diffusivities as a function of $k_{\theta}\rho_i$ alongside the flux-surface average nonlinear thermal diffusivities.

The second feature of the linear simulations was that there was a shift of the peak growth rate to longer wavelengths with increasing flow shear due to the dependence of the stabilisation on $k_{\theta}\rho_i$. Figure 6.9 shows that during the early linear phase, this phenomenon is still present. Due to the asymmetry with respect to the flow shear direction (see sections 5.3 to 5.6), counter-current rotation (positive shearing rates) have a larger effect on the linear physics than co-current rotation

⁵N.B. Strictly speaking, the important step size for the radial flux is the radial wavenumber, whereas we have used the poloidal wavenumber here. However, as there is a simple relation between k_r and k_{θ} (eq. (5.8)), this drops out in the ratio $\chi^{QL}/\chi_{static}^{QL}$.

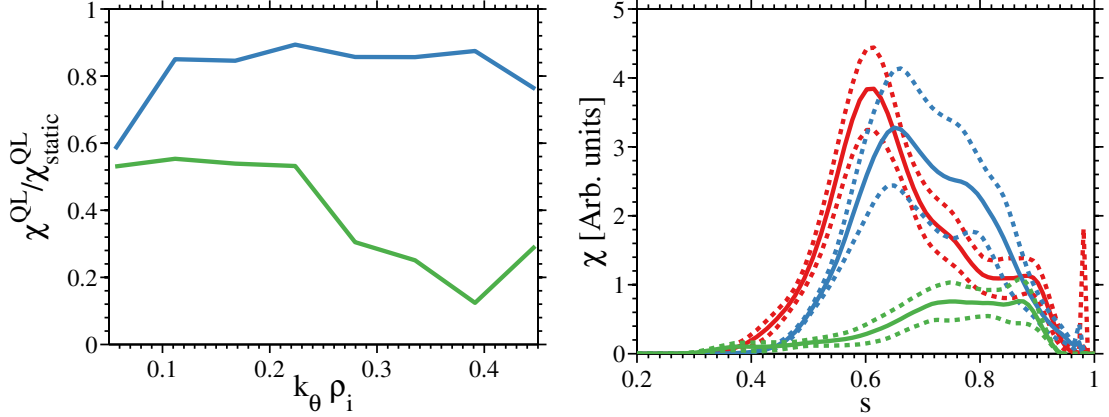


Figure 6.12: Comparison between quasilinear diffusivities estimated from linear simulations and the full nonlinear thermal diffusivities. Left: Reduction in the quasilinear diffusivities due to rotation in the co-current (blue) and counter-current (green) directions. Right: Flux surface average nonlinear thermal diffusivities, averaged over late times for the static (red), co-rotation (blue) and counter-rotation (green). Solid lines are mean values, dashed lines are the standard deviation.

(negative shearing rates) for the same magnitude of γ_E . However, during the course of nonlinear simulations, even without rotation, there is a shift of the mode energy to long wavelengths, due to the nonlinear coupling. This effect appears to dominate over the flow-dependent effect at late linear phase times. After saturation, the mode with the largest amount of energy is the $n = 0$ mode. Excluding the zonal flow, modes around $k_\theta \rho_i = 0.1$ have the most energy in all three cases. This can be seen in fig. 6.13. Given the noise in these data, even after time averaging, it is difficult to discern a difference in peak energy. Again, this is because of coupling between modes. It may be able to see if there is a difference in the turbulence spectra using the BES diagnostic - see section 6.5.2.

Figure 6.13 illustrates the nonlinear cascade of energy into all scales. A full discussion of the nonlinear cascade is beyond the scope of this thesis[90, 91, 92], but a brief summary follows. Energy is injected into certain scales by the microinstabilities (ITG/TEM in this case) which are nonlinearly coupled to adjacent scales. This allows energy to “cascade” down into the smallest scales, $(k_\perp \rho_i)_c$, where some form of dissipation turns the turbulent energy into heat. Physically, collisions are responsible for this dissipation[93], but this can be achieved numerically by various means in the absence of collisions. For example, in collisionless NEMORB simulations, the dissipation is provided by the finite size of the potential grid[55]. There is also an “inverse cascade” which allows energy to move into the larger scales, up to the size of the system, otherwise known as the outer scale, $(k_\perp \rho_i)_o$. Between these

two extremes lies the so-called inertial range, over which energy is transported to different scales. The energy spectrum $E(k)$ over the inertial range is often assumed to be a power law of the form

$$E(k) \propto k^{-p}, \quad (6.6)$$

where p is some power which depends on the exact characteristics of the turbulence in question. By fitting a power law to the energy spectra of the three cases studied here, we find that $p = 3 \pm 0.2$, averaged over all three cases (with the uncertainty coming from the average, rather than the fit). Recent theoretical results propose a division of the inertial range into two further power law regimes with different exponents [91, 92]. The predicted exponents are $-7/3$ between the outer scale and $k_{\perp}\rho_i \sim 1$ and $-10/3$ between $k_{\perp}\rho_i \sim 1$ and $(k_{\perp}\rho_i)_c$. We find that the energy spectra presented here match these predictions, with the only differences being in the ranges of these regimes. In the range $k_{\theta}\rho_i = 0.13 - 0.21$, we find $p = 2.3 \pm 0.4$ (cf. $7/3 = 2.\bar{3}$), and $p = 0.34 \pm 0.13$ (cf. $10/3 = 3.\bar{3}$) between $k_{\theta}\rho_i = 0.21 - 0.45$ (again, these results are averaged over all three cases, with the uncertainties coming from the averaging). There are two slight differences between our results and those in [91]: the first is that we show the energy spectra of $k_{\theta}\rho_i$ rather than $k_{\perp}\rho_i$; the second is that our definition of energy is essentially $n|\phi|^2$ (with n the toroidal mode number), whereas that in [91] is $k_{\perp}\rho_i|\phi|^2$. As we will show later in section 6.5.2 (specifically fig. 6.20), there is significant anisotropy in the perpendicular plane, with $k_r\rho_i > k_{\theta}\rho_i$. We expect, then, that $k_{\perp}\rho_i > k_{\theta}\rho_i$ also, with the result that the x -axis of fig. 6.13 will be shifted towards higher k such that the transition between the two regimes discussed above will be closer to $k_{\perp}\rho_i = 1$. A new diagnostic that measures $k_{\perp}\rho_i|\phi|^2$ as a function of $k_{\perp}\rho_i$ is required to verify this.

6.4.1 Counter-rotation

The heat flux trace, fig. 6.14, for the counter-rotation case is quite different to those of the static and co-rotation cases. There is a large overshoot, with a peak heat flux almost thrice as large as the static case, before the heat flux dies away almost altogether, while it stays at some roughly constant level with zero and co-rotation. The SNR tells a similar story. After the overshoot, the SNR for the counter-flow case quickly drops below 10, while the co-flow simulation takes several thousand more time steps to reach the same level. The decreasing heat flux means that data for this case plotted in fig. 6.10 depend significantly on where the time averaging windows are placed.

Doubling the number of markers to 200M improves the simulation only

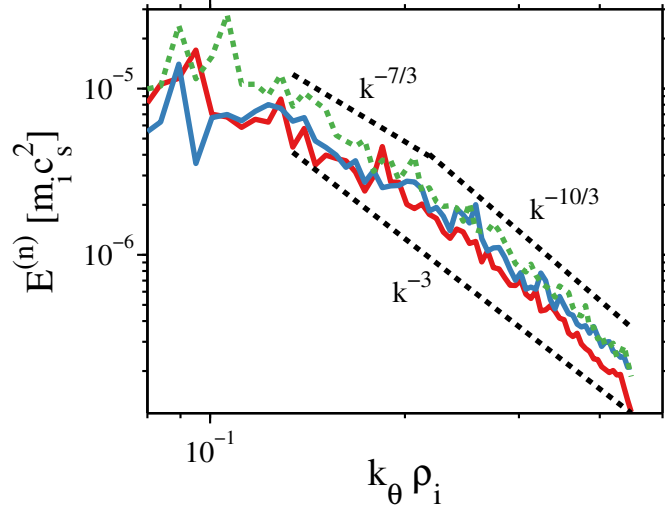


Figure 6.13: Energy versus $k_\theta \rho_i$ for the static (red), co-rotation (blue), and counter-rotation (green) cases. A power-law fit with exponent -3 is also plotted (black, dashed).

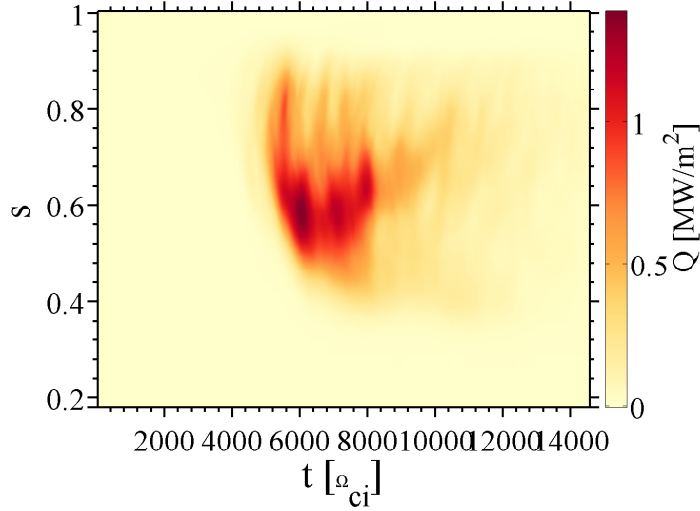


Figure 6.14: Heat flux from a simulation including counter-rotation. After a large overshoot ($t = 5 \times 10^3 \rightarrow 8 \times 10^3 \Omega_{ci}$), the heat flux dies away rapidly.

marginally (factor of $\sqrt{2}$), and doubling again seems to offer no further improvement. This raises the question of whether the decaying heat flux from the counter-rotation is a physical phenomenon or purely numerical. If the flow shear is really suppressing the turbulence, there should be little signal, which would account for the low SNR. Increasing the number of markers should do little to boost that (and indeed,

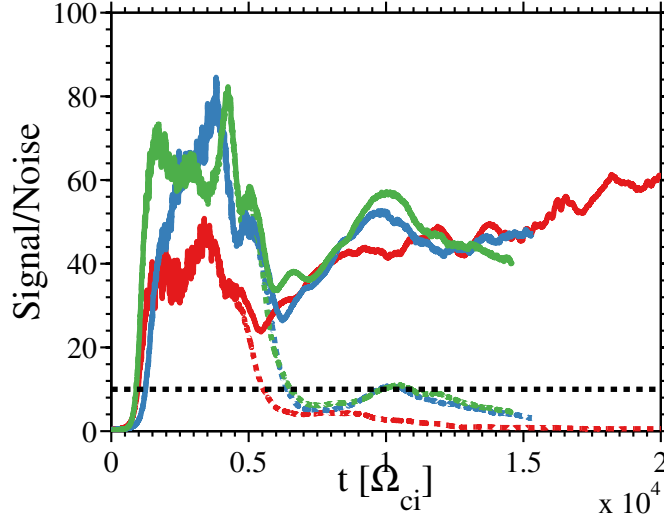


Figure 6.15: SNR for counter-current rotation with increasing number of markers, 100M (red), 200M (blue) and 400M (green), for the total SNR (solid lines) and with the zonal component removed (dashed lines). While the SNR does improve from 100M to 200M particles, there appears to be no gains above that.

we find this to be the case). While the low SNR does raise questions about the fidelity of the simulations, it seems unavoidable for simulations with completely or almost completely suppressed turbulence. Additionally, the large overshoot may be too much for the heating - the turbulence may flatten the profiles, reducing its drive thereby inhibiting itself. We increased the heating from $\gamma_H = 8 \times 10^{-4} \Omega_{ci}$ to $\gamma_H = 1.6 \times 10^{-3} \Omega_{ci}$. This helps keep the profiles close to their initial state (see fig. 6.16), but does not significantly alter the heat flux at later times, suggesting some other mechanism is responsible for the turbulence suppression.

One way to answer the question of whether this is a physical or numerical effect would be to start a simulation with no flow, and let it evolve to its nonlinear saturated turbulent state. The simulation can then be paused and restarted with the counter-current flow. However, this is not currently possible with the code in its present state, as the simulation becomes numerically unstable. This is likely due to the part of the flow in the distribution function. Changing the rotation mid-simulation results in a discontinuous change in the distribution function.

Based on the reduction in quasilinear diffusivities in fig. 6.12, the nonlinear state should still be unstable. A possible explanation for the turbulence in the counter-flow simulation being almost completely suppressed is an upshift in the R/L_T threshold for nonlinear simulations, compared with the threshold for linear runs. This so-called Dimits shift[62, 94] arises from the interaction of the zonal

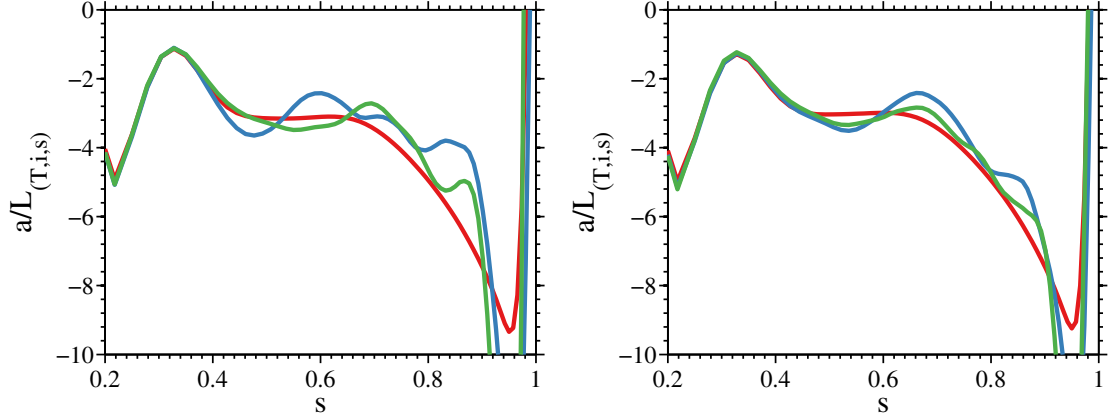


Figure 6.16: Temperature gradient profile at three times during the counter-flow simulations for two different heating rates: initial profile (red); $6000 \Omega_{ci}^{-1}$ (blue); $12000 \Omega_{ci}^{-1}$ (green). Left: $\gamma_H = 8 \times 10^{-4} \Omega_{ci}$. Right: $\gamma_H = 1.6 \times 10^{-3} \Omega_{ci}$.

flows and the turbulence. Close to the linear threshold, $R/L_{T,crit}$, the self-generated zonal flows are strong enough to completely quench the turbulence through the $E \times B$ shear[36]. As R/L_T increases, the “primary” ITG instability becomes stronger and stronger, and we might expect the linearly undamped zonal flows (the “secondary” instability) to build up until they suppress the turbulence. However, at some certain amplitude, the zonal flows themselves start to generate “tertiary” instabilities, limiting their size, with the effect that the heat flux can then increase beyond this point. The result of this is an increase in the value of R/L_T needed for nonlinear simulations to become unstable, and so, although a given linear mode may be unstable at some R/L_T , the nonlinear simulation may in fact be stable. The magnitude of the Dimits shift cannot be known *a priori*, as it relies on knowledge of the saturated state of nonlinear processes, and therefore remains an empirical observation[95].

The Dimits shift could be found for the MAST discharge presented here by performing a scan in R/L_T , however this was prevented by a lack of time. Instead, a scan of flow magnitude was performed, the results of which can be seen in fig. 6.17. The counter-current rotation profile was scaled down by multiplying the whole, original (that is, the co-current) rotation profile by -0.5 and -0.75 - hereafter, we refer to these cases as “half-counter” and “three-quarters-counter” rotation. The thermal diffusivities arising from these cases can be seen in fig. 6.17. The half-counter-flow has a peak χ_i similar to the co-rotation case, although the heat flux is confined to a smaller radial region, with the result that the overall heat flux is smaller in the half-counter case. The three-quarters-counter rotation simulation has a thermal diffusivity between the half-counter- and full-counter-flow cases. This

decrease in peak heat flux with increasing (counter-) flow magnitude, and its shift towards larger s , are a good indication that the turbulence really is suppressed more strongly by counter-rotation than by co-rotation. Unfortunately, these simulations too suffer from poor SNR, making the diagnostics uncertain at best.

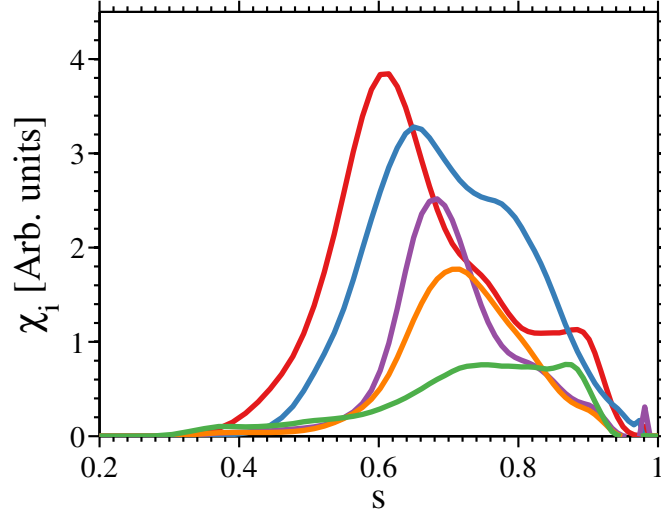


Figure 6.17: Flux surface average nonlinear thermal diffusivities with the inclusion of more rotation magnitudes, averaged over late times for the static (red), co-rotation (blue), counter-rotation (green), half-counter-rotation (purple) and three-quarters-counter-rotation (orange).

6.5 Comparison with experiment

To compare between simulations and experiments requires careful thought. In our models we can measure quantities to arbitrary precision and resolution, and even some physical quantities which are not possible to measure in tokamaks at all, e.g. the electrostatic potential in the core. Real diagnostic instruments have various physical effects which will affect the quality of the signal. Limited resolution, spatially or temporally, may have averaging effects, for instance. Limited bandwidth may destroy or remove information about particular frequencies. Therefore, the best way to compare a simulation to experiment is by forward modelling, i.e. by creating synthetic diagnostics. Synthetic diagnostics work by using a numerical model of the averaging effects, bandwidths, instrument noise, etc. of the physical diagnostic to produce a set of data from the simulated results which can be treated and analysed with the same tools as data from the real machine. Synthetic diagnostics are used elsewhere, for example, in Bayesian analysis to compute consistent plasma states

Optical throughput (étendue)	$1.1 \times 10^{-6} \text{ m}^2 \text{ sr}$
Detector area	$1.6 \times 1.6 \text{ mm}^2$
Magnification	8.7
Channel separation	2 cm

Table 6.2: BES parameters

given multiple diagnostic inputs[96].

6.5.1 BES system

In section 3.4.2, we discussed some of the difficulties in diagnosing turbulence, and the means of measuring it. Beam emission spectroscopy (BES) systems are in place and routinely used on only a few fusion devices - DIII-D, most notably[39]. BES diagnostics work by looking at the D_α ⁶ light from atoms in the heating beam (NBI), which has an energy of 60 – 70 keV. These neutral atoms are excited by collisions with the plasma ions, meaning that not only is the intensity of the light proportional to the neutral density in the beam, but fluctuations in the intensity are proportional to electron density fluctuations[39]. Despite the broadness of the NBI beam (10-20 cm), the spatial resolution of the BES device is much better than this, roughly 2-3 cm. This is because it exploits the very nature of turbulence. By viewing the heating beam along the field lines, the BES system takes advantage of the propensity of the fluctuations to align themselves correspondingly. Analogously, one can think of looking up a ruffled curtain, along its folds. This spatial resolution is good enough to detect ion scale turbulence with $k_\theta \rho_i < 1$. The direct-coupled collection optics have a high étendu which gives the system an SNR of ~300, allowing the detection of density fluctuations of the order of 0.1%. Additionally, the sampling rate of the sensors is 2 MHz, fast enough to fully capture the time dynamics of ITG turbulence, which are of the order of 100 kHz. The main parameters of the BES system are summarised in table 6.2. For a more detailed look at the BES system, please see: [77, 97, 98].

Synthetic diagnostic

The details of the synthetic diagnostic can be found in [97]. In order to construct a synthetic diagnostic, the physical properties of the device’s detection mechanism must be taken into account. For the BES system, this means the physical properties of the heating beam, such as its attenuation, size and shape; the half-life of the D_α

⁶Radiation emitted by an electronic transition of deuterium atoms

emission; and the curvature of the magnetic-field line and the line of sight of the BES system along the field line. From this information, as well as assumptions about the nature of the turbulence, point-spread functions (PSF) can be constructed. The PSF can then be applied to synthetic data (along with shot and signal noise) to generate signals equivalent to those produced by the real diagnostic. Because the PSF contains information about the spatial smearing of the signal due to the line-of-sight along the field-lines and the finite lifetime of the D_α (approximately 3 – 10 ns at a plasma density of $\sim 10^{19} \text{ m}^{-3}$), the synthetic diagnostic only needs 2D density data.

The synthetic diagnostic makes use of the highly elongated nature of tokamak turbulence. Normally, the BES samples the light along its entire line of sight. However, because the width of the heating beam is much shorter than the parallel correlation length of the turbulence, only that small volume of plasma which intersects the beam is actually sampled. The finite width of the beam will, nonetheless, contribute to spatial smearing of the signal.

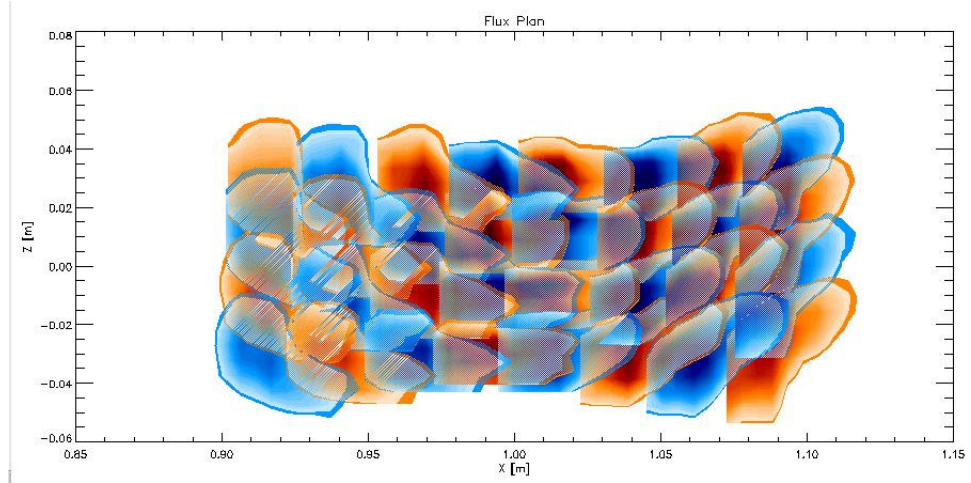


Figure 6.18: The point-spread functions of the detectors cause a "smearing" of the signal. Figure from Y.-c. Ghim, used with permission.

The synthetic diagnostic takes 2D electron density fluctuation data from simulations as its input, i.e. $\delta n_e/n_e(R, Z)$. While there is not currently a diagnostic in NEMORB which produces this data, it is possible to reconstruct density fluctuations from the perturbed potential, which is output in 2D. To do this, the electrons are assumed to have the Boltzmann response to the potential, that is the density is related to the potential through eqs. (2.75) and (2.77). To this end, the flux-surface average of the perturbed potential is removed from the potential before being converted to density fluctuations. Note that this method is not strictly valid,

as the electrons included kinetic effects from the trapped population, and so will not respond adiabatically to the potential. A true 3D diagnostic is currently in development; future work could use this diagnostic instead to take 2D slices of the density.

The only requirement on the spatial resolution of the simulation data is that it is finer than the spatial resolution of the BES itself. The time resolution must be the same, however. Time steps in NEMORB are normalised to the proton cyclotron period at mid-radius. Knowing this, and the physical parameters of the particular MAST discharge, it is trivial to output potential fluctuations with the right temporal resolution.

After obtaining a spatiotemporally varying 2D density, the photon flux, Γ_{ij} , for each detector, i, j , is calculated from the PSFs, $X_{ij}(R, Z)$ using the following formula[99]:

$$\Gamma_{ij} = \iint X_{ij}(R, Z) n_{e0}(R, Z) \left[1 + \beta \frac{\delta n_e(R, Z)}{n_e(R, Z)} \right] dR dZ, \quad (6.7)$$

where $\beta \simeq 0.3 - 0.6$ is a density dependent term, calculated from a collisional radiative model. From the photon flux, the number of photons per sample is further calculated, before shot noise is added. The end result is a series of signals that can be analysed consistently with the experimental data.

Analysis of BES data

Due to low-frequency MHD activity in MAST discharges, the experimental BES data has to be filtered with a band-pass between $f = 10 - 1000$ kHz. Therefore, the synthetic data should also be filtered in the same fashion, despite none of the simulations evolving the magnetic field, and therefore containing no MHD activity. However, the static simulation *does* have low-frequency fluctuations due to the turbulence (and should therefore not use the same filter). This is because the real plasma is rotating, which Doppler shifts the frequencies above the MHD modes. This is also the case for the simulations with rotation. This is neatly illustrated in fig. 6.19, where the static case appears to have much smaller fluctuations than the co-flow case if the same band-pass filter is applied to both. Without the filter, we are able to see more of the fluctuations in the non-rotating simulation.

After filtering, the data are analysed using cross-correlations, a standard technique in statistical analysis of spatiotemporally varying signals[100]. The cross-correlation of two functions of some parameter τ , $f(\tau), g(\tau)$, is essentially the con-

volution of the two functions[101]:

$$(f \star g)(t) \equiv \lim_{T \rightarrow \infty} \frac{1}{T} \int_{-T/2}^{T/2} f(\tau)g(t + \tau)d\tau, \quad (6.8)$$

where t is the lag between the two signals. Here we have assumed that the time-averages of $f(\tau)$ and $g(\tau)$ are zero. A non-zero mean can be removed before the cross-correlation analysis. By integrating over the lag, patterns in otherwise noisy data can be uncovered.

The cross-correlation functions are taken between the signals from the channels at one radial location. The auto-correlation ⁷ is necessarily unity at $\tau = 0$, while the peak of the cross-correlation will be shifted for the poloidally separated channels. The decay in the peak of the cross-correlations gives the lifetimes of eddies (that is, correlation times). The correlation times are calculated by fitting an exponential through the peaks of the cross-correlation function in successive poloidally separated channels, as follows:

$$H(\tau) = A_0 \exp\left(-\frac{\tau}{\tau_{corr}}\right), \quad (6.9)$$

where $H(\tau)$ is the peak of the cross-correlation functions across all channels, A_0 is the peak value of the cross-correlation, and τ_{corr} is the correlation time.

A spatial cross-correlation function can also be produced. This is similar in form to eq. (6.8), except that the temporal lag is replaced with a spatial separation. That is, the temporal lag is zero, and the signals are compared between spatially separated channels (either radially or poloidally). The width of this spatial correlation function then gives the correlation length in that direction.

6.5.2 Results

The fluctuation amplitudes in the simulations are much larger than experiments by a factor of approximately 2 at $s = 0.6$. Including flow does decrease the fluctuation amplitude by 10 – 20% in the core region ($s = 0.4 - 0.7$), but increases it outside of this by the same amount. Figure 6.19 shows the effects of the band-pass filter. Filtering from 10 kHz upwards cuts out a lot of the signal from the static case. The results from outside of $s = 0.9$ should be ignored in the following graphs (figs. 6.19 to 6.21), as the shielding in the edge damps the density fluctuations there.

The mean perpendicular wavenumber on each flux surface, fig. 6.20, helps

⁷The cross-correlation of f with itself, that is $f \star f$.

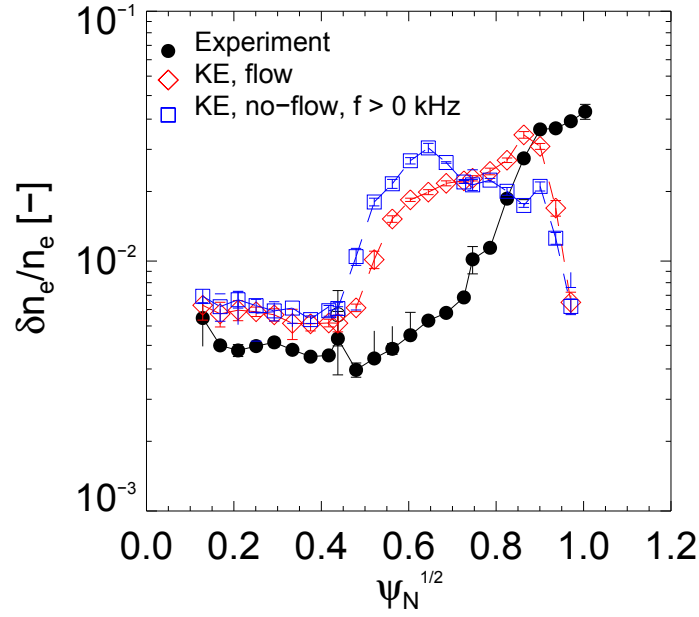


Figure 6.19: Comparison of amplitude of density fluctuations as a function of radius for simulations with (red diamonds) and without (blue squares) flow against experiment (black circles). The experimental levels are $\sim 40\%$ smaller than those predicted from simulation.

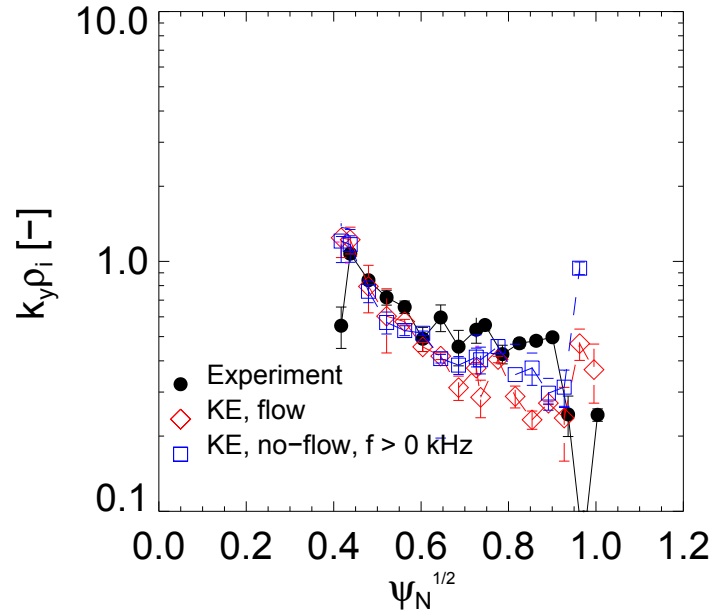


Figure 6.20: Peak perpendicular wavenumber as a function of radius for the experiment (black) and simulations with (red) and without (blue) flow.

us answer the question asked in section 6.4 - does the turbulence move to longer wavelengths? This appears to be the case for the poloidal wavenumber inside of $s = 0.7$, where it moves from $k_\theta \rho_i = 0.3$ to $k_\theta \rho_i = 0.2$ around $s \sim 0.6$, but there is no change outside of this. This is much larger than the shift in the linear simulations, which has a shift between the static and co-flow case of $\Delta k_\theta \rho_i \sim 0.03$ (though the counter-flow does move to $k_\theta \rho_i \sim 0.2$). Interestingly, the radial wavenumbers have a comparable shift in the opposite direction, shifting to shorter wavelengths ($k_r \rho_i = 0.2$ to $k_r \rho_i = 0.1$) in the same location, with little movement outside of $s = 0.7$. The most likely explanation for this is the tilting in the poloidal plane of the eddies by the sheared flow, which reduces their radial extent, increasing the radial wavenumber. This can be seen in the simulations in fig. 5.12.

In contrast to the simulations, the experiment has higher poloidal wavenumbers of $k_\theta \rho_i \sim 0.5 - 1$. The radial wavenumbers of the simulation with flow do, however, agree with experiment.

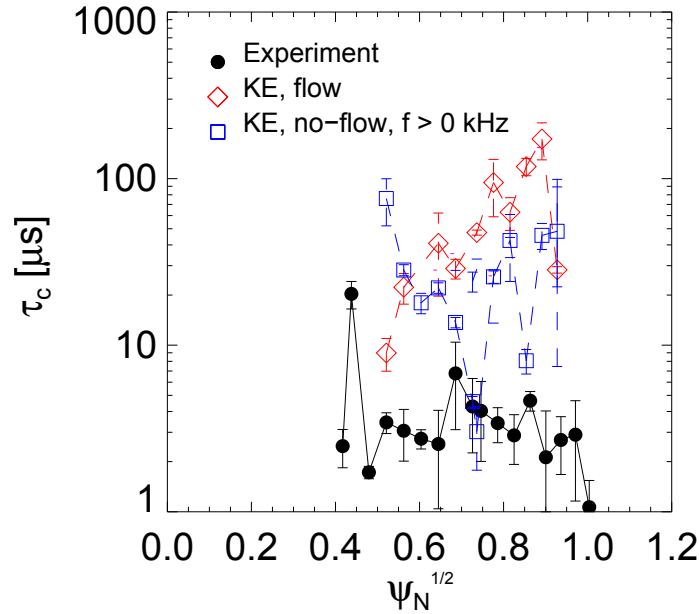


Figure 6.21: Correlation times as a function of radius. The turbulence observed in the experiment is more intermittent than that in the simulations, with correlation times one to three orders of magnitude longer in the latter.

Figure 6.21 depicts the correlation times of the simulations and experiment. It is immediately obvious that the correlation times in the simulations are a long way from the experiment values - by one to three orders of magnitude. Including the toroidal rotation dramatically increases the correlation times by around an order of magnitude. The experimental turbulence is much more intermittent than in the

simulations, which has long-lived structures. Video clips of the synthetic and real BES data make the differences immediately obvious - the simulated turbulence has slowly-varying poloidally elongated structures, while the experimental turbulence has short, more intermittent eddies.

6.6 Conclusions

The results presented in this Chapter suggest that there are other effects playing a role here, i.e. that the turbulence in MAST shot #22807 is most likely not due to collisionless electrostatic ITG/TEM. According to [102], in addition to the effects of trapped electrons, profile variation (that is, finite ρ_* effects), and sheared $E \times B$ flows, electromagnetic fluctuations and collisions are needed in order to get agreement between their simulations and the DII-D discharge under investigation. However, linear simulations using GS2 indicate that electromagnetic effects do not play a strong role for ITG-scale microinstabilities[16] (that is, $k_\theta \rho_i < 1$) in L-mode shots, such as the one studied in this thesis. Also, while it is possible that smaller-scale microinstabilities (such as electron temperature gradient (ETG) modes, which have $k_\theta \rho_i > 1$), are important in this shot, simultaneously simulating both ITG and ETG is beyond the current capability of NEMORB. Moreover, the limited resolution of the BES system means that it cannot detect ETG-scale turbulence, and so they cannot be responsible for differences between the NEMORB simulations presented here and the experimental results.

GS2 simulations demonstrate that collisions lower the growth rates of the ITG/TEM by a significant amount[15] - the effect is approximately the same magnitude as that from including co-current rotation. Therefore, the inclusion of collisions is a strong candidate for the reconciliation of simulation and experiment.

Chapter 7

The role of collisions on ITG/TEMs in MAST

One of the major pieces of physics missing from the simulations in the previous Chapter is collisions. Simulations performed using the local code GS2 show that the effects of collisions do significantly reduce the linear growth rates[15], by 20 – 40%. The addition of collisions to the gyrokinetic framework is a problem of subtle complexity. Superficially, the effects of collisions appear to be included purely by adding the collision operator, C , to the right-hand side of eq. (2.1). However, C hides a multitude of sins. While the exact form of the collision operator is known[103], it is (computationally) prohibitively expensive, and so some form of model operator must be used instead. The model collision operator must satisfy a set of criteria, such as conservation of mass, energy and momentum. It must also vanish when applied to a Maxwellian, which is the correct equilibrium state. A full set of considerations and criteria can be found in [93].

7.1 Implementation

Collisions are tricky to implement in PIC codes, and inevitably lead to increased noise. The implementation of collisions into NEMORB is detailed in [13]; the main details will be summarised here. The ion collision frequency, ν_{ii} , is smaller than the electron collision frequency, ν_{ee} , by a factor of the square of the mass ratio. Because of this, we neglect ion collisions, and include only electron-electron and electron-ion collisions.

While the gyrokinetic equations include FLR effects, they have been neglected in the collision operators. This approximation is thus strictly valid for the

regime $k_\theta \rho_i \ll 1$. Since we consider $k_\theta \rho_i < 1$, it is reasonably suitable for the cases studied in this thesis. We also assume weak collisionality, which is justified for the MAST device, as it is firmly in the banana regime (see section 1.3.1). The collision operator has been linearised with respect to a local Maxwellian, F_{LM} (that is, $\psi_0 = \psi$, the poloidal flux, in eq. (2.62)). This approximation is justified for small δf_{LM} , which must be true in the gyrokinetic framework.

The electron-ion and electron-electron collisions are handled differently. Electron-ion collisions make use of the small mass ratio approximation and assumes that the ions are immobile in the laboratory frame. Starting with the electron-ion collision operator, $C_{ei}[F_i, F_e]$, and using $F_e = F_{LM,e} + \delta f_{LM,e}$, we first note that the collision operator vanishes when applied to a Maxwellian velocity distribution function, therefore we only have to consider $C_{ei}[F_i, \delta f_{LM,e}]$. $C_{ei}[F_i, F_e]$ is modelled using the Lorentz operator,

$$\hat{L}^2 = - \left[(1 - \xi^2) \frac{\partial}{\partial \xi} + \frac{1}{1 - \xi^2} \frac{\partial^2}{\partial \alpha^2} \right], \quad (7.1)$$

and can be shown to reduce to:

$$C_{ei}[F_i, \delta f_{LM,e}] = -\nu_{ei}(v) \frac{\partial}{\partial \xi} \left[(1 - \xi^2) \frac{\partial \delta f_{LM,e}}{\partial \xi} \right], \quad (7.2)$$

where $\xi = v_\parallel/v$ is the pitch-angle, and the electron-ion collision frequency $\nu_{ei}(v)$ is given by

$$\nu_{ei}(v) = \bar{\nu}_{ei} \left(\frac{v_{th,e}}{v} \right)^3, \quad (7.3)$$

$$\bar{\nu}_{ei} = \frac{n_i Z^2 e^4 \ln \Lambda}{8\pi \epsilon_0^2 m_e^2 v_{th,e}^3}. \quad (7.4)$$

The Coulomb logarithm $\ln \Lambda$ is assumed to be constant throughout the plasma and $\simeq 13$.

The self-collisions operator is split into four terms by linearisation:

$$C[F, F] = C[F_{LM}, F_{LM}] + C[F_{LM}, \delta f_{LM}] + C[\delta f_{LM}, F_{LM}] + C[\delta f_{LM}, \delta f_{LM}], \quad (7.5)$$

where the first term is zero as the local Maxwellian is a stationary state of the collision operator, and the last term is neglected due to linearisation. The second term is the effect of collisions from the perturbed distribution function on the background function and is comprised of a drag and a diffusion term. This can be further

decomposed into a pitch-angle scattering term and a thermalisation term:

$$C[F_{LM}, \delta f_{LM}] = \frac{1}{2} \nu_D(v) \hat{L}^2 \delta f_{LM} - \frac{1}{v^2} \frac{\partial}{\partial v} \left[\frac{1}{2} v^4 \nu_{\parallel}(v) F_{LM} \frac{\partial}{\partial v} \left(\frac{\delta f_{LM}}{F_{LM}} \right) \right], \quad (7.6)$$

where $\nu_D(v), \nu_{\parallel}(v)$ are the pitch-angle and thermalisation frequencies, respectively. The third term, $C[\delta f_{LM}, F_{LM}]$, is the background reaction term and is designed to ensure that mass, momentum and kinetic energy are all conserved. The real term, derived from the Landau operator, requires derivatives of δf_{LM} , operations that introduce large amounts of noise into the simulation. Therefore, an approximate form is used:

$$C[\delta f_{LM}, F_{LM}] \simeq F_{LM} \mathcal{B}(\delta f_{LM}), \quad (7.7)$$

$$= \frac{F_{LM}}{n(\mathbf{X})} \left\{ 6\sqrt{\pi} H(\bar{v}) \frac{\delta \mathcal{P}_{\parallel} v_{\parallel}}{v_{th}^2} + \sqrt{\pi} G(\bar{v}) \frac{\delta \mathcal{E}}{v_{th}^2} \right\}, \quad (7.8)$$

where $\bar{v} = v/v_{th}$, the functions H and G are related to the Rosenbluth potentials (defined in [13]), and $\delta \mathcal{P}_{\parallel}$ and $\delta \mathcal{E}$ are the changes in the parallel momentum and kinetic energy, respectively, of the perturbed distribution function due to $C[F_{LM}, \delta f_{LM}]$. For details of the numerical implementation of this collisional scheme, please see [13].

7.2 Linear studies

We now perform a scan in $k_{\theta} \rho_i$ with linear simulations including the effects of collisions, using the experimental collision frequency of $\nu_{ei} = 4 \times 10^{-3} \Omega_{ci}$, the results of which are summarised in fig. 7.1. As expected, the collisions reduce the linear growth rates, by an average of 29% over the range $k_{\theta} \rho_i = 0.15 - 0.45$, comparable to that found by GS2, with a mean 44% reduction over $k_{\theta} \rho_i = 0.15 - 0.51$. Given that this damping of the linear growth rates is similar to the collisionless case with co-current rotation, we may expect the full nonlinear simulations to also be close. However, the collisions may interact with, for example, the zonal flows differently. Indeed, ion-ion collisions are known to enhance the damping of the zonal flow [36], which can lead to an increased heat flux.

The next step is to include rotation as well as collisions. The same rotation profiles as used in chapter 6 were used here. Figure 7.2 shows the effects of including rotation into collisional simulations on the linear growth rates. As with the collisionless case, counter-flow rotation is more stabilising than co-flow. Compared with the collisionless simulations, rotation in either direction reduces γ by a similar

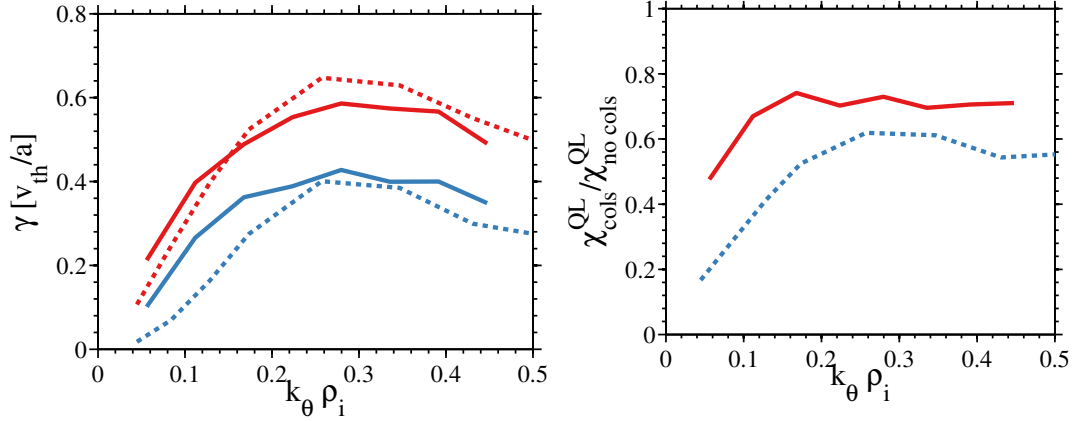


Figure 7.1: Left: Comparison of growth rate with (blue) and without (red) collisions between NEMORB (solid lines) and GS2 (dashed lines). Right: Ratio of collisional quasilinear diffusivity to collisionless quasilinear diffusivity as a function of $k_\theta \rho_i$ for NEMORB (red, solid) and GS2 (blue, dashed).

amount for wavenumbers $k_\theta \rho_i > 0.3$, but acts much more strongly at longer wavelengths, especially for $k_\theta \rho_i < 0.2$, as can be seen in the reduction in the quasilinear diffusivities in fig. 7.2. This is strikingly evident for the counter-flow case, where the modes are almost completely stabilised for the longer wavelengths, $k_\theta \rho_i < 0.3$, with $\gamma < 0.04$ across that whole range. Contrast this with the collisionless counter-flow case, fig. 6.9, which has $\gamma \sim 0.2$ even at $k_\theta \rho_i = 0.1$. Given that they are responsible for a large proportion of the transport, this large stabilisation for the longer wavelengths suggests that collisional nonlinear simulations with rotation are likely to be very close to marginal stability, if not completely suppressed.

7.3 Nonlinear studies

Collisions have a severely detrimental effect on the noise in PIC simulations. It is therefore even more important than the collisionless case to have adequate noise control. As stated above, the coarse graining technique is the only noise control scheme available which is suitable for use with collisions. Even with coarse-graining, collisional simulations require more markers than the equivalent collisionless run, typical a factor three or more. To this end, all the simulations presented in this section have at least 400M markers.

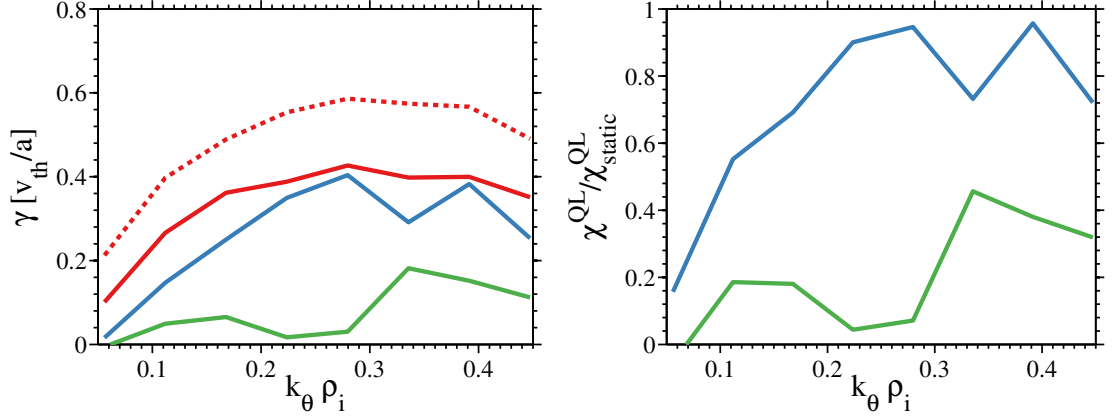


Figure 7.2: Left: Comparison of growth rate with co- (blue) and counter-rotation (green) to the static collisional (red, solid) and collisionless (red, dashed) cases. Right: Ratio of quasilinear diffusivities against $k_{\theta} \rho_i$ for co- (blue) and counter-flow (green).

7.3.1 Coarse-graining

As discussed in section 6.2.1, the coarse-graining noise control scheme requires some input parameters to be tuned manually. The number of bins in energy space were tuned using collisionless simulations in section 6.2.1. The coarse-graining rate, γ_{cg} , however, was tuned using collisional simulations, which require a robust noise control scheme. We scanned γ_{cg} over the range of $0.01 \Omega_{ci}$ down to $0.0001 \Omega_{ci}$. The results are shown in fig. 7.3, which depicts the effects of changing γ_{cg} on the growth rate, γ , measured during the linear phase of nonlinear simulations, and on the SNR of the same simulations. It can be seen immediately from fig. 7.3 that the largest coarse-graining rate affects the linear physics significantly, reducing γ from a peak of $0.45 v_{th}/a$ to $\sim 0.2 v_{th}/a$, while the damping rates smaller than $\gamma_{cg} = 1 \times 10^{-3} \Omega_{ci}$ all converge to the same γ . The best effect on the SNR is from γ_{cg} between $5 \times 10^{-4} \Omega_{ci}$ and $1 \times 10^{-3} \Omega_{ci}$. Figure 7.3 also includes a simulation with shielding and heating (see section 6.2).

7.3.2 Number of markers

Given that a collisional simulation requires several times more markers than a collisionless one, we increased the number of markers from 400M to 1200M. As can be seen in fig. 7.4, the SNR does improve in the late-time by the expected factor of $\sqrt{3}$, but the decaying nature remains, and the SNR drops below 10 after a mere additional 1000 time steps.

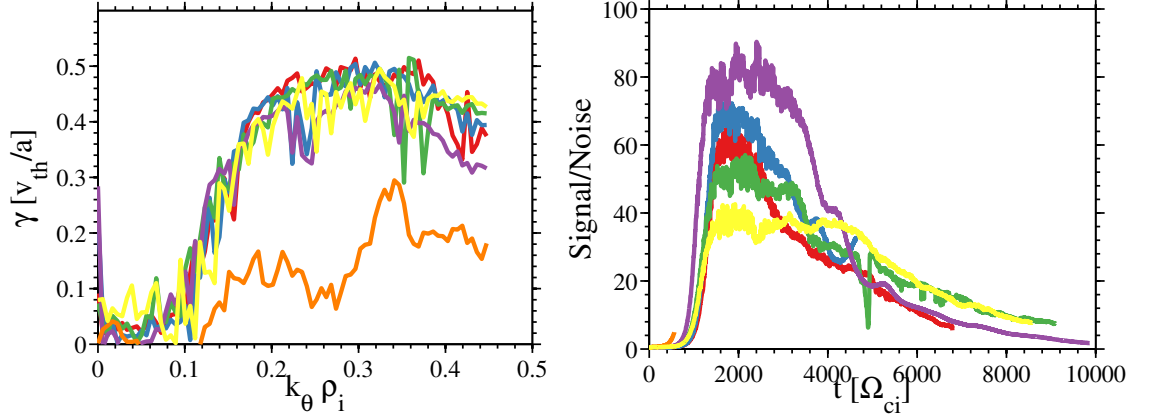


Figure 7.3: The effect of changing the coarse graining rate, γ_{cg} . Left: Growth rate during the linear phase against $k_\theta \rho_i$. Right: Signal to noise ratio. The damping rate was scanned from $1 \times 10^{-4} \Omega_{ci}$ (red), $5 \times 10^{-4} \Omega_{ci}$ (blue), $1 \times 10^{-3} \Omega_{ci}$ (green), $5 \times 10^{-3} \Omega_{ci}$ (purple), $1 \times 10^{-2} \Omega_{ci}$ (orange). A simulation including shielding and heating with $\gamma_{cg} = 5 \times 10^{-4} \Omega_{ci}$ (yellow) is also shown. The simulation with the largest γ_{cg} ($1 \times 10^{-2} \Omega_{ci}$, orange line) was stopped early due to its detrimental effect on the linear physics.

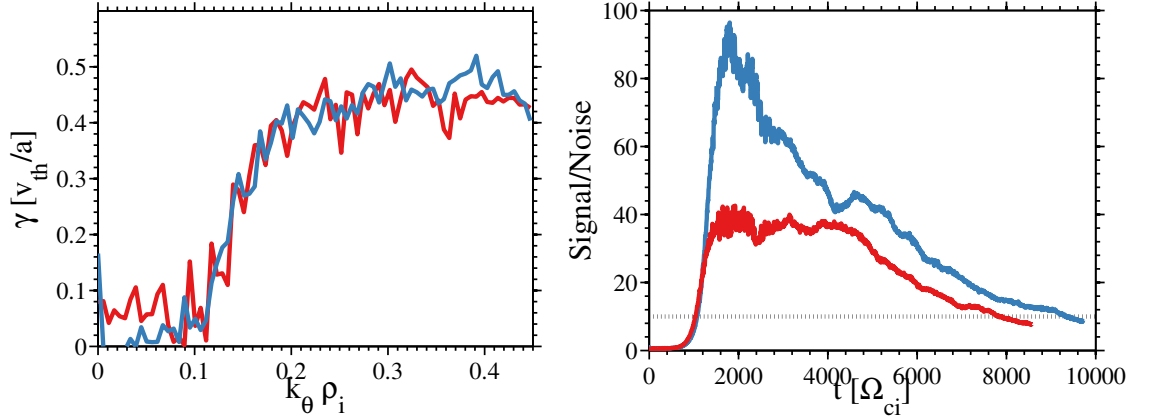


Figure 7.4: Increasing the number of markers from 400M (red) to 1200M (blue). Left: Growth rate against $k_\theta \rho_i$. Right: Signal to noise ratio.

As with the counter-rotating collisionless runs, section 6.4.1, there is an inherent difficulty in distinguishing fully- or largely-suppressed turbulent states and noise-dominated simulations. One factor not considered in the discussion for the former case is that of the electron model. All the nonlinear simulations presented in this thesis have been run using the hybrid kinetic electron model, where the trapped electrons are evolved, but the passing electrons are assumed to be adiabatic. The pitch-angle scattering from the collisions with the ions will likely de-trap a signif-

icant proportion of the trapped population, and at the same time, re-trap part of the passing population. While collisions are compatible with the hybrid model, it is possible that the changing trapped fraction is not being handled correctly. If that is the case, it may be better to use the fully kinetic model - where the entire electron population is loaded and evolved in the same fashion. This, however, has a significant cost associated with it: namely, that the time-step must be reduced by a factor of 4, to half the (proton) cyclotron frequency. The computational expense would increase by an equivalent amount.

7.4 Results

Given the decaying nature of both the SNR, fig. 7.4, and the heat flux, fig. 7.5, it is most likely that with the inclusion of collisions, the turbulence is largely, or completely, suppressed. Similarly to the collisionless counter-rotating case, the decaying heat flux leads to large uncertainties in the late time-averaged heat flux. With that in mind, the heat flux is approximately five times smaller than the collisionless case, and now much closer to the experimental value of $0.01 - 0.05 \text{ MW/m}^2$. This decrease in the heat flux and diffusivity is much larger than expected, given the linear results (fig. 7.1), where the linear growth rates were reduced by an amount similar to the collisionless co-flow case (fig. 6.9). This is similar to the collisionless counter-flow case, which has finite linear growth rates, but near-complete suppression of the turbulence. There is no significant evolution of the equilibrium profiles, ruling out the turbulence flattening the profiles and thereby inhibiting its own drive. Again, a possible explanation is the Dimits shift in the threshold gradient pushing this case closer to marginal stability. As with the collisionless case, a scan of R/L_T would be needed to test this theory.

Unfortunately, the inclusion of both rotation and collisions in the same simulation is currently numerically unstable in the nonlinear regime. There is a branch of the NEMORB code base in development that should rectify this issue, and so future work could, after appropriate testing, perform this last simulation. If we compare the collisionless cases with and without flow, both linear (chapter 5) and nonlinear (chapter 6), we note that the inclusion of sheared toroidal rotation leads only to a moderate reduction in the heat flux (fig. 6.10) and diffusivity (fig. 6.12), a small change in the fluctuation amplitude (fig. 6.19), and rearranging of the spatial spectrum (fig. 6.9 and fig. 6.20). Now, if we compare the linear collisional cases with and without flow, we see a reduction in the linear growth rates of a similar magnitude to the collisionless case (fig. 7.2, cf. fig. 6.9). However, we do see a greater stabilisation

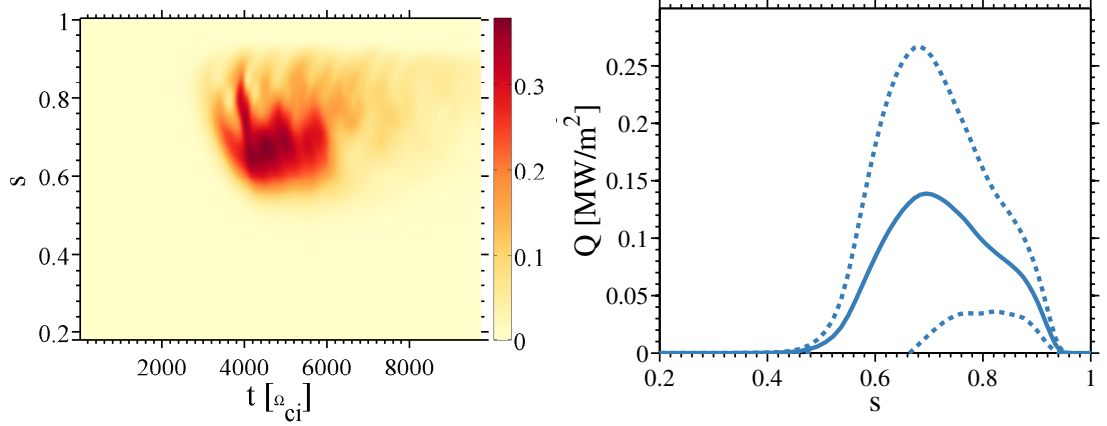


Figure 7.5: Flux-surface average heat flux. Left: As a function of radius and time. Right: Late-time average

of the longer wavelengths than in the collisionless cases. Extrapolating from this, we might predict, then, a somewhat greater change in the nonlinear collisional results with flow shear than the equivalent collisionless cases. This is, however, perhaps compounded somewhat by the Dimits shift, as evidenced by the counter-flow case (see section 6.4.1). An accurate measure of the change in threshold gradient due to the nonlinearity would help the robustness of this prediction.

7.4.1 Comparison to experiment

Going solely from the linear studies, we might expect only a moderate reduction in the fluctuation amplitude with the inclusion of collisions. We actually see a much larger reduction (a decrease of $\delta n_e/n_e$ from 2% in the collisionless static case to $\sim 0.2\%$ for the collisional simulation at $s = 0.6$, compared with $\sim 1\%$ for the collisionless case with flow), and the shape of the profile is now much closer to experiment (see fig. 7.6). Likewise, the poloidal wavenumber is now closer to experiment (see fig. 7.7), with $k_\theta \rho_i$ approximately equal to the experimental values over much of the range $s = 0.4 - 0.8$. There are still significant discrepancies outside of $k_\theta \rho_i = 0.8$ and large uncertainties in the simulated data inside of this radius. In contrast, the correlation times (fig. 7.8) are still approximately an order of magnitude longer than in experiment.

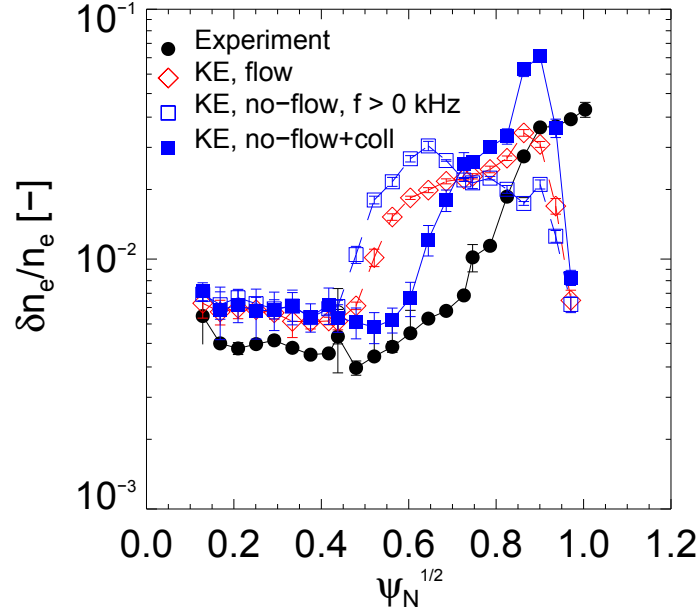


Figure 7.6: Comparison of amplitude of density fluctuations as a function of radius for simulations with (red diamonds) and without (blue squares) flow against experiment (black circles). The simulation including collisions is shown with filled blue squares. The experimental levels are $\sim 40\%$ smaller than those predicted from simulation.

7.5 Conclusion

As we have seen in the previous chapter, collisionless electrostatic simulations do not capture all of the physics present in MAST plasmas. Including the effects of collisions brings the level of ITG activity closer to experiment. The amplitudes of turbulent density fluctuations (fig. 7.6) are now within 40% of the experimental value, compared with collisionless results, which are a factor two out.

However, it is not certain if the collisional simulations are actually well resolved - that is, if the decaying heat flux in late times is due to physical or numerical effects. As with the counter-flow, collisionless case, the simulations end up becoming noise-dominated, with SNRs below 10. They also typically become numerically unstable at this point, resulting in a premature end to the simulation. It is not clear whether this is linked with the decaying heat flux.

A possible reason for the numerical issues with long-running collisional simulations could be the hybrid electron model used. This uses a drift-kinetic model (which neglects FLR effects) for the trapped electrons while still treating the passing electrons adiabatically[79]. Doing so allows one to use a reduced ion/electron mass ratio, which in turn allows larger time steps to be used[104]. However, as collisions

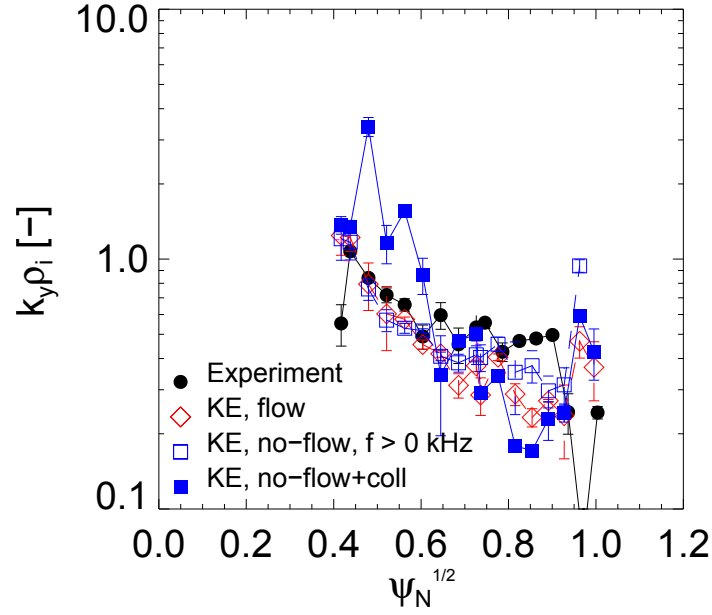


Figure 7.7: Peak poloidal wavenumber as a function of radius. The radial wavenumber is not shown here (cf. fig. 6.20), but the inclusion of collisions does not affect $k_r \rho_i$.

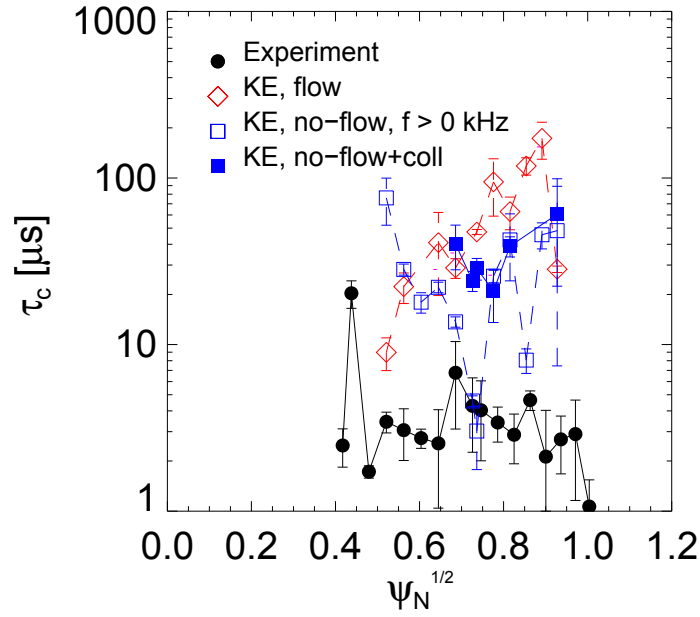


Figure 7.8: Correlation times as a function of radius. The addition of collisions does not significantly change τ_c from the collisionless case - that is, τ_c is still an order of magnitude longer than in experiment.

enhanced the detrapping/retrapping of electrons (that is, cause more electrons to cross the trapped/passing boundary), it is possible that this could adversely impact the simulations. This could be tested by using the fully kinetic model for the electrons, which makes no distinction between the passing and trapped electrons. The rapid parallel motion of the passing electrons then requires a reduction in the time step in order to resolve this motion. Furthermore, the passing electrons causes the appearance of electrostatic Alfvén waves, requiring even smaller time steps. Fully kinetic electrons would necessitate sub-gyroperiod, $\Omega_{ci}^{-1} < 1$, time steps in order to avoid such numerical instabilities. This is a factor four smaller than the time step used in the nonlinear simulations presented in this Chapter, meaning such simulations would be four times more computationally expensive. Therefore, it seems that a simulation with fully kinetic electrons and collisions in MAST geometry is currently at or beyond the limits of our current capability.

Numerical issues also currently prevent the simulation of nonlinear collisional cases with sheared toroidal rotation. Linear simulations are possible, and from these, it seems that flow shear is likely to have a stronger effect on collisional simulations than collisionless ones, as it stabilises longer wavelength modes more in the former case than the latter. The capability to perform these simulations is currently a work in progress by members of the NEMORB development team.

Chapter 8

Conclusion

This thesis investigates the effects of flow shear on ITG and ITG/TEM modes in MAST plasmas, and includes the first comparison of nonlinear turbulence simulations with experiment via a new synthetic diagnostic. In chapter 5, linear simulations investigated how the sign and magnitude of flow shear affects the stabilisation of ITG and ITG/TEM microinstabilities. The asymmetry in the flow shear stabilisation in MAST plasmas arises from global effects, which means that the treatment of profile variation is a necessity for the accurate simulation of spherical tokamaks or devices with large ρ_* .

The consequences of this flow shear asymmetry in nonlinear simulations were studied in chapters 6 and 7. The impact of the asymmetry is even larger for nonlinear simulations than for the linear simulations of chapter 5, strengthening the case for a global treatment of MAST L-mode plasmas. Chapters 6 and 7 also made the first direct comparisons of simulated turbulence with experiment on MAST. This revealed the need for the inclusion of kinetic electrons and collisions in simulations in order to match the experimental observations.

8.1 Summary of key results

Linear simulations with adiabatic electrons including the effects of flow shear in chapter 5 studied the dependence of flow shear stabilisation on the poloidal wavelength of ITG modes. Studies using two different rotation profiles (one using an analytic electric field to drive the $E \times B$ flow; the other using a rotation profile taken from the MAST experiment) in two different equilibria (CYCLONE base case parameters in circular magnetic geometry, and a typical set of experimental profiles for MAST MHD equilibria) found that the ratio of critical $E \times B$ shearing rate to static

growth rate ($\gamma_E^{\text{crit}}/\gamma_0$) varies strongly with $k_\theta \rho_i$ in all cases. The dependence of $\gamma_E^{\text{crit}}/\gamma_0$ on $k_\theta \rho_i$ is weaker for the experimental rotation profile than for the analytic one. The measurement of the geometric structure of the different modes suggests a relationship between $\gamma_E^{\text{crit}}/\gamma_0$ and the size/shape of the mode.

Flow shear stabilisation of ITG/TEM modes in MAST plasmas is asymmetric with respect to the sign of the $E \times B$ shearing rate, γ_E , with the maximum linear growth rate occurring at finite γ_E . For MAST discharge #22807 with the experimental profile, this peak growth rate is produced by negative shearing rates (the same sign as experiment), with a γ_E of 10% that of the experimental value. Positive shearing rates, corresponding to counter-current rotation are more stabilising for this shot. This asymmetry in the sign of γ_E is caused by equilibrium profile variation on length scales comparable to those of the microinstabilities.

While the experimental rotation profile does reduce the linear growth rates of ITG/TEM, the modes are not completely stabilised as in the cases with adiabatic electrons. The flow shear asymmetry is still apparent, with counter-current rotation profile (positive γ_E) stabilising the ITG/TEM more than co-current flow (negative γ_E) by a factor of more than two, though again, the growth rates remain finite. Additionally, the peak of the growth rate spectrum moves to longer wavelengths with negative flow shear.

In chapter 6 nonlinear simulations revealed that the flow shear asymmetry is even stronger than in the linear cases, with the counter-current flow profile almost completely suppressing the turbulence. The exact cause of this increased turbulence suppression over the linear stabilisation is not yet known, but a plausible mechanism does present itself: the Dimits shift. The change in the nonlinear threshold temperature gradient may mean that the counter-flow profile pushes the system close enough to marginal stability that the turbulence is almost completely suppressed by the zonal flows. Scaling the experimental profile in order to scan in the flow shearing rate revealed a steady suppression of the turbulence, suggesting that the asymmetry in nonlinear simulations is a physical effect and not due to numerical issues. The large difference in turbulence levels between the two signs of flow shear means that a global treatment of sheared rotation in tokamaks with a large ρ_* is necessary. Merely changing the sign of the flow shear makes the difference between a 20% reduction in the heat flux and near-complete suppression of the turbulence. At the very least, this would require the inclusion of the effects of profile variation into local codes in order to accurately model flow-shear in these devices.

Chapters 6 and 7 also presented the first direct comparison of simulated turbulence with experimental data from MAST using a synthetic beam emission

spectroscopy (BES) diagnostic. In collisionless simulations with kinetic trapped electrons, sheared toroidal rotation has mixed effects on the turbulence. While it reduces the heat flux, it dramatically increases the turbulence correlation time to around three orders of magnitude longer than the experimental correlation times. The poloidal correlation lengths are also longer in the simulations than experiment, though radially, the correlation lengths do agree quite well. Taken together, the results from this comparison suggest that other effects need to be taken into account in order to simulate MAST L-mode shots. The inclusion of electron-electron and electron-ion collisions in electrostatic simulations brings the turbulent density fluctuation amplitude profile closer to the experimental profile, both in amplitude and shape. Currently, nonlinear simulations with the effects of both collisions and flow shear are numerically unstable, and this is under investigation.

Despite the reasonable agreement between collisional simulations and experiment, one should be fully aware of the limitations of the simulations. The collisional simulations invariably become noise-dominated at late times, with low signal-to-noise ratios (SNR), and often becoming numerically unstable. Complete suppression of the turbulence would produce low signal-to-noise ratios, but collisions also make simulations noisier. An increase in the number of markers, from 400M to 1200M, did not alter the physical results and still lead to a similar noise-dominated end to the simulation. Likewise, tuning of the noise control scheme increased the SNR marginally, without affecting the late-time heat fluxes. These checks increase our confidence that the simulations with collisions really do show a large suppression of the turbulence than in the collisionless case.

8.2 Future work

The simulations with collisions come close to reproducing the experimentally observed turbulence. There are still physics effects not included at present in our these simulations. The first notable one is the lack of toroidal rotation, as nonlinear collisional simulations suffer from numerical instabilities when we include sheared flow. It is possible to perform linear simulations including both effects which suggests that flow shear is likely to have a stronger effect on collisional nonlinear simulations than collisionless ones. Sheared rotation in the former cases stabilises longer wavelengths more effectively than in the latter. We are working on understanding the numerical instability and hope to perform such simulations in the near future. Additionally, the model for rotation used in this thesis is the “low-flow” ordering, where the rotation is assumed to be well below the sonic speed. The flow in the core

of the plasma reaches sonic Mach numbers of around $0.4 - 0.6$, somewhat pushing this assumption. A “strong-flow” ordering model which allows transonic rotations is also under development. There is not enough data presently to say whether the simulations require the strong-flow model.

The effects from electromagnetic fluctuations have been implemented in the code, but they are not suitable for production at this time. Linear simulations with GS2 show that these effects are certainly needed for H-mode shots, but they do not make a significant impact on L-mode discharges. It is not yet known what electromagnetic microinstabilities present in MAST need a global treatment to understand their interaction with sheared toroidal flows.

While the BES diagnostic on MAST is still in its early days, having only been installed on the machine in 2010, it is already proving to be a valuable tool, allowing us to pry into the secrets of ion-scale turbulence. The synthetic version of the BES in NEMORB allows us, for the first time, to directly compare turbulence between simulation and experiment. This will enable us to benchmark codes directly against experiment, rather than other codes, ensuring that theory remains in contact with the experimental data. By allowing us to understand which pieces of physics are necessary to form a model of tokamak turbulence, we can improve the fidelity of simulations and perhaps reduce the dimensionality of our models without sacrificing accuracy. In turn, this could help motivate improving the diagnostic capabilities of the BES. While it suffers from poor spatial resolution, it has excellent temporal resolution. Improvements in simulations derived from matching models to experiment may then let us use the wavenumber/frequency spectra of simulated turbulence to improve the spatial resolution of the real diagnostic by inverting the frequency spectrum from the BES. This synergistic relation between theory, simulation and experiment may finally unlock the secrets of turbulence.

Appendix A

Notation

Here is a list of mathematical symbols commonly used throughout the text of this thesis. This is not an exhaustive list; symbols used only within one or two sections are not defined here.

Symbol	Description
a	Minor radius of last closed flux surface
\mathbf{A}	Magnetic vector potential
\mathbf{b}	Magnetic field unit vector
\mathbf{B}	Magnetic field vector
C	Collision operator
D	Particle diffusivity
e	Electron charge
\mathbf{E}	Electric field vector
F	Distribution function
F_0	Equilibrium part of F
δf	Perturbed part of F
I	Plasma current magnitude
\mathbf{J}	Plasma current vector
k	Mode wavenumber
L_n, L_T	Density and temperature length scales
m	Poloidal mode number/Particle mass
n	Toroidal mode number/Number density
n_i	Ion density
δn	Perturbed ion density
P_{\parallel}	Parallel momentum
q	Safety factor/Particle electric charge

Symbol	Description
Q	Heat flux
r, R	Minor and major radii of plasma
s	Radial coordinate
t	Time
T	Temperature
v	Velocity
v_{\parallel}	Parallel velocity
v_{\perp}	Perpendicular velocity
v_{th}	Thermal velocity
w	Particle weight
\mathbf{x}	Guiding centre position vector
\mathbf{X}	Gyro-centre position vector
z	Guiding centre coordinate system
Z	Gyro-centre coordinate system
α	Gyro-phase
β	Plasma- β
γ	Instability growth rate
γ_E	$E \times B$ shearing rate
Γ	Particle flux
δ	Small parameter
ϵ	Inverse aspect ratio
θ	Geometric poloidal angle
θ_*	Straight-filed line poloidal angle
ρ_i	Larmor radius
ρ_*	Normalised gyroradius
ϕ	Perturbed potential
ψ	Poloidal magnetic flux
χ	Heat diffusivity
Ω_{ci}	Cyclotron frequency

Bibliography

- [1] P. Hill, S. Saarelma, B. McMillan, A. Peeters, and E. Verwichte, *Plasma Physics and Controlled Fusion* **54**, 065011 (2012).
- [2] M. Parry, O. Canziani, J. Palutikof, P. van der Linden, and C. Hanson, editors, *Contribution of Working Group II to the Fourth Assessment Report of the Intergovernmental Panel on Climate Change*, Cambridge University Press, 2007.
- [3] B. Metz, O. Davidson, P. Bosch, R. Dave, and L. Meyer, editors, *Contribution of Working Group III to the Fourth Assessment Report of the Intergovernmental Panel on Climate Change*, 2007.
- [4] A. McCrone, V. S.-O. Eric Usher, U. Moslener, J. G. Andreas, and C. Grüning, *Global Trends in Renewable Energy Investment 2011*, 2011.
- [5] G. Audi, O. Bersillon, and J. Blachot, *Nuclear Physics A* **729**, 3 (2003).
- [6] J. Lawson, *Proc. Phys. Soc. B* **70**, 6 (1957).
- [7] M. Greenwald et al., *Nuclear Fusion* **28**, 2199 (1988).
- [8] K. Miyamoto, *Plasma Physics and Controlled Nuclear Fusion*, Springer, 2004.
- [9] J. A. Wesson, *Tokamaks*, OUP, second edition, 1997.
- [10] D. J. Applegate et al., *Physics of Plasmas* **11**, 5085 (2004).
- [11] A. Sykes et al., *Plasma Physics and Controlled Fusion* **39**, B247 (1997).
- [12] F. J. Casson, *Turbulent transport in rotating tokamak plasmas*, PhD thesis, University of Warwick, 2011.
- [13] T. Vernay et al., *Physics of Plasmas* **17**, 122301 (2010).
- [14] A. Bottino et al., *Plasma Physics and Controlled Fusion* **53**, 124027 (2011).

- [15] S. Saarelma et al., Plasma Physics and Controlled Fusion **54**, 085012 (2012).
- [16] C. Roach, D. Applegate, and J. Connor, Plasma physics and **47**, B323 (2005).
- [17] V. D. Shafranov, Soviet Physics JETP **6**, 545 (1958).
- [18] V. S. Mukhovatov and V. D. Shafranov, Nuclear Fusion **11**, 605 (1971).
- [19] P. C. Liewer, Nuclear Fusion **25**, 543 (1985).
- [20] L. Hinton and R. D. Hazeltine, Reviews of Modern Physics **48**, 239 (1976).
- [21] C. Angioni et al., Plasma Physics and Controlled Fusion **51**, 124017 (2009).
- [22] H. Meyer et al., Nuclear Fusion **49**, 104017 (2009).
- [23] B. Lloyd et al., Nuclear Fusion **51**, 094013 (2011).
- [24] A. J. Wootton et al., Physics of Fluids B: Plasma Physics **2**, 2879 (1990).
- [25] W. Horton, Reviews of Modern Physics **71**, 735 (1999).
- [26] F. I. Parra and P. J. Catto, Physics of Plasmas **17**, 056106 (2010).
- [27] G. R. Tynan, A. Fujisawa, and G. McKee, Plasma Physics and Controlled Fusion **51**, 113001 (2009).
- [28] H. W. Hendel, Physics of Fluids **11**, 2426 (1968).
- [29] C. M. Surko and R. E. Slusher, Physical Review Letters **37**, 1747 (1976).
- [30] E. Mazzucato, Physical Review Letters **36**, 792 (1976).
- [31] L. D. Landau, Journal of Physics (USSR) **10**, 25 (1946).
- [32] S. C. Cowley, R. M. Kulsrud, and R. Sudan, Physics of Fluids B: Plasma Physics **3**, 2767 (1991).
- [33] M. A. Beer, *Gyrofluid Models of Turbulent Transport in Tokamaks*, PhD thesis, 1994.
- [34] P. Terry, Reviews of Modern Physics **72**, 109 (2000).
- [35] D. J. Applegate, *Gyrokinetic Studies of a Spherical Tokamak H-mode Plasma*, PhD thesis.
- [36] P. H. Diamond, S.-I. Itoh, K. Itoh, and T. S. Hahm, Plasma Physics and Controlled Fusion **47**, R35 (2005).

- [37] T. Klinger, A. Latten, A. Piel, G. Bonhomme, and T. Pierre, Plasma Physics and Controlled Fusion **39**, B145 (1997).
- [38] M. Rosenbluth and F. Hinton, Physical Review Letters **80**, 724 (1998).
- [39] G. McKee et al., Review of Scientific Instruments **70**, 913 (1999).
- [40] S. L. Newton, S. C. Cowley, and N. F. Loureiro, Plasma Physics and Controlled Fusion **52**, 125001 (2010).
- [41] B. McMillan, T. Vernay, A. Bottino, S. Jolliet, and L. Villard, Effects of toroidal and poloidal shear flow in global gyrokinetic simulations, in *EPS2010*, pages 1–4, 2010.
- [42] M. Reshko, *Gyrokinetic Simulations of the Effects of Equilibrium ExB Flow Shear on Microinstabilities and Transport in Tokamaks*, PhD thesis, 2009.
- [43] J. W. Connor and T. J. Martin, Plasma Physics and Controlled Fusion **49**, 1497 (2007).
- [44] V. Antoni et al., Plasma Physics and Controlled Fusion **47**, B13 (2005).
- [45] J. E. Kinsey, R. E. Waltz, and J. Candy, Physics of Plasmas **12**, 062302 (2005).
- [46] Y. Kishimoto et al., Plasma Physics and Controlled Fusion **41**, A663 (1999).
- [47] T. S. Hahm et al., Physics of Plasmas **6**, 922 (1999).
- [48] R. E. Waltz, R. L. Dewar, and X. Garbet, Physics of Plasmas **5**, 1784 (1998).
- [49] K. H. Burrell, Physics of Plasmas **4**, 1499 (1997).
- [50] J. Kim, Y. Kishimoto, M. Wakatani, and T. Tajima, Physics of Plasmas **3**, 3689 (1996).
- [51] T. S. Hahm and K. H. Burrell, Physics of Plasmas **2**, 1648 (1995).
- [52] B. a. Carreras, K. Sidikman, P. H. Diamond, P. W. Terry, and L. Garcia, Physics of Fluids B: Plasma Physics **4**, 3115 (1992).
- [53] J. Connor et al., Nuclear Fusion **44**, R1 (2004).
- [54] F. Wagner et al., Physical Review Letters **49**, 1408 (1982).
- [55] S. Jolliet et al., Computer Physics Communications **177**, 409 (2007).

- [56] A. Bottino et al., *Physics of Plasmas* **14**, 010701 (2007).
- [57] L. Villard et al., *Nuclear Fusion* **44**, 172 (2004).
- [58] W. Lee, *Physics of Fluids* **26**, 556 (1983).
- [59] H. Lutfens, A. Bondeson, and O. Sauter, *Computer physics communications* **97**, 219 (1996).
- [60] R. Hatzky, T. M. Tran, A. Konies, R. Kleiber, and S. J. Allfrey, *Physics of Plasmas* **9**, 898 (2002).
- [61] T. Vernay et al., *Physics of Plasmas* **19**, 042301 (2012).
- [62] A. M. Dimits et al., *Physics of Plasmas* **7**, 969 (2000).
- [63] S. Saarelma et al., *EPS2010* , 3 (2010).
- [64] J. E. Rice, *Journal of Physics: Conference Series* **123**, 012003 (2008).
- [65] L.-G. Eriksson, E. Righi, and K.-D. Zastrow, *Plasma Physics and Controlled Fusion* **39**, 27 (1997).
- [66] C. M. Roach et al., *Plasma Physics and Controlled Fusion* **51**, 124020 (2009).
- [67] R. R. Dominguez and G. M. Staebler, *Physics of Fluids B: Plasma Physics* **5**, 3876 (1993).
- [68] A. Brizard and T. Hahm, *Reviews of Modern Physics* **79**, 421 (2007).
- [69] PPPL, TRANSP references.
- [70] B. F. McMillan et al., *Physics of Plasmas* **18**, 112503 (2011).
- [71] P. Angelino et al., *Physics of Plasmas* **13**, 052304 (2006).
- [72] F. J. Casson et al., *Physics of Plasmas* **17**, 102305 (2010).
- [73] L. Villard et al., *Plasma Physics and Controlled Fusion* **52**, 124038 (2010).
- [74] J. Taylor and H. Wilson, *Plasma Physics and Controlled Fusion* **38**, 1999 (1996).
- [75] H. Biglari, P. Diamond, and P. Terry, *Physics of Fluids B: Plasma Physics* **2**, 1 (1990).

- [76] D. Dickinson, C. M. Roach, and H. R. Wilson, Probing the linear structure of toroidal drift modes, in *EPS2011*, 2011.
- [77] A. Field et al., Nuclear Fusion **51**, 063006 (2011).
- [78] S. Sorge and R. Hatzky, Plasma physics and controlled fusion **44**, 2471 (2002).
- [79] S. Jolliet, *Gyrokinetic PIC simulations of ITG and CTEM turbulence in tokamaks*, PhD thesis, EPFL, 2009.
- [80] R. J. Akers et al., Plasma Physics and Controlled Fusion **45**, A175 (2003).
- [81] M. Romanelli et al., Full orbit simulations of ion collisional and turbulent transport in the MAST spherical tokamak, 2010.
- [82] B. D. Dudson et al., Plasma Physics and Controlled Fusion **50**, 124012 (2008).
- [83] A. Kirk et al., Plasma Physics and Controlled Fusion **48**, B433 (2006).
- [84] R. J. Akers et al., Transport studies in the MAST spherical tokamak, in *Proceedings of the 22nd IAEA Fusion Energy Conference*, number 1, pages EX/2-2, Geneva, Switzerland, 2008.
- [85] M. Romanelli et al., Plasma Physics and Controlled Fusion **53**, 054017 (2011).
- [86] B. F. McMillan et al., Physics of Plasmas **15**, 052308 (2008).
- [87] T. Gorler et al., Physics of Plasmas **18**, 056103 (2011).
- [88] B. F. McMillan et al., Physics of Plasmas **16**, 022310 (2009).
- [89] P. Diamond et al., Nuclear Fusion **41**, 1067 (2001).
- [90] B. D. Scott, New Journal of Physics **4**, 52 (2002).
- [91] M. Barnes, F. Parra, and a. Schekochihin, Physical Review Letters **107**, 1 (2011).
- [92] a. a. Schekochihin et al., Plasma Physics and Controlled Fusion **50**, 124024 (2008).
- [93] I. G. Abel, M. Barnes, S. C. Cowley, W. Dorland, and a. a. Schekochihin, Physics of Plasmas **15**, 122509 (2008).
- [94] X. Garbet, Y. Idomura, L. Villard, and T. H. Watanabe, Nuclear Fusion **50**, 043002 (2010).

- [95] D. Mikkelsen and W. Dorland, Physical Review Letters **101**, 1 (2008).
- [96] O. Ford, J. Svensson, a. Boboc, and D. C. McDonald, Review of Scientific Instruments **79**, 10F324 (2008).
- [97] Y.-C. Ghim, A. R. Field, S. Zoletnik, and D. Dunai, The Review of scientific instruments **81**, 10D713 (2010).
- [98] A. R. Field et al., The Review of scientific instruments **83**, 013508 (2012).
- [99] A. R. Field, Personal Communication, 2012.
- [100] J. S. Bendat and A. G. Piersol, *Random Data*, Wiley, 2010.
- [101] P. F. Dunn, *Measurement and Data Analysis for Engineering and Science*, McGraw-Hill Higher Education, 2005.
- [102] J. Candy and R. Waltz, Physical Review Letters **91**, 4 (2003).
- [103] L. D. Landau, Phys. Z. Sowjetunion **10**, 154 (1936).
- [104] A. Bottino, *Modelling of global electrostatic microinstabilities in tokamaks: effects of $E \times B$ flows and magnetic shear*, PhD thesis, 2004.